A RADAR-BASED CLIMATOLOGY OF THUNDERSTORMS IN HAWAIʻI

A THESIS SUBMITTED TO THE GRADUATE DIVISON OF THE UNIVERSITY OF HAWAIʻI AT MĀNOA IN PARTIAL FULFILLMENT OF THE REQUIREMENTS FOR A DEGREE OF

MASTER OF SCIENCE

IN

ATMOSPHERIC SCIENCE

MAY 2018

By

Robert A. Ballard

Thesis Committee:

Gary M. Barnes, Chairperson
Michael Bell
Yi-Leng Chen

ACKNOWLEDGEMENTS

First, I want to thank my lovely wife Maureen for her patience, understanding, flexibility, and encouragement throughout my time in graduate school. My success would not be possible without her support and love! Nor would it have happened if it weren't for the prodding nudges, gentle encouragement, and loving reminders from my mom!

Huge thanks to Kevin Kodama and Nicole Evans for their GIS assistance, and to my beta-readers Tina Stall and Justin Gibbs for putting fresh eyes on my grammar, references, and content suggestions. I want to also thank Julie Kelly, who long ago twisted my arm (i.e., physically threatened me) to get me to finally apply for Graduate School in the first place. I also want to thank Andy Nash and Wes Browning for long ago providing the spark of the research topic that piqued my interest. Special thanks go to my math tutors Tom "Danger" Robinson and Aaron Levine for helping me see through the smokescreen that surrounds the more dynamic and physical aspects of meteorology. Big mahalos to all my friends who have offered so much love and moral support (and yes, a little good-natured "old guy" razzing) over the years, including (but not limited to): Cindy, Duncan, Leigh Anne (no hyphen), Bonnie, Vanessa, Shannon, Tommy, Andre, Carl, Morgan, Andrew, Dr. Andy DeWald, Alejandro, Alyssa, Tom, Ian, Matt, Sandy, Klaus, and Chappy. I've had a BLAST celebrating our successes along the way together!

This effort would not have been possible without the gift of time and frequent encouragement from my bosses Jim Weyman, Ray Tanabe, Tom Evans, and Chris Brenchley at the National Weather Service. I also want to thank the Professors (past and present) at the University of Hawai'i Atmospheric Sciences Department, for being patient with a guy who lapsed 15 years between his undergraduate and graduate studies, and for making my graduate experience in meteorology fun, rewarding, and challenging.

ABSTRACT

While relatively infrequent, hazards related to severe convection in Hawai‘i do occasionally occur. Our understanding of these events can be improved by using algorithm data from the Weather Surveillance Radar-1988 Doppler (WSR-88D) to help build a spatial, temporal, and intensity climatology which eliminates population density and diurnal sampling biases. Radar can also expand the climatological area by approximately 17 times over that offered by land-based reports only. Surface and upper air observations and storm reports are used to validate the radar algorithm output. Parameters and indices from sounding data at Līhu‘e are compared to observed thunderstorms, as well as to output from the Maximum Estimated Hail Size (MEHS) and Tornado Vortex Signature (TVS) algorithms, to establish values significant for the occurrence of these events. The data show that greater instability is typically needed to support thunderstorms in Hawai‘i, approximately double that found for similar events over the continental United States. MEHS values greater than 32 mm appear to indicate a higher risk of severe hail in Hawai‘i, and these occur within radar range on average every 5.5 days per year. MEHS values likely to be associated with supercells and very large hail occur within radar range about 1.5 day per year. Most TVSs in Hawai‘i are associated with delta-V values of <30 m s^{-1}, but values ≥ 45 m s^{-1} (known to be associated with strong tornadoes) have been observed. The results presented here should help forecasters to better evaluate the risk of these rare but important events.

TABLE OF CONTENTS

LIST OF TABLES

LIST OF FIGURES

Chapter 1. Introduction & Motivation

Thunderstorms are infrequent in Hawai‘i, but when they occur, they often cause significant local hazards and impacts. While the most significant threat from thunderstorms in Hawai‘i is well-known to be flash flooding (Kodama and Barnes 1997**,** Kodama and Businger 1998), other hazards do present themselves on occasion. Lightning is an obvious hazard to mariners. Thunderstorms also pose hazards to the residents and visitors enjoying a wide variety of outdoor activities, many of whom may not be accustomed to the need to take protective action from the weather. Thunderstorms can also cause problems for Hawai‘i’s isolated electrical infrastructure. The Honolulu Advertiser reported that on December 26, 2009, a series of lightning strikes on the O‘ahu power grid caused an island-wide outage that lasted over 12 hours.

Other thunderstorm hazards, though even less frequent, are not unheard of. This includes damaging winds, large hail, tornadoes, and tornadic waterspouts (collectively referred to here as “severe weather”). Two tornadoes, rated EF-0 and EF-1, occurred on February 11, 2009 near the Kapolei Golf Course, according to a Public Information Statement issued by the National Weather Service (NWS). One of the tornadoes caused minor injuries to one person (NCEI 2009a). These tornadoes were spawned from a short-lived thunderstorm that appeared to form on a sea breeze convergence boundary. On the 8th and 9th of January 2005, a severe squall line swept across parts of the state, causing a tornado as well as straight line winds up to 33 m s^{-1} on Kaua‘i and 32 m s^{-1} on O‘ahu. These winds uprooted trees, damaged roofs, fences and carports, and caused power outages (NCEI 2005, NOAA 2005). In the predawn hours of March 5, 2011, a “bow echo” associated with a squall line knocked down at least 30 trees and a number of utility poles in the Ewa region of O‘ahu (NCEI 2011). On December 9, 2010, a severe squall line moved across Kaua‘i, causing wind damage (NCEI 2010). A severe thunderstorm hit the Kahului

airport on December 20, 2009, producing wind gusts to 26 m s^{-1} as well as hail up to 19 mm in diameter (NCEI 2009b). Finally, large, damaging hail can also occur. An upper trough in March 2012 caused a thunderstorm that brought hail up to 38 mm in diameter on O‘ahu from Waimānalo to ‘Āina Haina (NCEI 2012) on the 6th. A few days later, a supercell thunderstorm associated with an outbreak of severe weather on March 9, 2012 brought giant hail to Kailua and Kāne‘ohe, with hailstones of nearly 11 cm across on their long axis (NCEI 2012). Hail this large was previously unheard of in the Hawaiian Islands. This is just a sample of relatively recent severe weather events in Hawai‘i.

We do not know much about these unusual events. Most local studies have focused on the heavy rain and flash flooding threat. Prior to the mid-1990s, the primary datasets used to observe hazardous weather in Hawai‘i were a dense network of telemetered gauges which reported intense rainfall in near-real time, as well as geostationary and polar satellite imagery. These datasets were useful in identifying flash flood threats, but were not able to provide much information about the causes of severe weather events. Schroeder (1977) recognized the need for weather radar in Hawai‘i to assist in the detection of severe weather, but it would be more than 15 years before that observation network became a reality, decades after many other parts of the United States had network radar coverage.

The NWS in Honolulu is responsible for forecasting and warning for severe weather events. One component to improved forecasting for a given type of event is knowledge of the event climatology, followed closely by an understanding of the synoptic and mesoscale conditions in which they occur (Johns and Doswell 1992). Barnes (2001) summarized the general necessary conditions for severe weather events in the tropics, and his work will serve as a general guide for a more detailed examination. However, as he points out, obtaining a more

detailed climatology in isolated areas like Hawai‘i can be challenging. There are limitations with using public and spotter reports alone, as these likely do not tell the full story of the extent, frequency, or intensity of such events. A challenging combination of small sample sets, a vast surrounding ocean with very few *in situ* reports, limited remote sensing data, and areas of sparsely populated land add to the complexity of creating a climatology. Even at the few observing sites where automated observations are augmented by human observers to include significant phenomena (thunderstorm, waterspout, funnel cloud, tornado, hail, etc.), reporting by airport personnel may take a lower priority to other duties.

This study is designed to produce a more complete climatology of severe weather events by utilizing radar data as proxy for some types of these events. Radar will help remove diurnal and population biases, and can be applied over a much larger area than public reports. I first propose a simple algorithm-based radar proxy for storm electrification, then use the proxy to assess the climatology as well as some of the local thermodynamic and kinematic conditions that tend to be favorable for thunderstorms in Hawai‘i. I then use the radar algorithms to assess the climatology of stronger events, including some signatures that likely indicate severe thunderstorms. For this study, I utilize the current NWS definition when referring to severe thunderstorms: Any thunderstorm producing hail over 25 mm in diameter (also referred to here as “large hail” or “severe hail”), straight line winds of 26 m s^{-1} or greater (i.e., “damaging straight line winds” or “severe straight line winds”), or a tornado. While this study will not be an exhaustive treatment of all aspects of thunderstorms and severe weather in Hawai‘i, the information presented here should prove helpful in an initial assessment, with future studies covering other aspects of the forecast problem. I begin by examining some previous research in regards to severe thunderstorms in Hawai‘i.

1.1 Tornadoes, funnel clouds, and waterspouts.

Price and Sasaki (1963) noted that thunderstorms in Hawai‘i were “accompanied at times by small hail, but seldom by high winds.” However, there had also been a few cases of tornadoes, waterspouts, and funnel clouds (hereafter collectively referred to as “funnel events”). In order to gain a better understanding of the frequency of funnel events, Price and Sasaki (1963) used Weather Bureau logs and newspaper accounts to catalog reports. They examined the monthly and diurnal distribution of reports from August 1948 to December 1960, as well as the accompanying weather conditions, radiosonde observations, and general synoptic situation. Logging and archiving of reports, particularly during the early part of that era, was not stressed as much as it is today. They noted that an effort toward improved reporting during the period of their study resulted in a gradual increase in reports with time. Although their sample size was rather small, with only 31 total days, they were able to identify some interesting background characteristics related to the synoptic situation ongoing at the time of the reports. Many of the reports occurred on days when the trade winds were interrupted and sea breezes were blowing, and were preceded by abundant sunshine. A smaller number of funnel events appeared to have close connections to a synoptic scale system such as a front, a kona low, or upper level trough or low. It was difficult to ascertain seasonal variability from the limited reports. There were no nighttime funnel events in their dataset, which they surmised was from the difficulty in spotting these features in darkness. Again, this was still well before the era of weather radar in Hawai‘i; at that time, visual reports were the only way to ascertain the existence of these features.

Schroeder (1977) added 15 more years to the dataset started by Price and Sasaki, extending the period to December 1975. There was a large increase in the number of funnel event reports during this period, but he noted that many of these tended to cluster in areas of

relatively high population density or from those with a unique interest in such features (e.g., meteorologists, aviators, and mariners). He found that funnel events were more common during the months of October through April. This seems to agree with the previous findings of funnel events favoring light wind days, which occur most often during the cool season in Hawai‘i. Although most funnel events occurred during relatively benign synoptic regimes, Schroeder did note some significant exceptions and concluded that in rare instances, conditions more typical of mid-latitude tornado situations can occur in Hawai‘i. For example, Schroeder (1977) discussed a case of a tornado in Kailua-Kona on Hawai‘i Island in 1971 which caused $1.5 million in damage.

Tanabe (2000) extended the climatology of funnel events to the period from 1976 to 1997. His findings echo those of the previous studies, that population and diurnal observational biases are likely causing underreporting in the climatology. This is particularly true for funnel clouds and waterspouts, but less so for tornadoes as the resultant damage from a storm may be noticed afterward, even if no one was able to see the storm at that time. Tanabe also showed that many classic sounding indices appeared to be insufficient to capture most funnel events in Hawai‘i, with little significant difference between climatological values and funnel event values. Tanabe’s study again showed the vast majority of funnel events occurred during benign synoptic conditions, but some events appeared to be associated with significant synoptic features like cold fronts and kona lows.

In keeping with the hypothesis that many severe weather events go unreported, this study will attempt to examine and catalog severe weather using significant radar-based signatures, including high reflectivity aloft and strong rotation. This should eliminate population and diurnal biases. For example, Kodama and Businger (1998) documented a strong velocity couplet

associated with a mesocyclone on radar 40 km northeast of O‘ahu in January 1996 that was never reported by the public. It would be useful for us to know how often such events occur, regardless of whether or not a report was received. Weaker events, such as tornadoes and waterspouts not spawned by mesocyclones, will generally not be included here. This is not meant to imply that these events are not significant or worth additional study. On the contrary, non-supercell tornado events, like the previously mentioned Kapolei tornadoes in 2009 can cause significant damage or injuries. However, because of the shallow nature of the vortex (compared to the rotational depth of a mesocyclone associated with a supercell), they continue to be elusive and are unlikely to be captured by the radar data used in this study. In many cases, known funnel events accompanied by reliable public reports (which now often include photographs and video) could not be discerned in the radar base data. The radar’s tornado detection algorithm is simply much more likely to detect stronger, larger, deeper, and more persistent circulations that originate from mesocyclones (Mitchell et al. 1998). These considerations will be discussed in further detail later.

1.2 Hail

There are few studies that mention hail in Hawai‘i. However, Price and Sasaki (1963) noted it does occur on rare occasions, and is almost always small. Frisby and Sansom (1967) compiled a global summary of hail in the tropics and mentioned two cases of hail falling in Hawai‘i, one in Hilo (that produced hail of 6 mm in diameter) and one on O‘ahu, in 1964 and 1965, respectively. Hail falls somewhere in Hawai‘i about 5 to 10 times per year (Blumenstock and Price 1967), and most often at higher elevations on the Big Island (Barnes 2001). There are a few cases, however, when hail of larger sizes has occurred, even at lower elevations. Takahashi

(1987) documented a case of a storm which dropped widespread, uniquely shaped hail over the eastern side of the Big Island, with an average diameter of 18 mm. Although the focus of his research was on the embryos, growth, and shape of the frozen hydrometeors, he offered several examples of large hail, including one spike-shaped stone that was approximately 60 mm long. The thunderstorms responsible for the large hail were caused by a strong cold front, demonstrating once again that at least occasionally, favorable synoptic environments can lead to severe weather in Hawai‘i. Lyman et al. (2005) did a study of a flash flood-producing severe thunderstorm at Hana, on the island of Maui. Although their focus was on the radar signatures of extreme rainfall that had occurred with this storm, they mention that the storm had some supercell characteristics, and also dropped hail up to 25.4 mm in diameter.

Since large hail in the tropics is quite rare, radar indications of large hail imply intense updrafts, a favorable synoptic environment with the possibility of other severe modes, as well as supercells (Barnes 2001). This study presents a climatology of algorithm indicated hail signatures as well as a climatology of relevant sounding-based indices for such events.

1.3 Damaging straight line winds

Blumenstock and Price (1967) state that “once every 3 or 4 years on the average a cold front storm will produce winds that blow down trees or rip the roofs from houses within a limited area of a square mile or so.” It was not clear from this description if the damage from these events is attributable to frontal (or pre-frontal) convection, or damaging gradient winds blowing downslope and through terrain gaps. In some cases, these two events can be nearly co-located in time and space, with shallow convection possibly functioning as an additional component to

terrain-accelerated gusts. Other cases are more clearly convectively forced. For example, Businger et al. (1998) documented a case of damaging straight line winds associated with a bow echo along a squall line in Hawai‘i that was observed in November 1995. This was soon after the installation of the Weather Surveillance Radar-1988 Doppler (hereafter, WSR-88D) on Kaua‘i. The squall line, caused by a kona low, knocked down trees and power lines, and tore the roof off the Nāwiliwili Small Boat Harbor where winds of 40 m s^{-1} were reported. Based on the radar indications of severe winds in the reflectivity and velocity imagery, the NWS in Honolulu issued the first-ever Severe Thunderstorm Warning in the state of Hawai‘i, which verified with lead time.

While a number of known squall line damaging wind cases have occurred, using radar data alone to develop a climatology of all possible severe straight-line wind events is challenging, with complex sampling issues to consider. Some cases of damaging winds appear to be easily detectable in radial velocity imagery. However, since the radars only detect radial motion, velocities of severe magnitude can be completely undetectable if the wind is blowing normal to the beam. To complicate matters further, the lowest radar elevation angle becomes increasingly separated from the surface with distance from the radar, making it difficult to ascertain the surface wind speed with any confidence. A network of many well-sited radars would be necessary to adequately estimate the full horizontal near-surface wind field. There is no archived operational radar algorithm output specifically designed to assist in identifying cases of damaging winds associated with squall lines and bow echoes (sometimes collectively referred to as quasi-linear convective systems or “QLCS”). Forecasters are trained to look for several different signatures in radar base data to identify situations when damaging wind is likely occur within a thunderstorm. Unfortunately, executing some of these techniques (e.g., examining

storms for very high reflectivity aloft, mid-altitude radial convergence, storm-top divergence, etc.) requires the examination of data which is not available in the radar archive.

The area affected by a severe squall line or bow echo is typically larger than that of a weak tornado. Like tornadoes, the damage they leave may be reported later, even in more sparsely populated areas. Some radar-indicated large hail cases also yield damaging wind signatures, though many (if not most) damaging wind signatures likely occur in the absence of radar-indicated hail.

1.4 Goals

The main goal of this study is to offer a more complete climatology of thunderstorms and their intensity than can be accomplished using documented public reports alone. In order to do this, my study investigates the following:

1. Examine commonly utilized sounding parameters and indices associated with reported thunderstorms, in order to determine significant thresholds or ranges of each that generally support thunderstorms in Hawai‘i.

2. Establish a radar algorithm-based proxy for thunderstorm, and then examine the same sounding based parameters for those cases.

3. Examine the climatology of stronger radar-algorithm-based events, especially those that are likely to produce severe weather.

4. Examine sounding parameters and indices associated with radar algorithm based events expected to be associated with severe weather, to determine which are useful and what values are significant.

The introduction of an radar-based event climatology, as well as the discovery of significant sounding-based parameters associated with radar detected convective events, should lead to an improved understanding of these unusual but important occurrences, resulting in better forecasts and warnings for them in the future.

Chapter 2. Data & Methodology

Three primary datasets were used for this study. These included surface and upper air observations from the NWS office in Līhu‘e, and data from the WSR-88D network in Hawai‘i. The upper air data was obtained via the University of Wyoming online sounding archive (http://weather.uwyo.edu/upperair/sounding.html), and was displayed using the RAOB software package (http://www.raob.com). Surface observations were obtained from the National Centers for Environmental Information (NCEI, previously National Climatic Data Center) Local Climatological Data (LCD) as well as from the NCEI Integrated Surface Database. Level III radar data were obtained from the NCEI radar archive, and output from the Maximum Estimated Hail Size (MEHS) and Tornadic Vortex Signature (TVS) radar post-processing algorithms was obtained from the NCEI Severe Weather Data Inventory (SWDI). While native-resolution Level II data would have been preferable to examine the base data, hardware failures with the archive system led to prolonged outages in the dataset until the NWS initiated electronic collection of the data in January 2010. It should be noted that the SWDI dataset is described as “experimental.” During the course of this research, it was discovered that there were instances where some data were missing for known case days. The author worked with the data curator at NCEI to reprocess several days that were known to have missing data. The radar data were interrogated using the GRLevel3 software (http://www.grlevelx.com). A discussion of some of these datasets follows.

2.1 Radiosonde observations associated with surface observations of thunder

There are two upper air sites in the Hawaiian Islands: Līhu‘e, on the island of Kaua‘i, and Hilo, on the windward side of the Big Island. Līhu‘e was chosen to be the primary focus for this

study in order to assess the local thermodynamic and kinematic background conditions that would be contributing to large scale convective potential, organization, and intensity. The diurnally forced circulations caused by diabatic heating and cooling of the relatively large land mass of the Big Island (e.g., Leopold 1949, Chen and Nash 1994, Chen and Feng 1995) significantly influence the sounding conditions at Hilo (Lavoie 1967, Garrett 1980, Kodama and Barnes 1997). This would limit the representativeness of the stability data, which is a key part of the study. Kauaʻi is a much smaller island with less elevation change, and although the Līhuʻe site suffers from some of these localized boundary-layer effects, they appear to occur less often and to a lesser degree than at the Hilo site.

In order to identify sounding parameter space favorable for thunderstorms in Hawaiʻi, a comparison was done with upper air data for the years 1973-2015. First, when the LCDs and surface observations indicated the start of a thunderstorm at the Līhuʻe site, selected parameters were obtained from the most recent 0000 UTC or 1200 UTC upper air sounding within 12 hours prior to the occurrence. Soundings which exhibited extremely unusual tendencies (e.g., the entire sounding exhibited an inversion, extreme and unrealistic wind speeds, or non-meteorological superadiabatic layers that would adversely affect data quality), or that had ongoing convection near the time of the sounding, were not used. Using a pre-thunderstorm "antecedent" sounding (rather than the sounding taken closest to the time of the event) helped to mitigate some data quality effects. These could be caused either by the thunderstorms themselves (e.g., cool outflow winds from local convection modifying the boundary layer) or by the passage of strong synoptic scale boundaries triggering thunderstorms (e.g., the site being in a post-frontal air mass at sounding time). Although the thermal and moisture gradients found in subtropical marine environments are typically substantially less than those found in mid-latitude continental

environments (Barnes 2001), even relatively minor variations (particularly with boundary layer temperature or moisture content) can result in a poor evaluation of convective potential.

One could use objective analyses from numerical models or from satellite remote sensing data to obtain these parameters rather than observed sounding data. However, the limited amount of *in situ* data available for model analyses in an area very distant from any rawinsonde networks, as well as the limitations and assumptions made from satellite sounder data used in the models (e.g., Dostalek and Schmit 2001), make observed data preferable to initiate such a climatology.

For each occurrence of a thunderstorm at Līhuʻe, several parameters and indices were obtained from the antecedent sounding (Table 1). These parameters were chosen in part for their relationship to two of the three necessary ingredients for convection: sufficient low-or-mid tropospheric moisture and conditional instability over a deep layer (Johns and Doswell 1992, Doswell 1987). Although the focus for this portion of the study is any thunderstorm, for completeness and later comparison, parameters typically used to evaluate severe weather threats were included here as well. The choice of parameters also reflected their familiarity by forecasters, and in some cases, their inclusion in previous Hawaiʻi studies. This is certainly not meant to be an exhaustive list of all parameters that may be useful to examine from the sounding, but to serve as a starting point to establish a baseline climatology of some more well-known parameters. It should be noted that the use of parameters in a forecast sense, even when compared to climatological reference values, should not replace attempts to gain a deeper physical understanding of the meteorological processes in a given situation, including the probable synoptic or mesoscale lifting mechanisms (Doswell et al. 2006).

Table 1. Convective-related parameters utilized throughout this study. (The definitions of these parameters is given in Appendix B).

Ordinary deep convection parameters	Severe weather parameters
Precipitable water	0-6 km bulk shear magnitude
Surface based CAPE (SBCAPE)	Supercell composite parameter
Mixed layer CAPE (MLCAPE)	0-1 km Storm relative helicity
Most unstable CAPE (MUCAPE)	0-3 km Storm relative helicity (SRH)
Lifted Index	SWEAT index
K-Index	
500 hPa geopotential height	
500 hPa temperature	
700 hPa geopotential height	
700 hPa temperature	
500-700 hPa lapse rate	

2.2 Upper air and WSR-88D hail algorithm data.

2.2.1 The radar network in the state of Hawai'i

In the second part of this study, I matched upper air soundings to algorithm data from the WSR-88D network in Hawai'i archived in the SWDI. The WSR-88D network in Hawai'i consists of four 10 cm wavelength (S-band) radars. These are located on the southern part of the island of Kaua'i (PHKI), on west Moloka'i (PHMO), on the northern part of the Big Island in the Kohala Mountains (PHKM), and on the southern part of the Big Island near Na'alehu (PHWA). The locations and elevations of the WSR-88Ds are given in Table 2. The radars have a horizontal beam width of 1 degree, with a range gate of 1 km for reflectivity, and 250 m for velocity. The full radar range of the WSR-88D is 459 km (248 nautical miles). However, the radar-based algorithms are only calculated to a range of 230 km (124 nautical miles). The WSR-88D has a variety of scan strategies (also known as volume coverage patterns or VCPs), which include a series of elevation angles that repeat approximately every 4 to 6 minutes when in

precipitation mode. Between 9 and 15 elevation scans are made, ranging from 0.5° above horizontal to 19.5°.

Table 2. Locations and radar elevations for the four Hawai‘i WSR-88D radars. Obtained from http://www.nws.noaa.gov/tg/pdf/wsr88d-radar-list.pdf (A plan view map of these radar locations is available in Figure 2.)

Location	Site ID	Radar elevation (m)
South Kaua‘i	PHKI	104
West Moloka‘i	PHMO	440
North Kohala	PHKM	1209
Na‘alehu	PHWA	445

2.2.2. Establishing a radar-based proxy for thunderstorm cases

This study utilizes radar to increase both the area and temporal frequency of observations to improve the climatology of thunderstorms over and near the main Hawaiian Islands. Another possible choice for a remote sensing dataset to develop a climatology of thunderstorms near the main Hawaiian Islands is data from lightning detection networks. However, to create a climatology near the islands, ideally there should be nearly continuous monitoring and consistent detection efficiency, both throughout the diurnal cycle as well as over longer periods. Over time, long range lightning detection networks that have included the central North Pacific have evolved as new sensors are added (Pessi et al. 2009, Thompson et. al 2014), during a period when the number of radars was constant. Initially the accuracy of such long range, oceanic networks appeared to be rather poor near Hawai‘i, although many improvements have been made and the data now appears to much more closely match observations and reports. Pessi et al.

(2009) described in more detail the expected evolution of the PacNET lightning detection network, for example.

In addition to changes in the sensor network with time, they also note the detection efficiency of such networks tends to drop considerably in daytime. It has been estimated that approximately 22% of the total number of lightning flashes were being detected from the PacNet long range lightning network during the day, versus approximately 61% at night. This is due to changes in the location of electron density in the ionosphere yielding improved ionospheric reflection at night. Finally, they caution that location accuracy of lightning strikes may be adversely affected in the vicinity of Hawai‘i where a limited number of sensors are available to triangulate the source.

The radar network in Hawai‘i has remained relatively unchanged since the mid-1990s. Aside from occasional maintenance issues and minor changes in scan strategies, the data should be fairly consistent during this period. Also, the radar data do not suffer from diurnal upper atmospheric changes. The long term and diurnal changes associated with lightning detection networks make it rather challenging to conduct a quantitative study of thunderstorms alone. Nevertheless, a comparison of the results from this radar-based study to more recent lightning data from a mature detection network would likely be quite useful indeed.

For the purposes of attempting to determine a thunderstorm on radar, one must consider not only the magnitude of the maximum reflectivity value, but also the levels at which high reflectivity is occurring. Several studies have noted that storm electrification typically begins when high radar reflectivity values reach environmental temperatures from 0° to -20°C (Dye et al. 1989, Toracinta et al. 1996, Yang and King, 2010). A commonly accepted threshold for the initiation of lightning is 40 dBz reaching the -10°C level. Although the WSR-88D has no

algorithm to alert the user when this occurs, there is an alternative way to approximate this threshold using the WSR-88D hail algorithm.

Hail growth requires strong updrafts to loft large amounts of supercooled water into the subfreezing levels of a cumulonimbus cloud. As previously mentioned, hail of any size is rare in Hawai‘i. Rasmussen and Heymsfield (1987) demonstrated that hailstone melting is very sensitive to the size of the frozen hydrometeor, as well as the temperature and relative humidity of the profile through which the particles are falling. In addition, Zipser and Lutz (1994) describe a number of different studies that all indicated a prevalence of relatively weak vertical velocities within tropical oceanic cumulonimbi. The deep moist environment of the oceanic tropics and subtropics, high freezing levels, and tendency toward weak updrafts are unfavorable for hail to reach the surface at such latitudes (Rasmussen and Heymsfield 1987, Barnes 2001).

As described in Witt et al. (1998), the WSR-88D uses the vertical distribution of reflectivity to estimate three parameters: the probability of the cell containing hail that will reach the surface, the probability of severe hail, and the maximum estimated hail size (MEHS). For this portion of the study, I utilize the MEHS output. The MEHS algorithm uses an integration of hail kinetic energy computed from reflectivity at environmental temperatures below 0°C to compute a severe hail index (SHI). Weighting functions are used to zero out the contributions to the SHI from reflectivity less than 40 dBz, from higher reflectivity below the melting level, and to cap the contributions from reflectivity values greater than 50 dBz at levels colder than 0°C. The computation of SHI is then used in a simple empirical relationship to calculate the MEHS to the nearest 6 mm (0.25 inch), with values returned at 6 mm increments up to 102 mm (4.0 inches). The hail size algorithm was validated with data from WSR-88Ds in Oklahoma and Florida for 147 hail reports over 9 storm days. By design, the relationship chosen to calculate

MEHS is meant to overpredict hail size, such that 75% of the reports would be expected to be smaller than returned by the algorithm.

Using the derivation presented in Witt (1998), the minimum non-zero value reported by the MEHS algorithm would occur with a reflectivity of 46 dBz extending to roughly the -10°C level. This would be very unlikely to allow hail to reach the surface at lower elevations in Hawai‘i, but based on the electrification studies, should be more than sufficient to initiate lightning within a developing cumulonimbus. Thus, MEHS ≥ 6 mm is expected to occur slightly less often than actual thunderstorm occurrences. In order to verify this hypothesis, the number of observed thunderstorm days per year Līhu‘e from 2005 to 2015 were compared against the number of days of MEHS ≥ 6 mm detected near Līhu‘e. Since the requirement to observe a thunderstorm is audible thunder (when the local noise level is sufficiently low to allow audible detection)(OFCM 2005), various ranges were chosen to establish a relationship. There is a high correlation between observed thunder and MEHS ≥ 6 mm (hereafter, “MEHS event”) for a range within 15 km of the Līhu‘e airport (Figure 1). Using this radius, however, there are actually fewer thunderstorm days than MEHS event days. A check of some individual cases indicated that thunder could be reported without a MEHS detection when:

1) A MEHS event occurred, but the cell detection was outside the allowed 15 km range. It is possible the observer could be hearing thunder at ranges greater than 15 km from the cell core in some situations, or that lightning was spreading well away from the cell core (where the MEHS detection is plotted).

2) A MEHS event did not occur from a cell known to be producing thunder, because the radar beam was significantly blocked by terrain at levels that are critical for hail calculations. This causes an underestimate of integrated reflectivity. This underestimate

can happen, for example, to the north and northwest of Līhuʻe (over much of central and eastern Kauaʻi), where there is significant beam blockage. I will discuss more about beam blockage in a moment.

When the allowable range of MEHS events is increased to 30 km around the Līhuʻe airport, the bias is nearly eliminated. The total number of thunderstorm days versus MEHS event days is similar, although the correlation decreases somewhat (Figure 2). This may be due to the difficulty of hearing thunder at distances as far as 30 km. The larger ring also encompasses even more beam-blocked area to the northwest of the observation site.

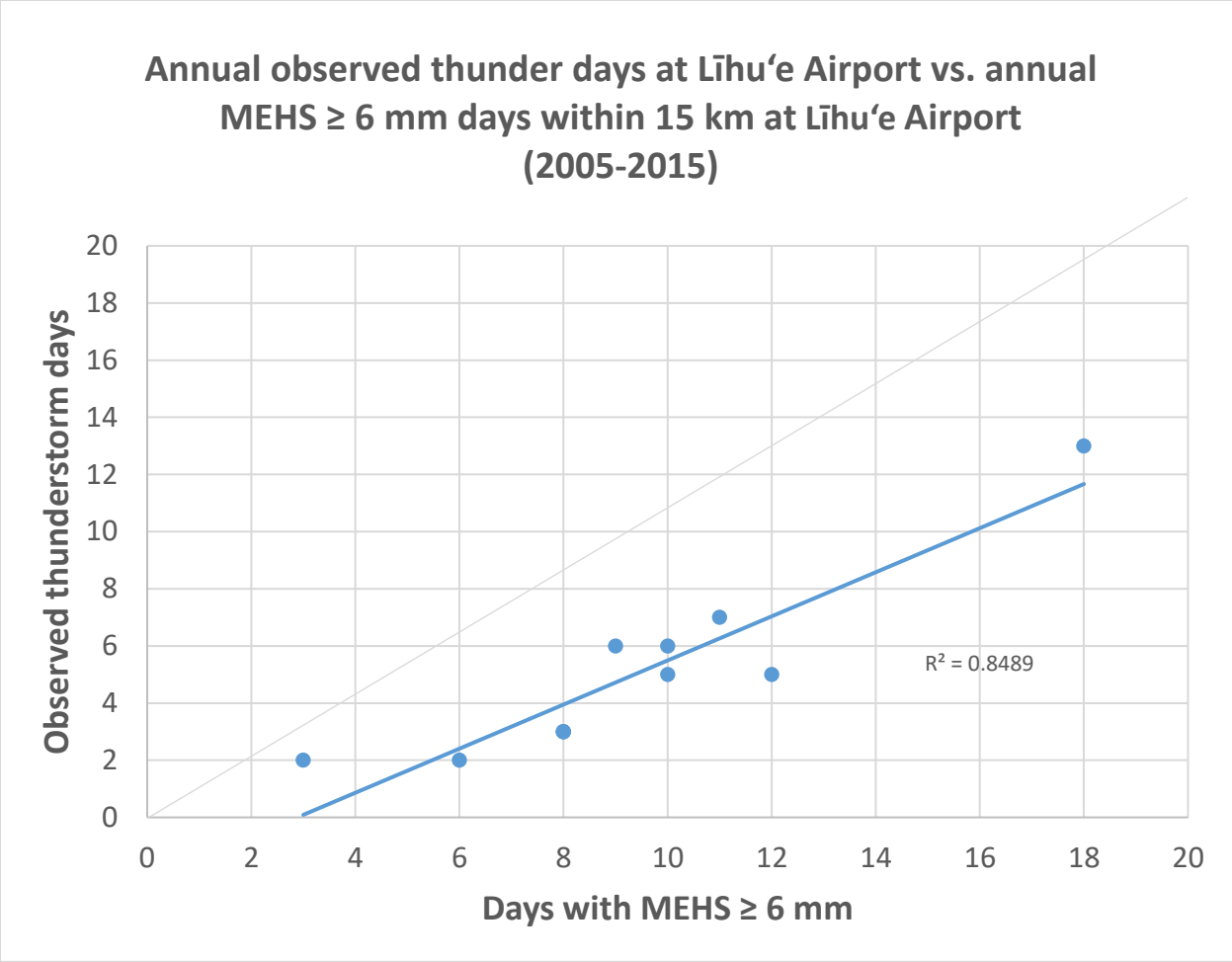

Figure 1. Observed thunderstorm days at Līhu‘e airport per year versus observed number of days with a cell returning a maximum estimated hail size (MEHS) ≥ 6 mm within 15 km of Līhu‘e airport, 2005-2015.

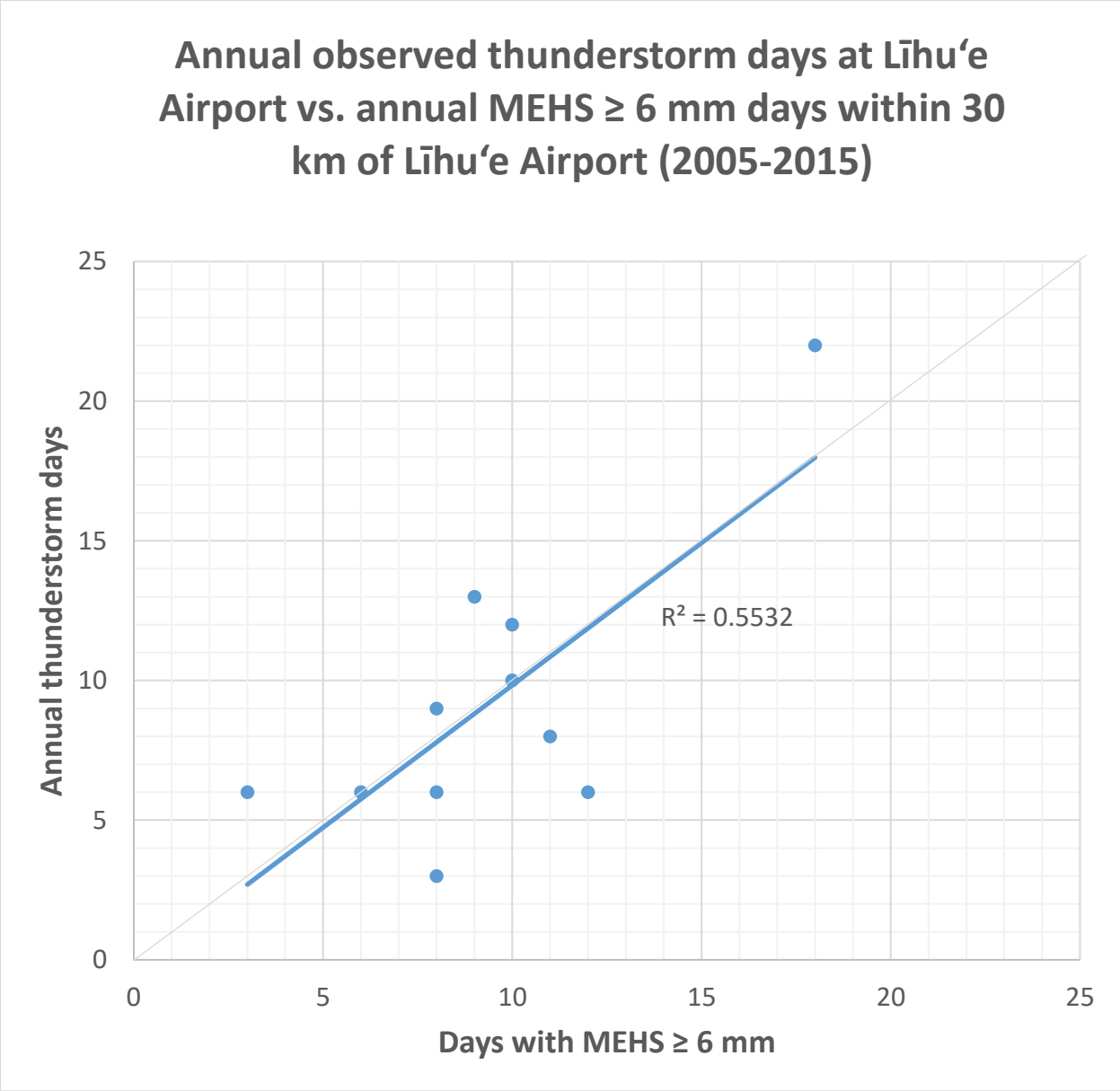

Figure 2. Same as Fig. 1, except for a 30 km MEHS radius.

2.2.3. Limitations & considerations

Beam blockage is a significant consideration for a study utilizing radar data to establish a climatology in Hawai‘i. If the radar beams were unblocked by terrain, the total area covered by the four radars would be approximately 25 times the amount of area that land-based public reports could offer. However, each of the four Hawai‘i radars has significant to near-total beam blockage along some radials due to the terrain and volcanic peaks throughout the islands. Figure 3 shows the estimated radar coverage areas using standard beam refraction for each radar, and also a mosaic of coverage from all four radars. One can see there is near total beam blockage in most of the northern semicircle of the Kaua‘i radar. A similar problem exists with the Na‘alehu radar on the Big Island. The radar there sits on a rather steep slope, with total blockage from west-southwest clockwise through east-northeast from the radome. The problem is partially mitigated somewhat by utilizing a mosaic of radar data (Figure 3), as the Moloka‘i and Kohala radars have reduced blockage. In some cases, blocked areas from a closer radar may be able to be scanned by a more distant radar. When considering beam blockage, the total area covered is still approximately 17 times the amount of land area.

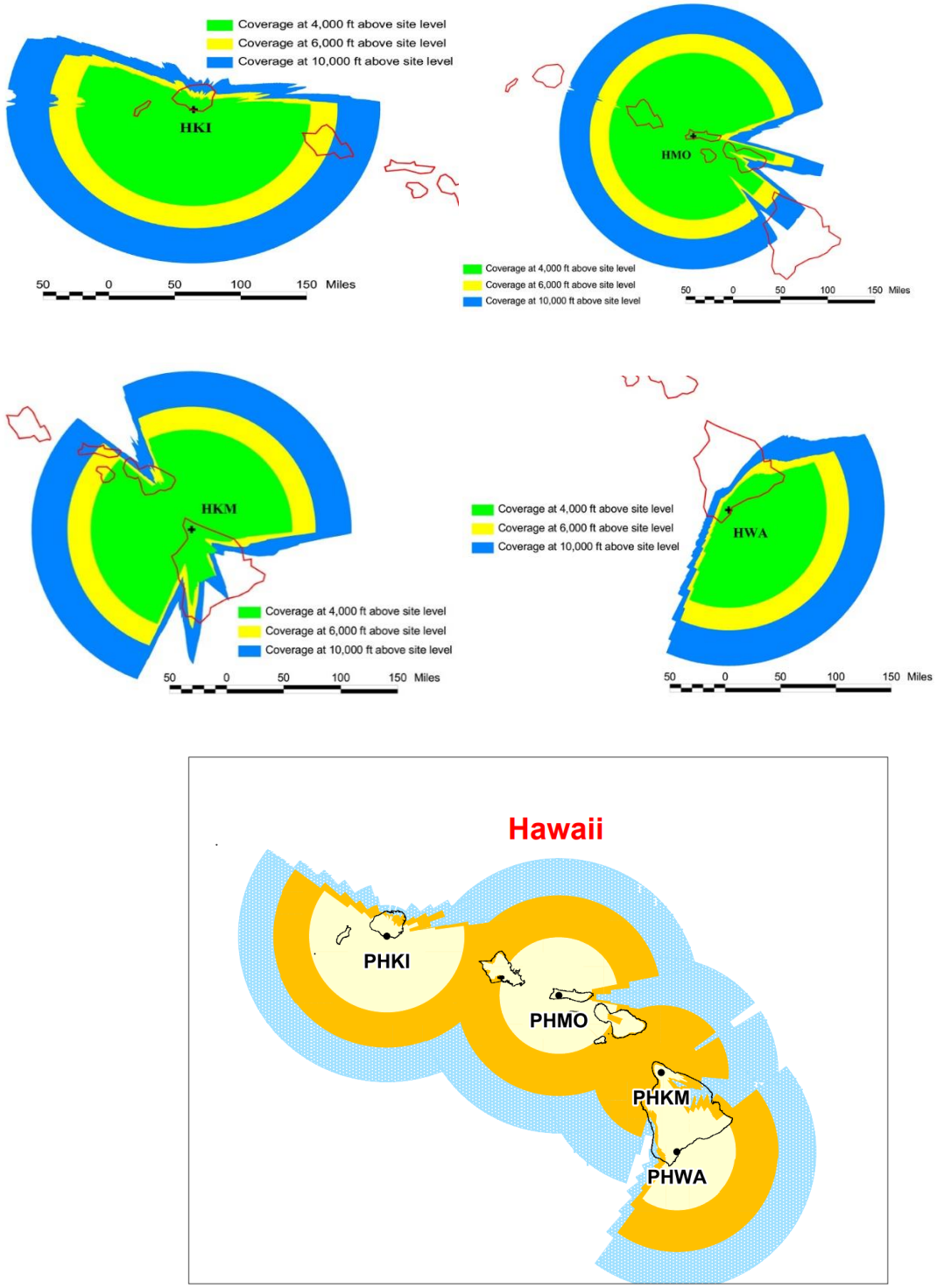

Figure 3. Areas of radar coverage with respect to beam height for the four individual radars (top), and a mosaic of coverage (bottom) provided by the NWS Radar Operations Center (https://www.roc.noaa.gov/WSR88D/). The mosaic image shows expected coverage (assuming standard refraction) at 3000 ft (914 m, yellow), 6000 ft (1829 m, orange), and 10000 ft (3048 m, light blue).

In addition to beam blockage, other factors need to be considered when utilizing a MEHS event as a proxy for thunderstorm. The radar VCP does not extend beyond 19.5° elevation from horizontal, and thus at very close ranges, is insufficient to sample the mid-and-upper level portions of a storm. The findings from this study showed that MEHS events were generally not detected within approximately 12 km from each radar (note that the Līhu‘e airport weather station is about 24 km from the Kaua‘i WSR-88D).

As has already been mentioned, the WSR-88D MEHS calculations are made over an area extending 230 km from the radar. At longer ranges, beam spreading and beam height cause the resolution of the beam to decrease significantly. For example, at 230 km, the 1° beam is nearly 4 km in diameter. In this case, reflectivity is calculated over a much larger sample volume than close to the radar, which typically leads to a reduction in returned power. Also, assumptions made in the calculations of MEHS at the top and bottom of the VCP may not be valid, particularly if the lowest elevation angle is intersecting the storm above the environmental freezing level. Assuming standard refraction of the radar beam, the lowest elevation angle would be increasingly likely to intersect a thunderstorm above the freezing level at ranges approximately 185 km from the radar. These limitations are evident when viewing a plot of all MEHS events (Figure 4a-e). For this research, I utilized the entire detectable range of MEHS events, though it is relatively trivial to truncate these results to a shorter range if desired, at the expense of a smaller sample set.

a.

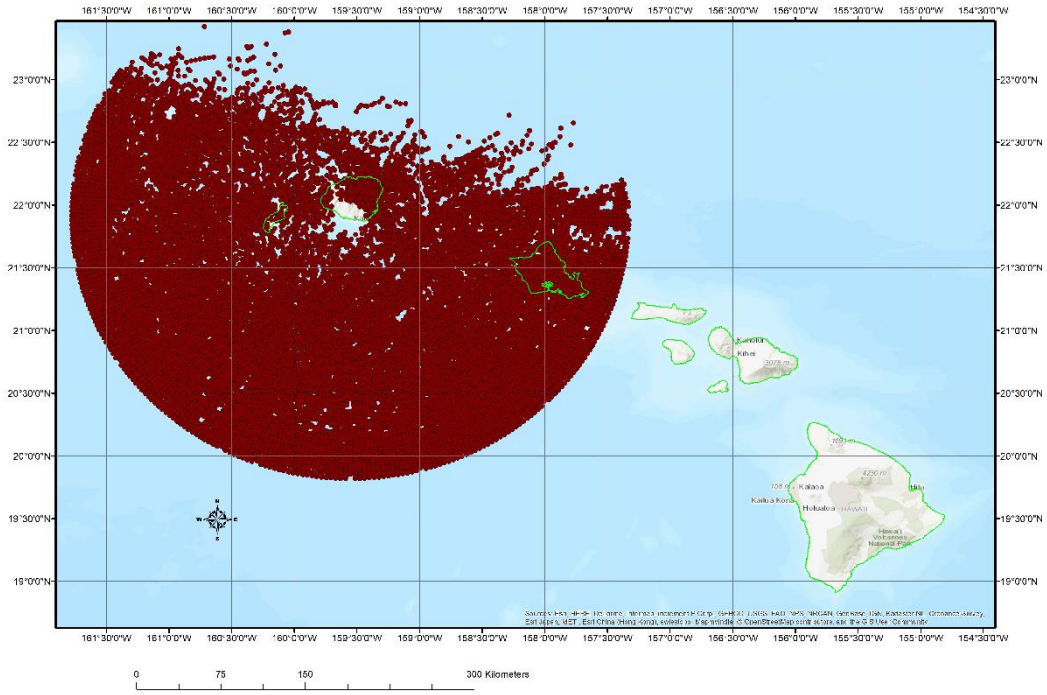
161°30'0"W
161°0'0"W
160°30'0"W
160°0'0"W
159°30'0"W
159°0'0"W
158°30'0"W
158°0'0"W
157°30'0"W
157°0'0"W
156°30'0"W
156°0'0"W
155°30'0"W
155°0'0"W
154°30'0"W
23°0'0"N
22°30'0"N
22°0'0"N
21°30'0"N
21°0'0"N
20°30'0"N
20°0'0"N
19°30'0"N
19°0'0"N
Kaua'i
Kihau
3078 m
4250 m
Kailua-Kona
Hilo
Hawai'i Volcanoes National Park
0
75
150
300 Kilometers

b.

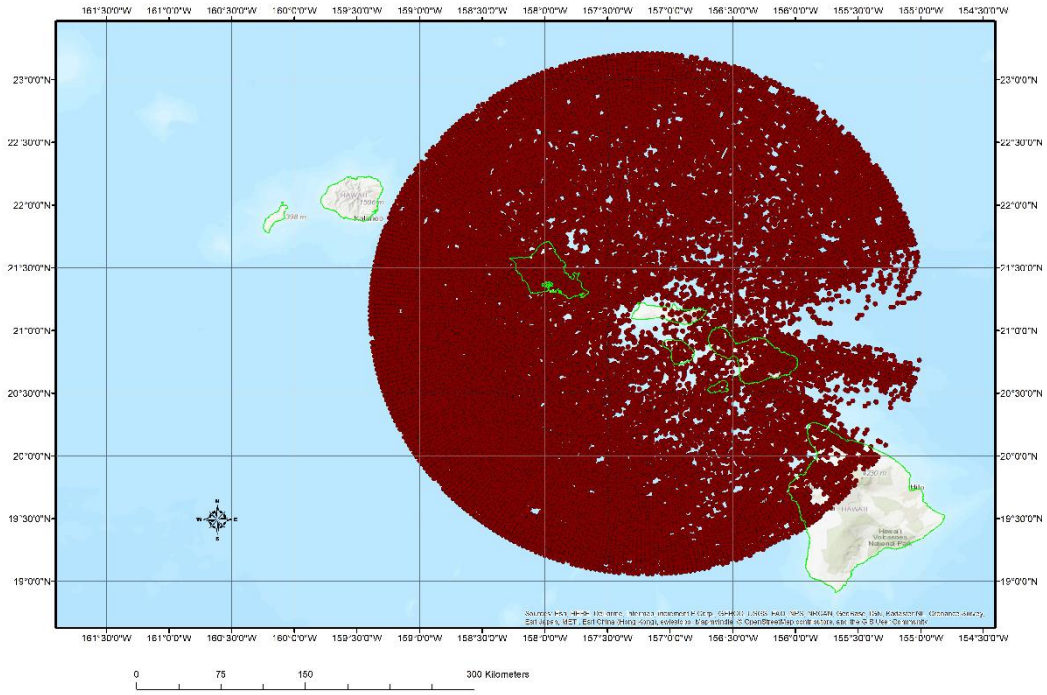
161°30'0"W
161°0'0"W
160°30'0"W
160°0'0"W
159°30'0"W
159°0'0"W
158°30'0"W
158°0'0"W
157°30'0"W
157°0'0"W
156°30'0"W
156°0'0"W
155°30'0"W
155°0'0"W
154°30'0"W
23°0'0"N
22°30'0"N
22°0'0"N
21°30'0"N
21°0'0"N
20°30'0"N
20°0'0"N
19°30'0"N
19°0'0"N
Hilo
Hawai'i Volcanoes National Park
0
75
150
300 Kilometers

c.

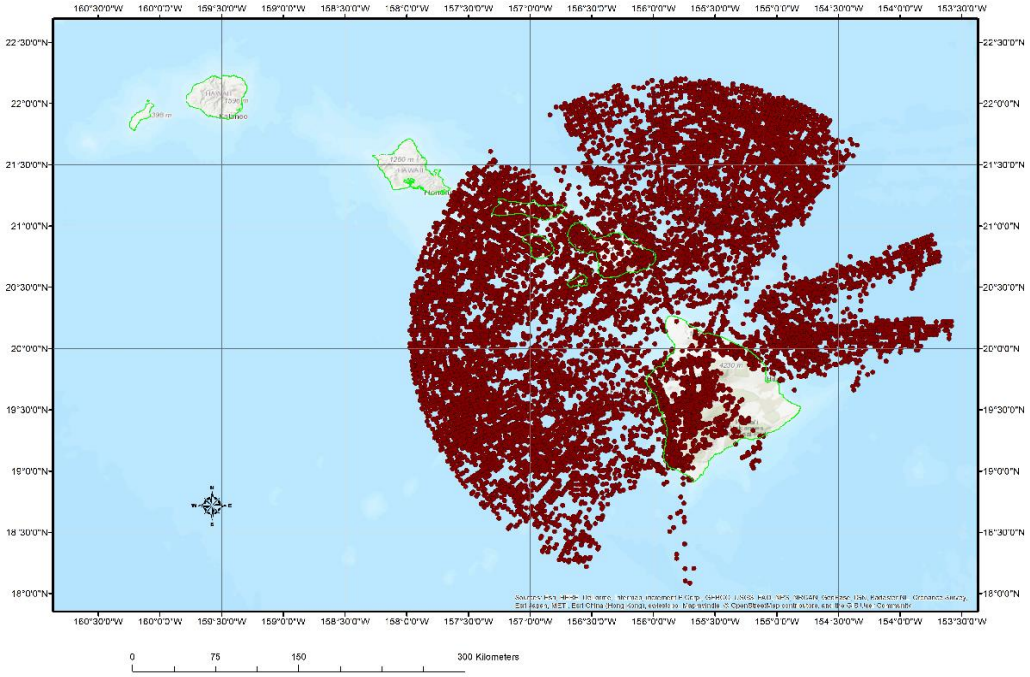
160°30'0"W
160°0'0"W
159°30'0"W
159°0'0"W
158°30'0"W
158°0'0"W
157°30'0"W
157°0'0"W
156°30'0"W
156°0'0"W
155°30'0"W
155°0'0"W
154°30'0"W
154°0'0"W
153°30'0"W
22°30'0"N
22°0'0"N
21°30'0"N
21°0'0"N
20°30'0"N
20°0'0"N
19°30'0"N
19°0'0"N
18°30'0"N
18°0'0"N
0
75
150
300 Kilometers

d.

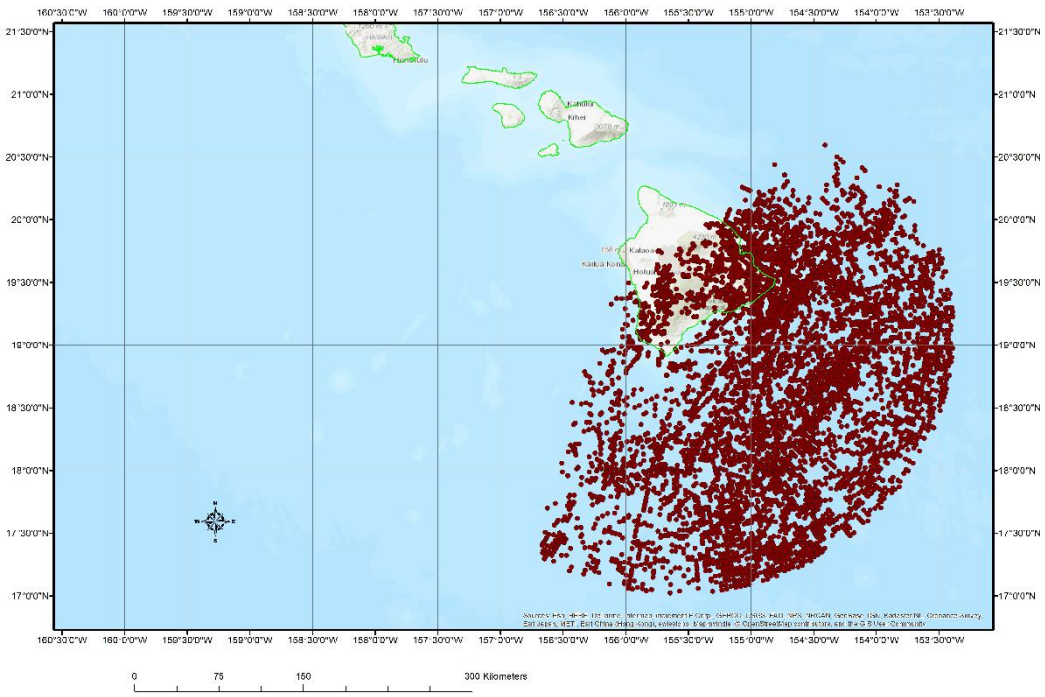
160°30'0"W
160°0'0"W
159°30'0"W
159°0'0"W
158°30'0"W
158°0'0"W
157°30'0"W
157°0'0"W
156°30'0"W
156°0'0"W
155°30'0"W
155°0'0"W
154°30'0"W
154°0'0"W
153°30'0"W
21°30'0"N
21°0'0"N
20°30'0"N
20°0'0"N
19°30'0"N
19°0'0"N
18°30'0"N
18°0'0"N
17°30'0"N
17°0'0"N
0
75
150
300 Kilometers

e.

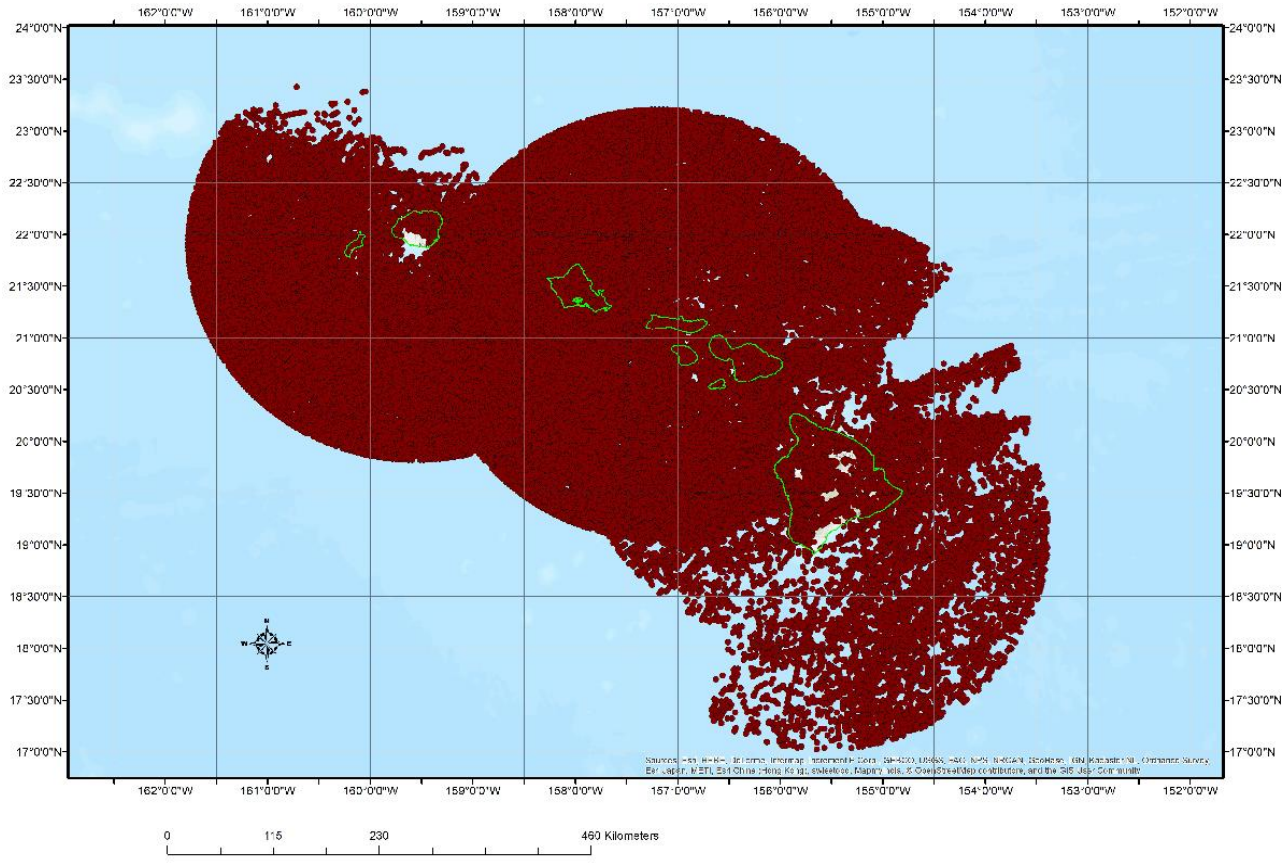

Figure 4. Location of all MEHS events (MEHS ≥ 6 mm, red dots) for 2005-2015, from a) South Kauaʻi radar (PHKI), b) Molokaʻi radar (PHMO), c) North Kohala radar on the Big Island of Hawaiʻi (PHKM), d) Naʻalehu radar on the Big Island of Hawaiʻi (PHWA), and e) composite for all radars.

There are 3 primary ways that the MEHS algorithm can be affected by bad data: chaff, incorrectly calibrated scans, and terrain. These all lead to false returns and needed to be quality controlled, particularly for the more significant events which are climatologically sensitive to bad data. Each of these sources of bad data will be discussed here.

A radar beam (and associated side lobes) intersecting terrain produce intense ground returns (ground clutter). The WSR-88D employs clutter suppression techniques using a combination of data from base reflectivity and base velocity that post-process the data to strongly limit the displayed reflectivity returns caused by terrain in most instances. However, in situations that lead to super-refraction, the clutter suppression may fail. In these cases, NWS personnel can apply even more stringent clutter suppression to the affected areas. Overall, the number of false MEHS returns from ground clutter appear to be fairly low by utilizing these mitigation strategies.

A more significant challenge with using reflectivity-based algorithms comes from chaff. Chaff releases by the military do not appear to be especially common, but can be relatively intense for brief periods, particularly at the onset. This occasionally results in false returns from the MEHS algorithm. In laminar airflow, chaff falls slowly with respect to air (Zrnic and Ryzhkov 2004). Thus, I examined the vertical continuity, and echo motion in relation to other echoes. Starting in 2011 when dual-polarization capability was added to the Hawai‘i WSR-88Ds, it became possible to very easily verify chaff by using the correlation coefficient from the radars to determine if the echo is non-meteorological return. The correlation coefficient (hereafter, CC) is a radar measure of the homogeneity of targets within the sample volume. Sample volumes with all meteorological targets of similar size such as raindrops or ice crystals exhibit a very high correlation coefficient. CC in non-meteorological targets (e.g., chaff, smoke plumes, volcanic ash, etc.) is much lower than in homogenous precipitation returns or in areas where the

precipitation is in mixed phase (Zrnic and Ryzhkov 1999, Zrnic and Ryzhkov 2004). A mix of large and small hailstones and raindrops in the sample volume can result in small local minimums of low CC within a larger field of relatively homogenous high CC. Chaff, however, will show up as a swath of persistently low CC throughout the echo, regardless of high or low reflectivity. Chaff cases typically occurred during quiet weather conditions favorable for aviation operations, and tended to occur on several consecutive days.

Finally, there were a few cases of an individual scan or two having obviously bad calibration. This would manifest itself as a volume scan suddenly having extreme reflectivity in all echoes, with many cells exhibiting very high MEHS values, then immediately returning to typical values in subsequent scans. Sometimes this would happen at the end of a maintenance period immediately after the radar was returned to service.

This study uses a total of 138,751 MEHS events in the SWDI database for 2005-2015. All scans with cells that exhibited MEHS ≥ 19 mm (6,833 total cell scans) were visually examined to ensure that the cells were indeed from a precipitating echo and not from chaff, bad radar calibration, or ground clutter detections. This led to the elimination of 312, or 4.5% of the MEHS ≥ 19 mm cases. When a cell with MEHS ≥ 19 mm was removed from the dataset due to chaff, the associated MEHS event cells from that scan (i.e., ≥ 6 mm), and those in temporally adjacent scans that also exhibited chaff were removed from the total. Chaff events were known to occur on consecutive days. If MEHS events occurred on days adjacent to known chaff events, those MEHS events were similarly checked and removed if needed. All of the quality control procedures discussed led to a removal of a total 997 MEHS event cell scans from the entire dataset. Thus, the vast majority of scans with cells that only have MEHS < 19 mm remain

unchecked. For example, a day with chaff that did not reach a MEHS of 19 mm might not be removed if there were no other nearby days when chaff also caused a MEHS of 19 mm.

2.3 Upper air and Tornado Vortex Signature (TVS) data

The tornado vortex signature (TVS) is a radar-based signature of strong, low-level azimuthal shear evident in the radial velocity imagery over an established depth. It manifests itself as an area of strong gate-to-gate (adjacent in azimuth with range) shear. While radar operators will scan the base data themselves in order to detect a TVS, the WSR-88D has a tornado detection algorithm developed by the National Severe Storms Laboratory (NSSL) which is designed to assist the warning forecaster (Crum and Alberty 1993, Mitchell et al. 1998). The algorithm currently in use is described in detail by Mitchell et al. (1998) and I will summarize it here. It begins by sampling the velocity data along the azimuth and compares it to the velocity data from the next azimuth. "Shear segments" are identified by adjacent velocity gates of a minimum velocity difference. The algorithm default is 11 m s^{-1}. The algorithm then uses six velocity thresholds to isolate core vortices within the shear segments, to construct a two-dimensional (2D) feature. The 2D feature then undergoes a series of checks to ensure it meets certain distance and shape criteria (including an aspect-ratio check to filter elongated features like gust fronts). After all 2D features have been collected for each radar elevation within a given volume scan, a vertical continuity check of the features is done with other volume coverage pattern slices to establish that the feature is three-dimensional (3D). Some allowance is made in the 3D check to account for limited poor velocity dealiasing and range folding, and as well as for updraft tilting common in supercells. Finally, for those volume elements meeting the following criteria, a TVS is assigned when:

1. The base of the feature extends to a prescribed lowest elevation angle or altitude (typically 0.5° or 600 m, respectively).
2. The minimum lowest level azimuthal velocity difference is at least 25 m s^{-1}.
3. The minimum azimuthal velocity difference at some elevation angle within the storm is at least 36 m s^{-1}.
4. The depth of the detectable shear feature exceeds 1.5 km.

The values for 2 and 3 are adaptable at the radar control consoles (Appendix A). NWS offices are provided suggested values for use during four types of storm situations, based on tests of algorithm performance. However, in practice, adjustments to these values require prior approval, and are not typically changed "on the fly."

The algorithm, and the sampling of velocity in tornadic circulations in general, does have several noteworthy considerations. These are covered in more detail in Mitchell (1998), Wood and Brown (1997), and others, and will be summarized here. First, tornadic circulations sometimes last less than the time needed to complete the volume scan, even in faster volume coverage patterns. Poor velocity data quality can also affect algorithm detection. Missing or range folded velocity is not included in the calculations and, in some cases, can cause missed detections. Echoes at longer ranges typically return lower peak velocities doe to beam spreading resulting in larger sample volumes with each range bin. The discrete azimuthal sampling of the WSR-88D also affects the velocity magnitudes, based on the location of maximum rotational velocities in relation to the beam center. These magnitudes can appear to fluctuate significantly from scan to scan, even in a vortex of unchanging rotational velocity.

Terrain poses a number of challenges to algorithm performance as well. This is a challenge for radar detection of tornadic circulations over the relatively complex terrain of

Hawai‘i, since all four radars experience some lower-elevation blockage from terrain (e.g., Figure 3). Partial or complete blockage of the lower elevation angles in some radials likely result in an unknown number of missed detections. Even in the absence of blockage, terrain can cause serious problems. Extremely noisy and incorrect base data can occur where the beam, or its side lobes, intersect terrain. Although the WSR-88D employs clutter reduction techniques to mask this type of bad data from the operator and from the radar post-processing algorithms, variations in atmospheric refraction can still result in many situations where noisy reflectivity and velocity data are displayed and make their way into the computations. Even with the algorithm checking for vertical continuity, some false TVS events occur. This requires checking the velocity and reflectivity data from any returned indications of TVS in order to ensure false returns do not make their way into the dataset.

A legitimate TVS indicates strong and possibly tornadic rotation. However, the scan strategy of the WSR-88D, as well as the default adaptable parameter values already mentioned, are not optimum for detecting non-supercell tornadoes, such as squall line funnels and most tornadoes associated with tropical cyclones. In these instances, a mid-level mesocyclone is usually not the primary mechanism for tornadogenesis. Instead, much of the vorticity generation for tornadogenesis occurs near or below sub-cloud level along shallow, pre-existing boundaries (Wakimoto and Wilson 1989). This precludes tornado detection in Hawai‘i in many instances. For example, the Kapolei tornadoes on February 11, 2009 formed along a rapidly-developing but short-lived thunderstorm that initiated along a sea breeze boundary. The TVS algorithm did not identify this cell, nor was rotation evident from the high-resolution radar imagery available at the NWS in Honolulu. The TVS algorithm performs better with cells exhibiting rotation of considerable depth. Finally, in some situations, larger tornadic circulations very close to a radar

(< 20 km) may not trigger the algorithm (Mitchell et al. 1998). In these instances, the intense shear may not be "gate to gate."

Unfortunately, all of these considerations make it impossible to do a straightforward comparison with the prior work of Price and Sasaki (1965), Schroeder (1977), and Tanabe (2000). Although the radar-based TVS signatures are more likely to be significant tornadoes or waterspouts, it is impossible to verify many of them, and most brief, small funnel clouds or waterspouts occur in the absence of a TVS. Despite these limitations, some general observations and statements about the frequency and locations of strong circulations associated with convective cells can be made using this quality-controlled data set.

All 609 algorithm detected TVSs from the Hawai‘i radars from 2005-2015 were examined. Each TVS was checked to see if the feature exhibited temporal and/or vertical continuity, and was associated with precipitation. Out of this number, 526 (86%) of the TVSs were attributed to bad data, typically due to excessive noisy data near terrain in a variety of conditions. On the other hand, in some cases, a single thunderstorm was responsible for multiple TVSs, increasing the confidence that the storm was exhibiting supercell characteristics.

Chapter 3. Results

3.1 Antecedent sounding parameters associated with surface reports of thunder at Līhuʻe.

The first goal this study involves establishing a baseline climatology of sounding parameters for observed thunderstorms at the Līhuʻe airport. In addition to being important for a historical understanding of the parameter space for thunderstorms in Hawaiʻi, the results from this part are later compared to a similar pairing of sounding parameters with radar MEHS events. The results here include all cases where thunder was reported at the Līhuʻe airport within 12 hours after the sounding was taken (i.e., the antecedent sounding). This dataset includes cases from 1973 to 2015 and reflects 274 soundings, representing a variety of synoptic situations and various levels of storm organization. For this portion of the study, which extends well before the weather radar era, no attempt is made to categorize the reports by storm organization or severity, since there is no definitive way of knowing what conditions existed around the time of the observations.

The results for this section are shown in the box and whisker diagrams in Figure 5. When considering these plots, it is important to keep a few things in mind. Although the diagrams show *typical* values for thunderstorms at Līhuʻe, one should remember that *ideal* values for convection can extend well beyond the ranges indicated here (i.e., colder aloft, more unstable, more moisture). On the other hand, thunderstorms with less than typical values of moisture and/or instability may tend to reflect situations where synoptic forcing is stronger. The same is true for instability when compared with moisture: Individual cases in the dataset sometimes showed that when one type of parameter was ideal, the others would be marginal. For example, thunderstorms aided by very cold air aloft were not typically accompanied by large amounts of

moisture, and thunderstorms in regimes of excessive moisture were often accompanied by relatively warm air in the mid-levels.

The results show that thunderstorms at Līhu‘e tend to occur only when much higher values of MLCAPE are achieved compared to the “ordinary” thunderstorm category (i.e., thunderstorms not associated with tornadoes, damaging winds, or large hail) over the continental United States (CONUS) established by Rasmussen and Blanchard (1998). A median value of 1186 J kg^{-1} was found for Līhu‘e, but over the CONUS the value was less than half, at 537 J kg^{-1}. In fact, their median value is below the 25th percentile value of 702 J kg^{-1} at Līhu‘e. This difference indicates that typically, much greater instability is needed for thunderstorms in Hawai‘i to compensate for typically weak synoptic forcing environments that are less likely to lift parcels to the level of free convection. Mixed-layer CAPE (MLCAPE) values greater than about 2200 J kg^{-1} comprise the top 10% of cases at Līhu‘e, compared to about 1800 J kg^{-1} for “ordinary” thunderstorms on the CONUS.

The values for 0-6 km bulk shear magnitude (i.e., the magnitude of the shear vector between the surface wind and the wind at 6 km, hereafter “0-6 km shear”) at Līhu‘e for pre-thunderstorm cases are strikingly similar to the results presented by Rasmussen and Blanchard for the “ordinary” thunderstorm cases. It is interesting to see that the top 10% of 0-6 km shear values for pre-thunderstorm cases are accompanied by values in excess of 21.6 m s^{-1} (i.e., 3.6×10^{-3} s^{-1}). This suggests an environment that may be supportive of longer-lived updrafts and the possibility for severe weather. The 0-3 km storm relative helicity (SRH) values (assuming storm motion from Bunkers (2000)) are also quite similar to the Rasmussen and Blanchard findings, with the values at the higher end of the data more often found in environments typical of supercells. The relatively shallow 500-700 hPa lapse rates support the idea that deep convection

in Hawai‘i is generally characterized by weak updrafts, especially compared to continental thunderstorm environments where values can approach dry adiabatic if an elevated mixed layer is present. As other authors have noted, (Lucas et al. 1994a, b, Zipser 1994, Blanchard 1998, Barnes 2001) even relatively large values of CAPE can yield weak updraft speeds if the same magnitude of CAPE is distributed through a deep free convective layer (so called thin or "skinny" CAPE).

It is also useful to compare the values in Figure 5 with climatology, in order to have some idea of which of these data are useful discriminators for the prediction of thunderstorms. The long term (1973-2016) climatology of many of the parameters in Figure 5 is given in Appendix C. Since a thunderstorm is a relatively rare event at any given location in Hawai‘i, the long-term climatology will largely reflect soundings without convection. There is no overlap between the 75th percentile value of MLCAPE for climatology (529 J kg^{-1}) versus the pre-thunderstorm soundings (702 J kg^{-1}). The same is true for K-index, with 18 and 25, respectively. For lifted index, the climatological 25th percentile value is -1.7°C, but for pre-thunderstorm soundings, the 75th percentile value is -2.7°C. Finally, for precipitable water, the 75th percentile value of climatology is 35.3 mm, while the 25th percentile for pre-thunderstorm soundings is 36.2 mm. These appear to be the best discriminators among the reviewed data to determine if thunderstorms are a possibility.

Some of the parameters appear to show less skill, with more overlap between climatology and pre-thunderstorm conditions. The 500 hPa geopotential heights dip to 583 dm at the 25th percentile of climatology, while the 75th percentile for pre-thunderstorm soundings is 584 dm. Similarly, the 25th percentile for climatology of 700 hPa geopotential height is 3145 m, but for pre-thunderstorm soundings, the 75th percentile is 3158 m. For both 500 hPa and 700 hPa

temperatures, there is only small overlap between the climatological 25th percentiles and 75th percentiles for pre-thunderstorms. It may be useful to further investigate changes in these parameters with time, rather than focusing on an individual sounding.

The 500 to 700 hPa lapse rate is not a good discriminator for potential thunderstorm situations. There is very little difference in the climatological values versus pre-thunderstorm soundings. Hawai‘i’s long distance from any continents (particularly those with high terrain that can yield steep mid-level lapse rates through advection of elevated mixed layers), and relatively weak temperature gradients overall, make it quite difficult to yield steep mid-level lapse rates, which can be favorable for stronger convective updrafts. Both datasets showed that it was rare for the 500 to 700 hPa lapse rate to exceed 6.9°C km^{-1} (90th percentile).

Two parameters which have been typically more utilized for determining severe versus non-severe thunderstorms were also compared to climatology. The SWEAT index showed small overlap from the 75th percentile of climatology versus the 25th percentile of pre-thunderstorm soundings. Interestingly, the pre-thunderstorm 0-6 km shear, although slightly higher for pre-thunderstorm soundings, showed considerable overlap with the long term climatology.

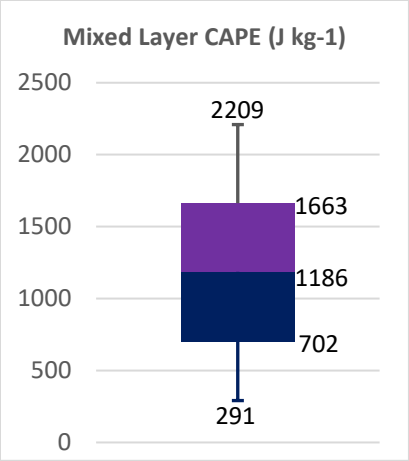
Mixed Layer CAPE (J kg-1)
2500
2000
1500
1000
500
0
2209
1663
1186
702
291

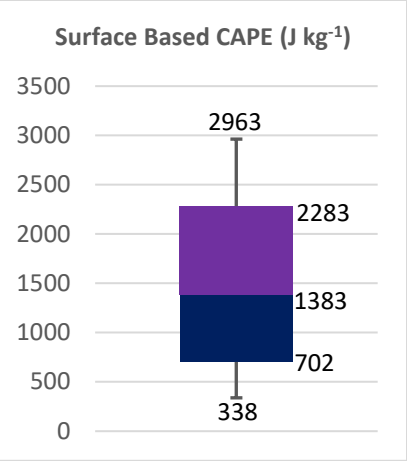
Surface Based CAPE (J kg-1)
3500
3000
2500
2000
1500
1000
500
0
2963
2283
1383
702
338

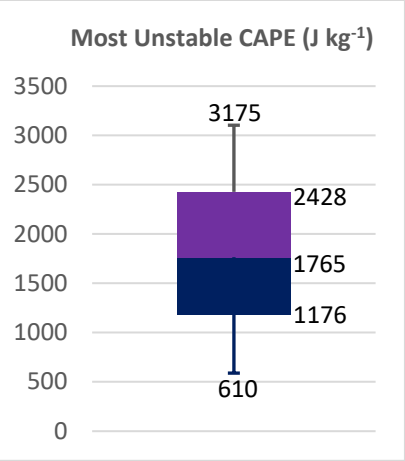
Most Unstable CAPE (J kg-1)
3500
3000
2500
2000
1500
1000
500
0
3175
2428
1765
1176
610

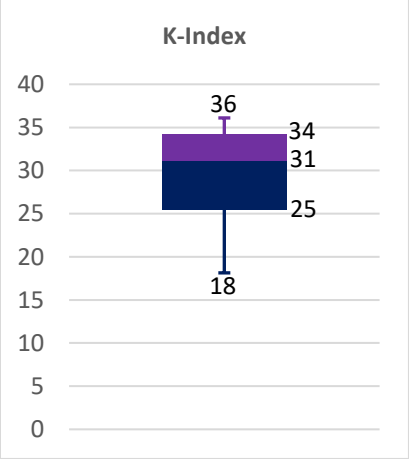
K-Index
40
35
30
25
20
15
10
5
0
36
34
31
25
18

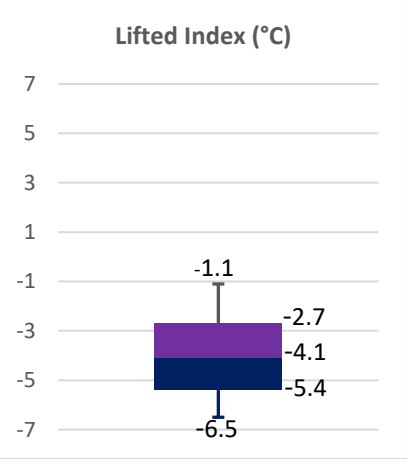
Lifted Index (°C)
7
5
3
1
-1
-3
-5
-7
-1.1
-2.7
-4.1
-5.4
-6.5

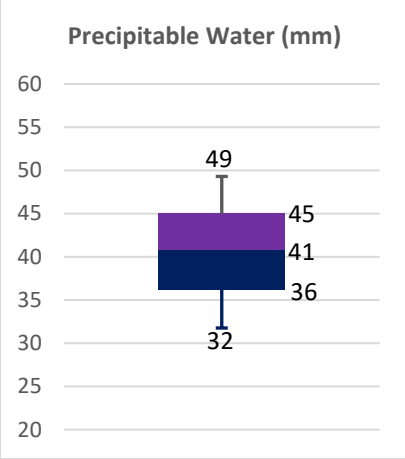
Precipitable Water (mm)
60
55
50
45
40
35
30
25
20
49
45
41
36
32

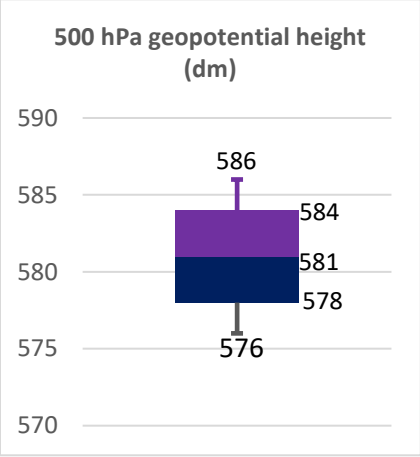
500 hPa geopotential height (dm)
590
585
580
575
570
586
584
581
578
576

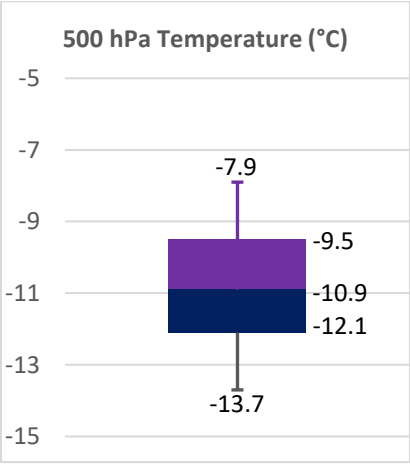
500 hPa Temperature (°C)
-5
-7
-9
-11
-13
-15
-7.9
-9.5
-10.9
-12.1
-13.7

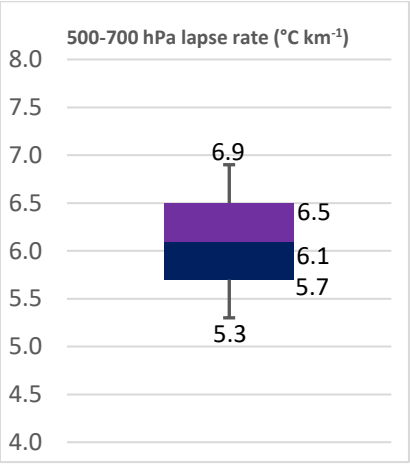
500-700 hPa lapse rate (°C km-1)
8.0
7.5
7.0
6.5
6.0
5.5
5.0
4.5
4.0
6.9
6.5
6.1
5.7
5.3

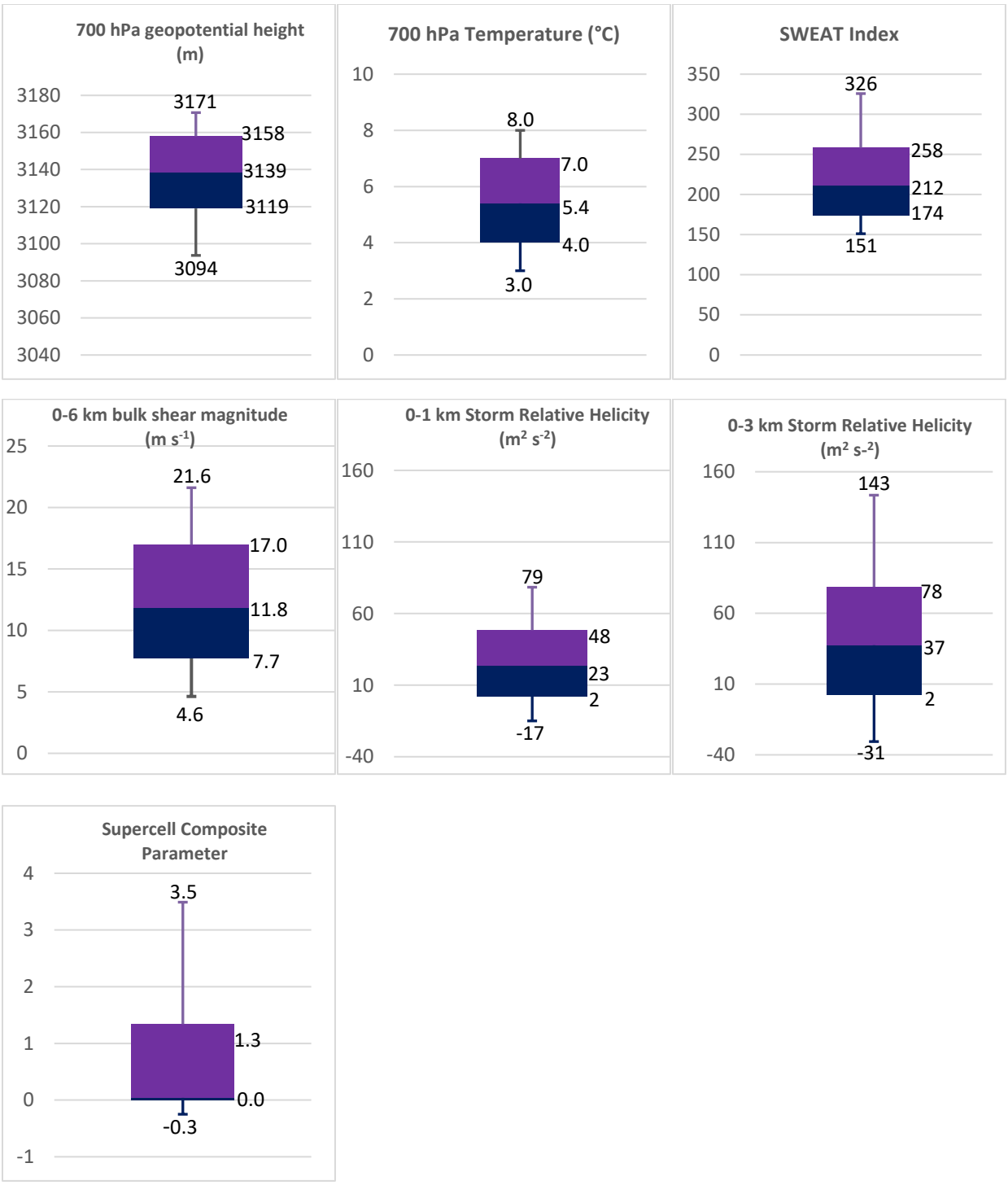

Figure 5. Box and whiskers plots of parameters associated with soundings antecedent to observations of thunder at Līhuʻe (1973-2015). The darker box extends to the 25th percentile, while the lighter box extends to the 75th percentile. The median is indicated at the division of the colored boxes. Thin bars ("whiskers") extend to the 10th and 90th percentiles.

3.2 Antecedent sounding parameters associated with MEHS events near Līhuʻe.

A study of antecedent soundings when associated with the radar-based thunderstorm proxy should yield results similar to the comparison between soundings and observed thunder cases, so long as the proxy detection is within a relatively small distance from the observation site. For this comparison, I used MEHS events from 2005-2015 within a 30 km ring around the Līhuʻe observation site are used to approximate a thunderstorm. The results are shown in Figure 6. For most parameters, the median antecedent sounding values for proximity MEHS events are within 5% of those found by comparing soundings to observed thunder. For SWEAT, 0-3 km storm relative helicity, and lifted index, the median values were within 10%. For comparison, the results for MEHS events within 40 and 80 km from Līhuʻe, and any MEHS event (within 230 km of the radar) were also obtained. Table 3 shows the median sounding parameters for observed thunder, for MEHS within 30 km, and for MEHS event within 230 km of the radar (40 and 80 km are not shown). Not surprisingly, when the radius of detection increased significantly, most of the sounding parameters indicated less stringent conditions were necessary.

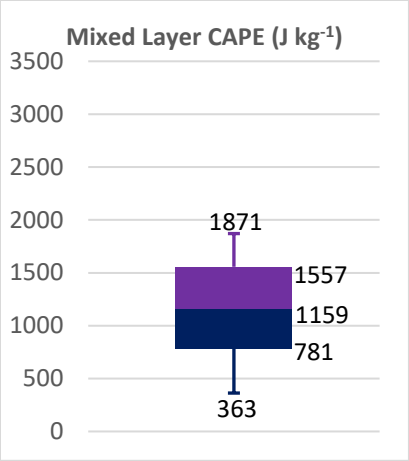
Mixed Layer CAPE (J kg-1)
3500
3000
2500
2000
1500
1000
500
0
1871
1557
1159
781
363

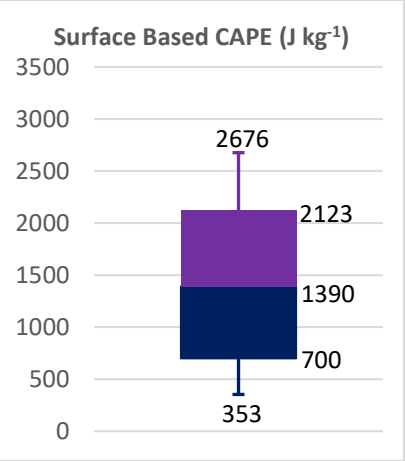
Surface Based CAPE (J kg-1)
3500
3000
2500
2000
1500
1000
500
0
2676
2123
1390
700
353

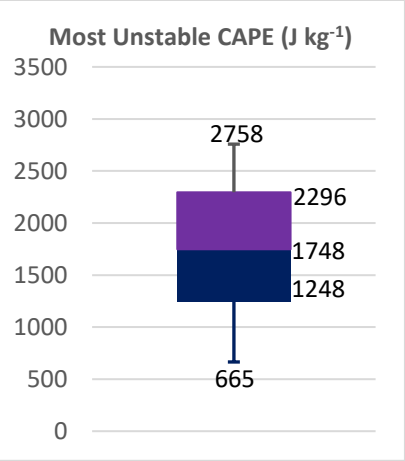
Most Unstable CAPE (J kg-1)
3500
3000
2500
2000
1500
1000
500
0
2758
2296
1748
1248
665

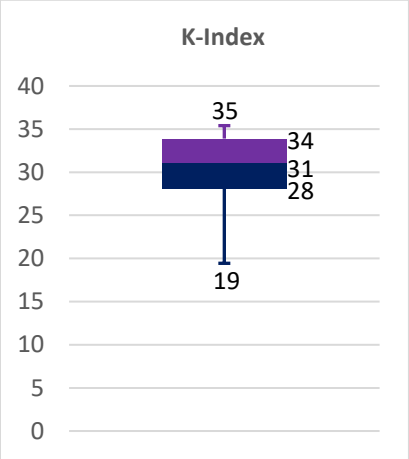
K-Index
40
35
30
25
20
15
10
5
0
35
34
31
28
19

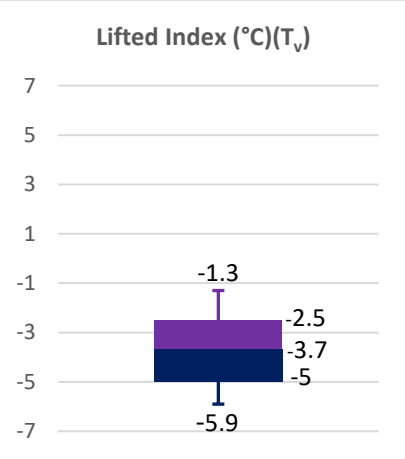
Lifted Index (°C)(Tv)
7
5
3
1
-1
-3
-5
-7
-1.3
-2.5
-3.7
-5
-5.9

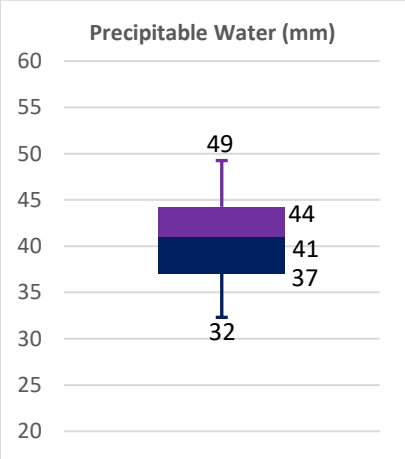
Precipitable Water (mm)
60
55
50
45
40
35
30
25
20
49
44
41
37
32

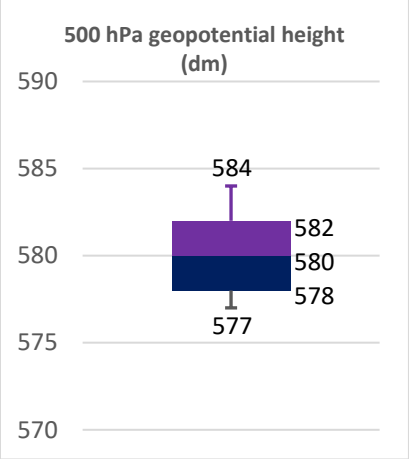
500 hPa geopotential height (dm)
590
585
580
575
570
584
582
580
578
577

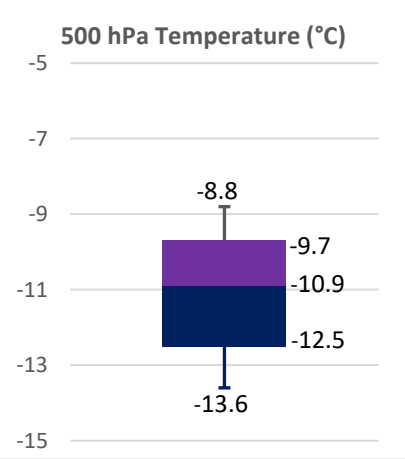
500 hPa Temperature (°C)
-5
-7
-9
-11
-13
-15
-8.8
-9.7
-10.9
-12.5
-13.6

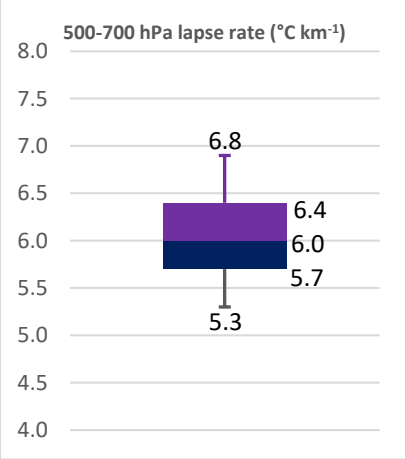
500-700 hPa lapse rate (°C km-1)
8.0
7.5
7.0
6.5
6.0
5.5
5.0
4.5
4.0
6.8
6.4
6.0
5.7
5.3

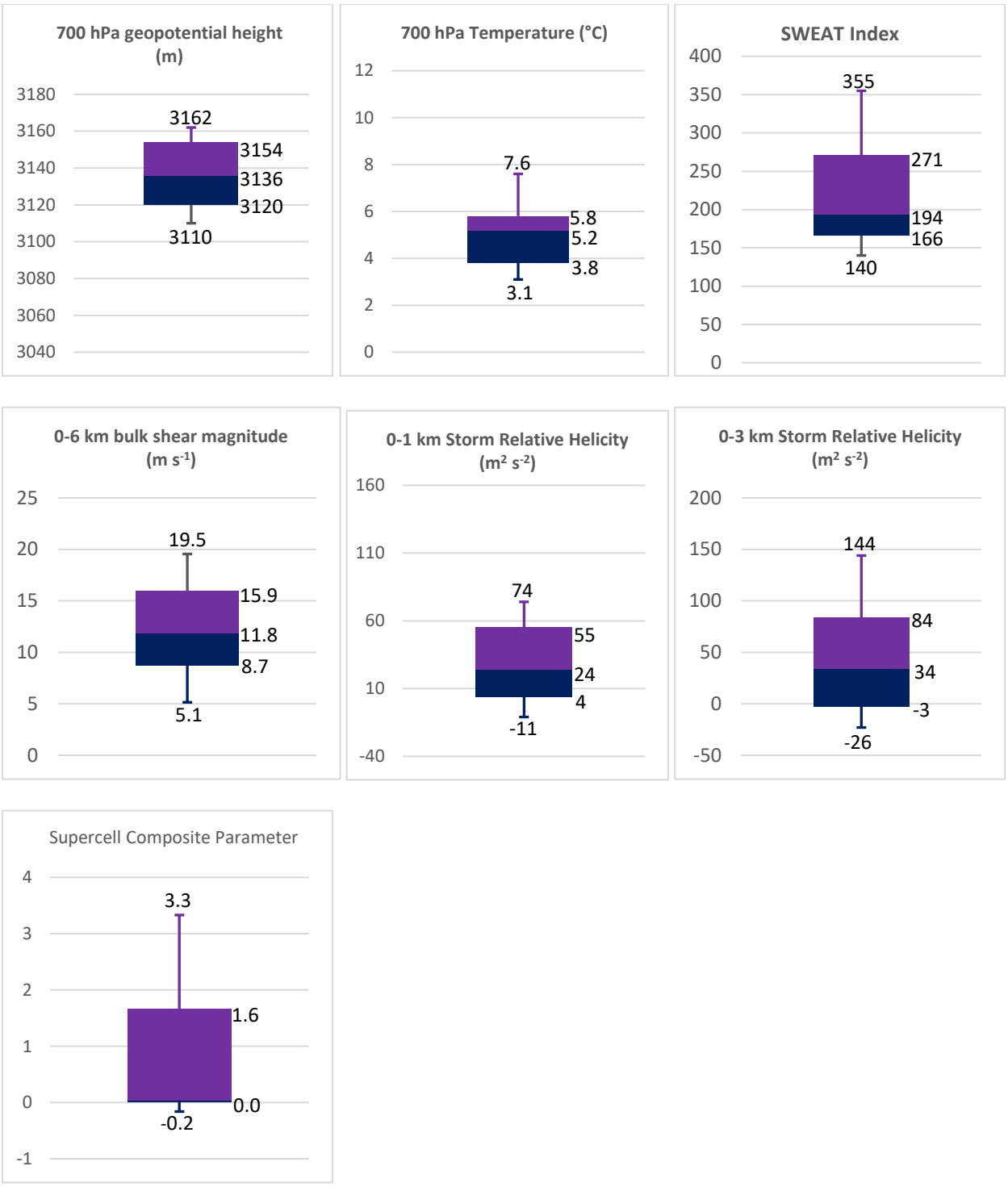

Figure 6. As in Figure 5, but for MEHS events (MEHS ≥ 6 mm) within 30 km of the Līhu‘e observation site.

Table 3. Comparison of median PHLI antecedent sounding parameters for observed thunder, MEHS events within 30 km of Līhu‘e, and MEHS events within 230 km of the Kaua‘i radar (PHKI).

Parameter	Observed thunder	MEHS within 30 km of Līhu‘e	MEHS within 230 km of PHKI
MLCAPE (J kg^{-1})	1186	1159	796
SBCAPE (J kg^{-1})	1383	1390	1046
MUCAPE (J kg^{-1})	1766	1748	1340
K-Index	31	31	28
Lifted Index (°C)	-4.1	-3.7	-2.8
Precipitable Water (mm)	41	41	38
500 hPa geopotential height (m)	5810	5800	5810
500 hPa temperature (°C)	-10.9	-10.9	-10.4
500-700 hPa lapse rate (°C km^{-1})	6.1	6.0	6.0
700 hPa geopotential height (m)	3139	3136	3144
700 hPa temperature (°C)	5.4	5.2	5.4
SWEAT index	212	194	183
0-6 km bulk shear magnitude (m s^{-1})	11.8	11.8	10.8
0-1 km storm relative helicity (m^2 s^{-2})	23	24	20
0-3 km storm relative helicity (m^2 s^{-2})	37	34	27
Supercell composite parameter	0	0	0

3.3 MEHS event climatology

3.3.1. All MEHS events (≥ 6 mm)

In order to establish when MEHS events occur in Hawai‘i, their monthly distribution is given in Figure 7 for each of the radars. The data reveals the well-known pattern of wet and dry seasons in Hawai‘i, with events strongly favoring November through May. The total number of cases for all radars for June through October makes up only about 10% of the annual total. For 10 of the 12 months, PHMO had the highest number of occurrences when compared to the other three radars. However, this is probably not due to the radar being in a relative maximum of activity. When examining all MEHS events for each radar in plan view (Figure 4), one can see beam blockage is likely a major factor in masking event occurrences in some areas. An examination of individual radials from each radar shows that about 39% of the radar radials from PHKI exhibit some blockage, 9% for PHMO, 43% for PHKM, and 53% for PHWA. When attempting to account for the amount of blocked area (assuming homogenous coverage within), the density and total number of events decreases for each radar from west-to-east.

There are some interesting results from the number of MEHS events within the wet season as well. From October to November, there is a sharp increase in the number of events for the western half of the state, and more modest increases for the eastern half. The increase for western areas is likely due to the increase in the number of extratropical weather systems that affect the area at that time. Systems like these commonly affect Kaua‘i and O‘ahu, but stall or dissipate before reaching the southern islands (Blumenstock and Price 1967, Schroeder 1993), which may also account for the apparent decrease in total number of MEHS events around the

Big Island discussed previously. The increase is more pronounced for the Big Island radars in December, which is also when a peak number of MEHS events occurred.

The spike in events for March on the PHKI and PHMO radars is notable, and reflective of two very active periods. The first was through much of March 2006 (a.k.a., the so-called "40 Days of Rain" which continued into April). The second is the period from March 3-10, 2012. If the totals for these two months were omitted, the overall March total would be comparable to the total MEHS events for February and April. It is difficult to tell from this 11-year period whether March is climatologically a more active month. It is possible that with March being a transition season, that it favors more active weather systems near Hawai‘i. This also may explain a relative minimum in MEHS events for the Kaua‘i and Moloka‘i radars in January and February, compared to November, December, and March. However, there is extreme variability in any given March, with total events for the period ranging from less than 5 (2005, 2010), to greater than 5000 (2006, 2012).

When looking at the hourly distributions of MEHS events (Figure 8), one can see some similar characteristics for three of the four radars. For PHKI, PHMO, and PHKM, there is a strong tendency toward nocturnal events, very similar to that found for rainfall frequency over windward land areas by Schroder et al. (1977). The hourly peak for all three of those radars was between midnight and 1 am, with a midday minimum between 11 am and 1 pm. Only about half to two-thirds as many events occurred during the minimum period, compared to the maximum hours. The results for the PHWA radar were significantly different, exhibiting considerably less diurnal variability. There is a minor peak around daybreak, with a minor minimum in the early evening.

Another interesting feature that shows up in the hourly distributions for PHKI, PHMO, and PHKM is a minor peak in the mid-afternoon between 3 and 5 pm. This is likely due to convection that forms over the island interiors on when trade winds are absent and the air is moist and unstable. For PHKI and PHMO, there is a short decrease an hour after the peak, before the overall trend increases into the nighttime hours. However, at PHKM, which covers more land area and thus likely exhibits a more dominant upslope/downslope signal on the totals, there is a gradual decrease that lasts until mid-evening. The PHWA radar, which has considerable blockage over land, shows a negligible afternoon peak.

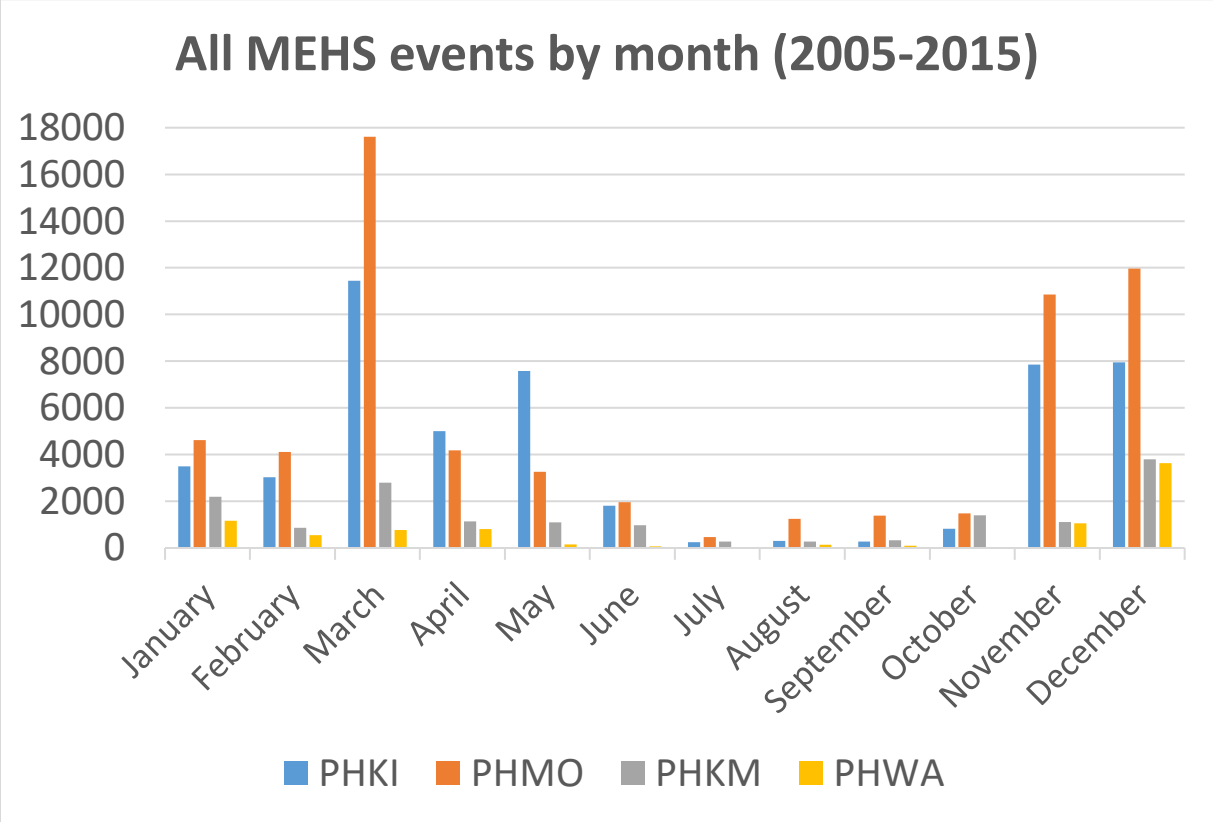

Figure 7. Monthly distribution of MEHS events for each radar, 2005-2015.

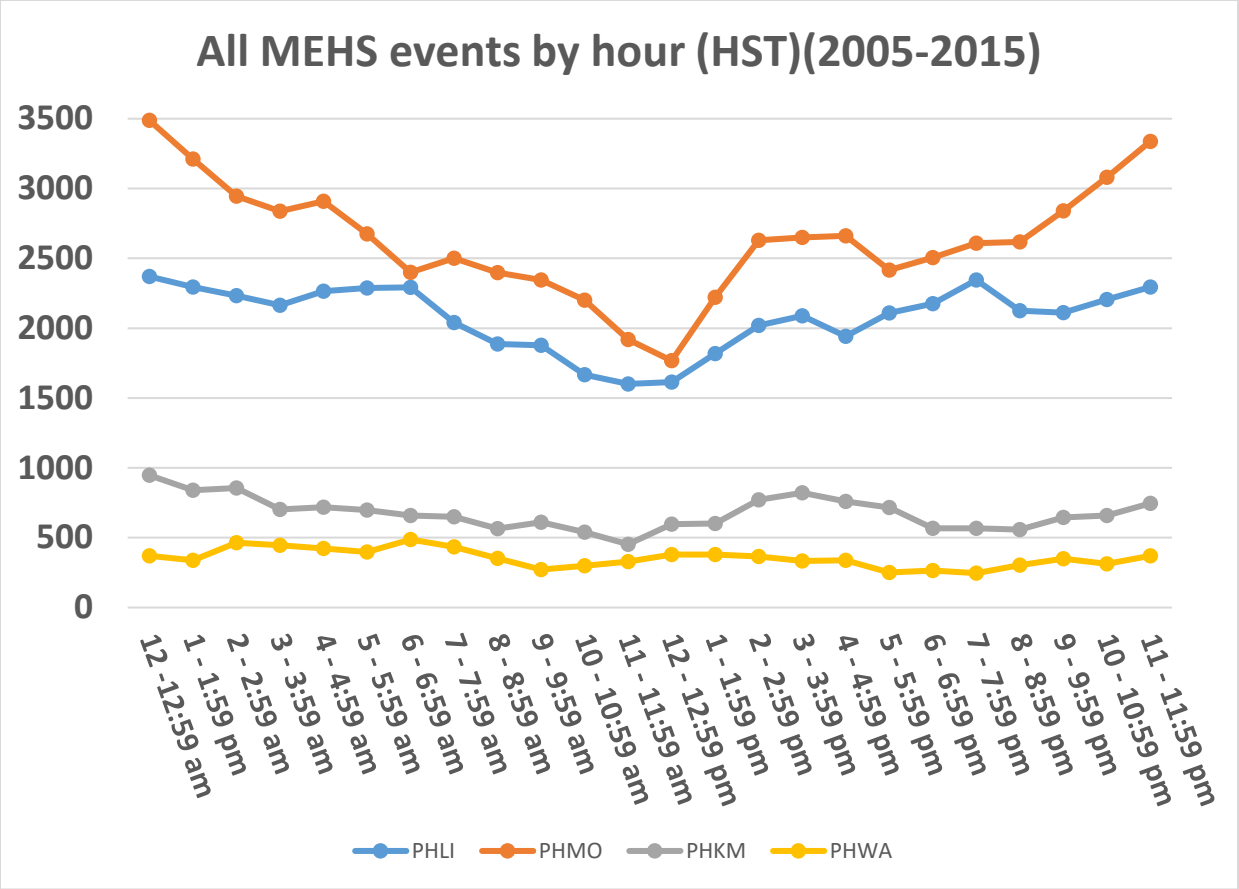

Figure 8. Hourly distribution of MEHS events for each radar, 2005-2015.

A plan-view mosaic of the average annual distribution of MEHS event days around Hawai‘i and surrounding waters is shown in Figure 9. The MEHS event thunderstorm proxy was developed using a 30 km radius around Līhu‘e. In order to maintain consistency with the area considered when looking at a view of the entire state, the MEHS event data were gridded using an approximate equal area for each grid box (about 2827 km^2). This allows for comparisons with reported annual thunderstorm day values at the first order stations. The maximum value reported from any of the radars was used for grid boxes with more than one radar-based value. Caution should be used when interpreting this grid. Grid boxes at the edge of the radar range are unrepresentative of the total number of MEHS events that would occur in that box. The same is

true for areas affected by beam blockage that do not have the benefit of another radar to adequately cover.

When accounting for these limitations, some interesting features appear. There are relative maxima in average annual MEHS event days over the islands of Kaua‘i and O‘ahu, and over the interior of the Big Island. The relative maximum to the west of the islands may be due to downwind convergence zones. There is a general decrease in the number of events from northwest to southeast, consistent with the findings of Blumenstock and Price (1967) that note a decreasing number of frontal passages as you go down the chain from west to east. The gridded MEHS event annual average values centered over four first-order climate stations appear to be relatively consistent with the observed thunderstorm day values obtained from the NCEI Local Climatological Data values for the same period (Table 4), when considering resolution and accounting for beam blockage (i.e., over Hilo).

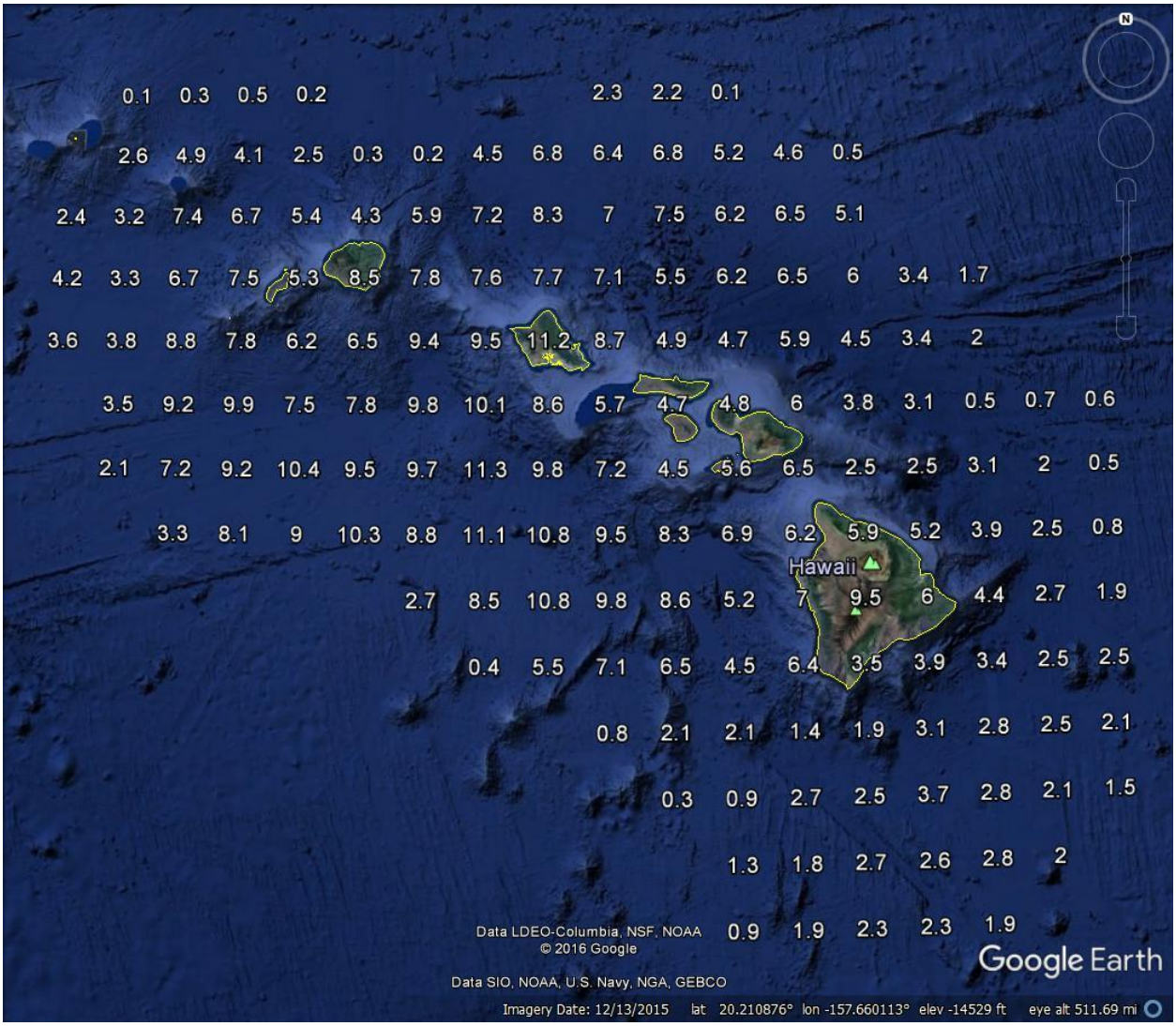

Figure 9. Gridded average annual MEHS event days 2005-2015.

Table 4. Comparison of average annual thunderstorm days 2005-2015 for the four first order stations versus the corresponding gridded values centered on each site.

Observation site	Average annual t-storm days (2005-2015)	Average annual MEHS event days (2005-2015)
Līhu‘e airport (PHLI)	9.4	8.6
Honolulu airport (PHNL)	10.2	10.4
Kahului airport (PHOG)	1.0	5.0
Hilo airport (PHTO)	9.2	6.4

3.3.2 Larger MEHS occurrences (>13 mm)

To investigate more significant events, I study cells exhibiting MEHS larger than 13 mm. I will first present a climatology of these occurrences, as well as a climatology of the same antecedent sounding parameters used previously. While there is no well-defined radar-based threshold for MEHS that differentiates large hail from smaller hail reaching the surface in Hawai‘i, events with large MEHS sizes would correspond to very high reflectivity at unusually high altitudes within a storm. This implies very strong updrafts that are more likely to lead to severe weather. Some NWS guidance to radar operators suggests that, owing to the known overestimation of the MEHS algorithm, 32 mm may be a good warning threshold for severe hail reaching the surface, although this threshold has not been explicitly tested in Hawai‘i.

At this point, it should be reiterated that indications of higher MEHS are only expected to be a proxy for a *subset* of likely severe weather types (most often, damaging downbursts or large hail). Prior authors (e.g., Zipser 1994, Barnes 2001) have shown that, in some cases, lightning can be sparse or non-existent in some cumulonimbi. In fact, some severe weather environments-the so called “high shear, low CAPE” environment are known for having a dearth of lightning (Sherburn and Parker 2014). Thus, an absence of MEHS does not necessarily mean a complete absence of severe weather (particularly damaging winds or tornadoes and waterspouts). Further study will be needed to ensure other cases not represented by high MEHS are considered.

The number of events of all reportable MEHS sizes for each radar for the period 2005-2015 is given in Table 5 as well as the totals. This is also presented as a probability distribution in Figure 10. There is a sharp decline in the number of cases of >13 mm, with these sizes only representing about 5% of the total number of events. For thunderstorms within radar range, MEHS of 32 mm or greater make up a little less than 1% of all cases. For all sizes, the Moloka‘i

radar has the largest number of cases, often exceeding the number of cases of the other 3 radars combined. It is difficult to say with certainty whether this is a function of radar beam blockage, an artifact related to the radars, or if there is a meteorological reason. Blockage alone does not seem to be enough to account for the large difference.

In addition to the total number of cases, it is useful to examine the frequency of these cases. For each radar, the total number of MEHS days for each year (2005-2015) for a given size or larger is given for each year in Table 6, as is the average number of days. The table also shows the average number of days per year with a given size or larger. Although the number of storms with large hail indications on radar is small, it is noteworthy, challenging the assumption that hail will almost always be small in Hawai‘i. The top 1% of total cases as demonstrated in Table 5, 32 mm or greater, were observed 5.5 days per year on average. Prior studies have noted that very large hail (i.e., greater than 51 cm) is generally the result of supercell thunderstorms (Rasmussen and Blanchard 1998; Barnes 2001). One can thus infer that at least one day per year, on average, includes the possibility for supercell thunderstorms within radar range. This may be a conservative estimate, however, as many (and perhaps most) supercell thunderstorms do not produce very large hail (Rasmussen and Blanchard 1998).

Table 5. MEHS cell-scans (2005-2015) distributed by size for each radar, as well as the total.

MEHS size (mm)	PHKI	PHMO	PHKM	PHWA	total
≤ 13	47877	59701	15509	8142	131229
19	1433	2213	490	283	4419
25	324	677	140	54	1195
32	100	300	48	17	465
38	42	112	25	7	186
44	19	53	13	1	86
51	13	33	6	0	52
57	7	21	8	1	37
64	6	12	4	0	22
70	1	13	1	0	15
76	3	12	0	0	15
83	4	10	0	0	14
89	1	4	0	0	5
95	1	3	0	0	4
102	0	6	0	0	6

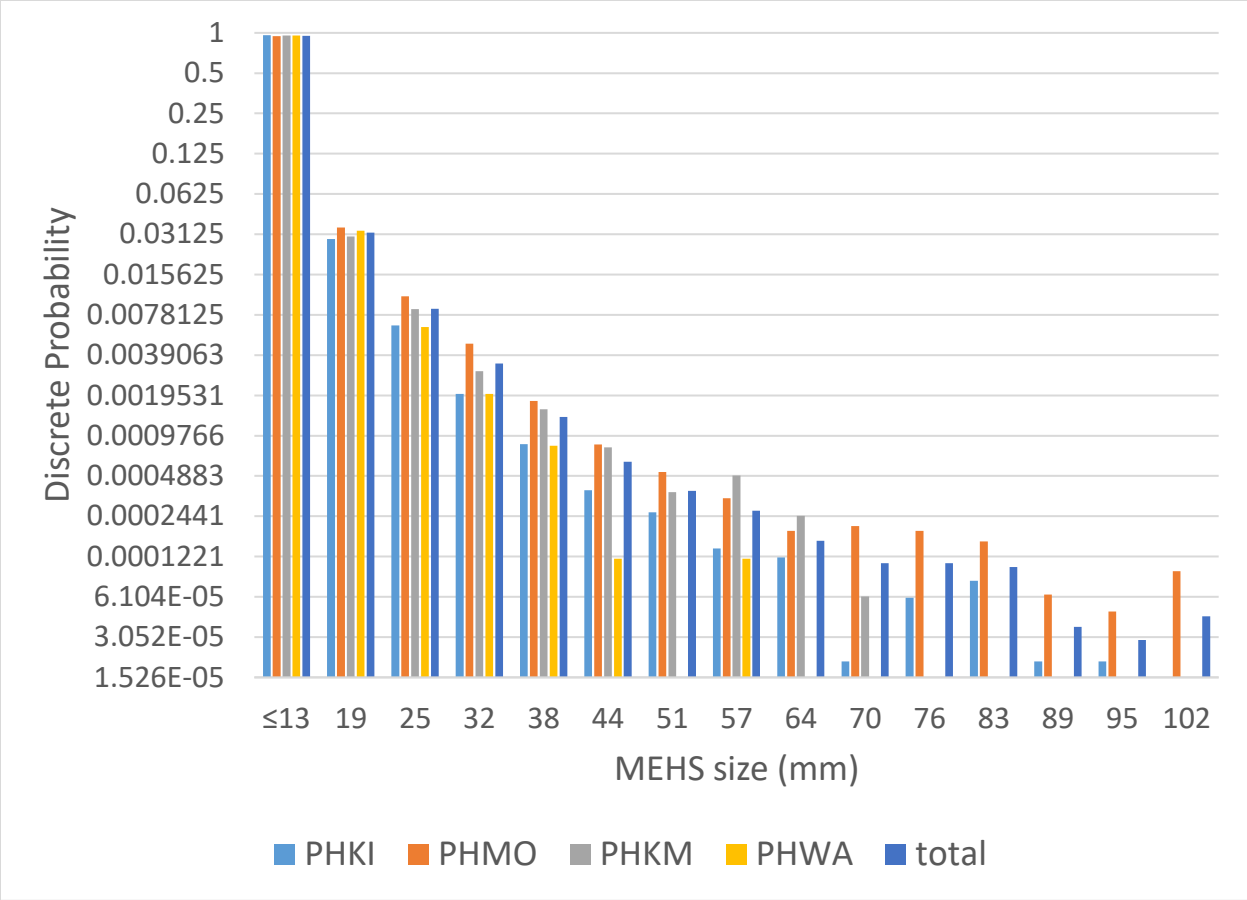

Figure 10. Discrete probability distribution of MEHS size, and total for all cell scan detections.

Table 6. Days per year with MEHS exceeding given sizes (2005-2015). The average number of days per year is shown in the bottom row.

	≥6 mm	≥19 mm	≥25 mm	≥32 mm	≥38 mm	≥44 mm	≥51 mm	≥57 mm	≥64 mm	≥70 mm	≥76 mm	≥83 mm
2005	68	8	5	4	3	3	1	1	0	0	0	0
2006	55	25	17	13	7	5	5	5	4	3	2	0
2007	101	20	11	5	3	1	0	0	0	0	0	0
2008	106	26	14	5	2	1	1	0	0	0	0	0
2009	55	25	14	6	5	4	4	2	1	0	0	0
2010	28	6	2	1	1	1	1	1	0	0	0	0
2011	93	43	28	11	6	3	3	3	3	2	1	1
2012	54	15	8	5	5	3	2	1	1	1	1	1
2013	78	15	8	4	1	0	0	0	0	0	0	0
2014	76	19	9	7	4	2	0	0	0	0	0	0
2015	75	8	2	0	0	0	0	0	0	0	0	0
avg.	***71.7***	***19.1***	***10.7***	***5.5***	***3.4***	***2.1***	***1.5***	***1.2***	***0.8***	***0.5***	***0.4***	***0.2***

The monthly distribution of MEHS ≥ 19 mm cell scans is shown in Figure 11. The overall distribution is very similar to that shown in Figure 7, with activity strongly favored toward the Hawai‘i wet season months of November through April. Once again, there appears to be two relative maxima in the activity. The first peak is in November and December, with relatively fewer cases being observed in January and February. This is followed by a sharp peak in March, and then a decrease in April. The peak in March is largely due to the very active month of March 2006, and the very large single day total on March 9, 2012. If these two situations were omitted, the totals would be much closer to the April values. Monthly distributions of larger values of MEHS were also examined (not shown) and appeared similar to the pattern exhibited by all MEHS events and the ≥ 19 mm cases.

An examination of the hourly distribution of larger MEHS cell scans (Figure 12) shows less of a diurnal signal than for all MEHS cases. The total number of events during the midday hours is similar to the total number of events for the overnight hours, for all radars as well as for all cases within radar range. It may be that stronger synoptic forcing, which would be expected to accompany more intense thunderstorms, may override the typical diurnal signal in weaker events.

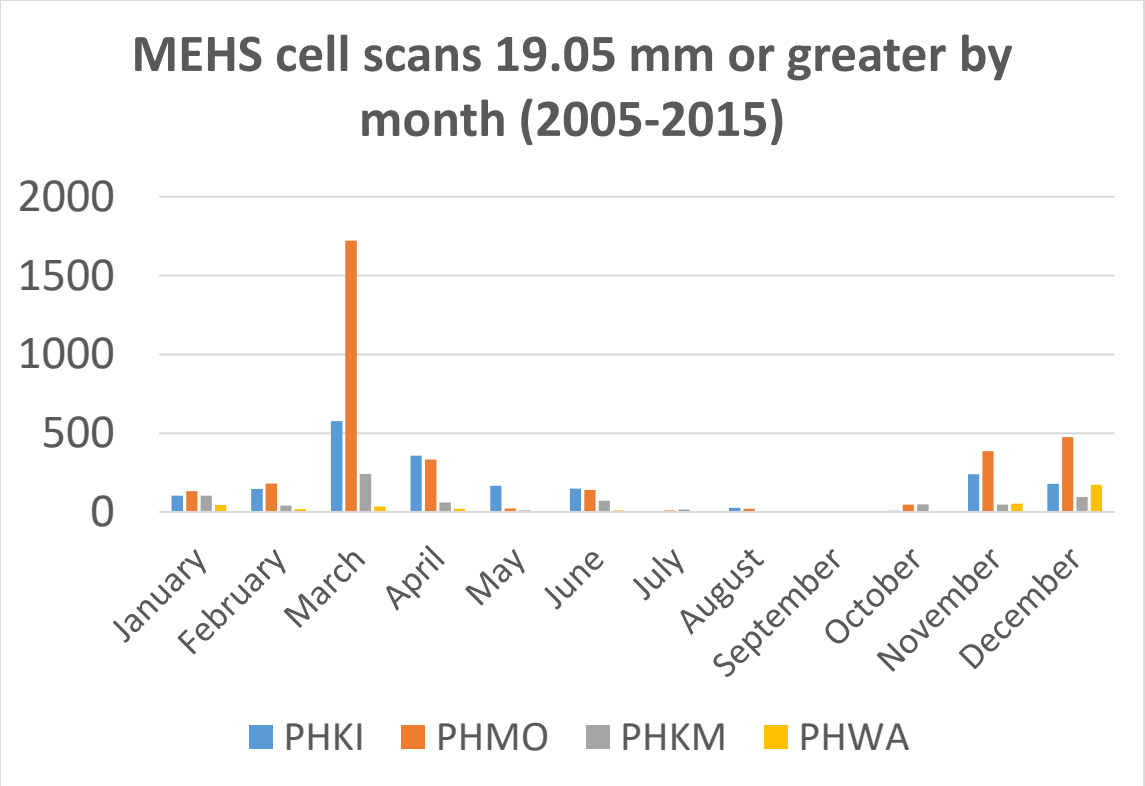

Figure 11. Monthly distribution of MEHS cases ≥ 19 mm.

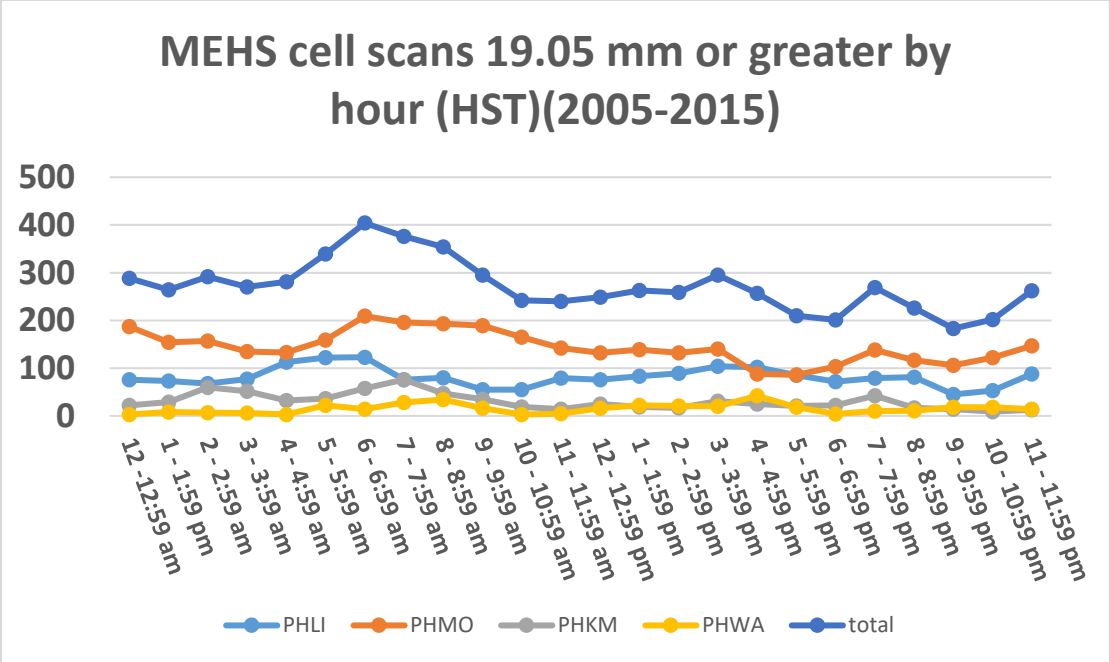

Figure 12. Hourly distributions of MEHS cases ≥ 19 mm from each radar, as well as for the total.

A map of all cell scans of MEHS ≥ 19 mm from 2005-2015 is given in Figure 13. There are several interesting things that show up when plotted in this manner. First, some tracks of individual thunderstorm cells are evident. A number of tracks appear to be oriented from southeast to northwest, particularly to the northeast of O‘ahu, Moloka‘i, and Maui. To the south of the islands, and to the north of O‘ahu, there appears to be a preference for tracks oriented west-southwest to east-northeast. Cell motions cannot be discerned with certainty from this graphic alone, and it is incorrect to assume that a prevailing cell track orientation in a given area is the result of many cells moving the same direction. Further study needs to be done to reveal more about the preferred cell motions in certain areas, as well as the reasons for them.

Figure 13 also reveals areas that appear to be preferred regions for stronger thunderstorms to develop. There are clusters of cases over the eastern half of Kaua‘i, near the east facing or windward shore of O‘ahu, along the northern shore of Moloka‘i, and along the northern and northeastern shore of Maui. This clustering does not appear to be evident on the Big Island, however. It is unknown if this is the result of limited sampling or a meteorological artifact.

Even though the windward facing slopes of the smaller islands appear to be favored, there are fewer cases over interior and leeward sections of all the islands, including over far western Kaua‘i, interior and southwest O‘ahu, and far west Maui. Thus, it seems very likely that different regions of each island may be favored for stronger development in certain background flow regimes (e.g., southeast flow, kona winds, light winds). There also appears to be some indication of clustering near the expected locations of downwind convergence zones (e.g., in a long ribbon extending to the west of the Big Island), although further examination is needed to determine whether that is indeed the cause.

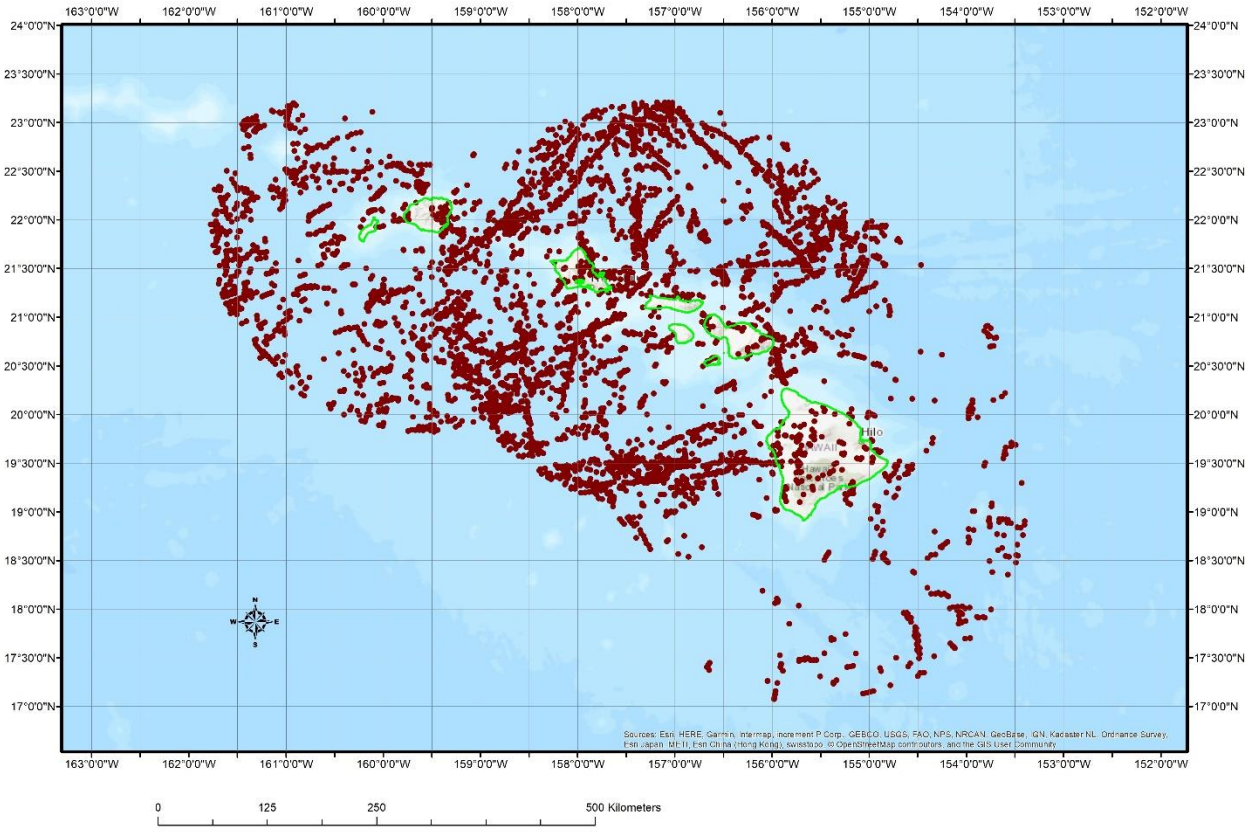

Figure 13. Map of all MEHS detections of ≥ 19 mm (dark dots) for the period 2005-2015.

A plot of all MEHS cell scans of ≥ 44 mm (i.e., golf ball size) is shown in Figure 14. This represents the top 2% of cases. The date associated with each case (or cluster of cases) is shown. Many of the events are single-scan indications, when the cell MEHS peaked at that intensity. There are a number of events, however, where a discrete cell track occurs, the longest of which is approximately 30 km long.

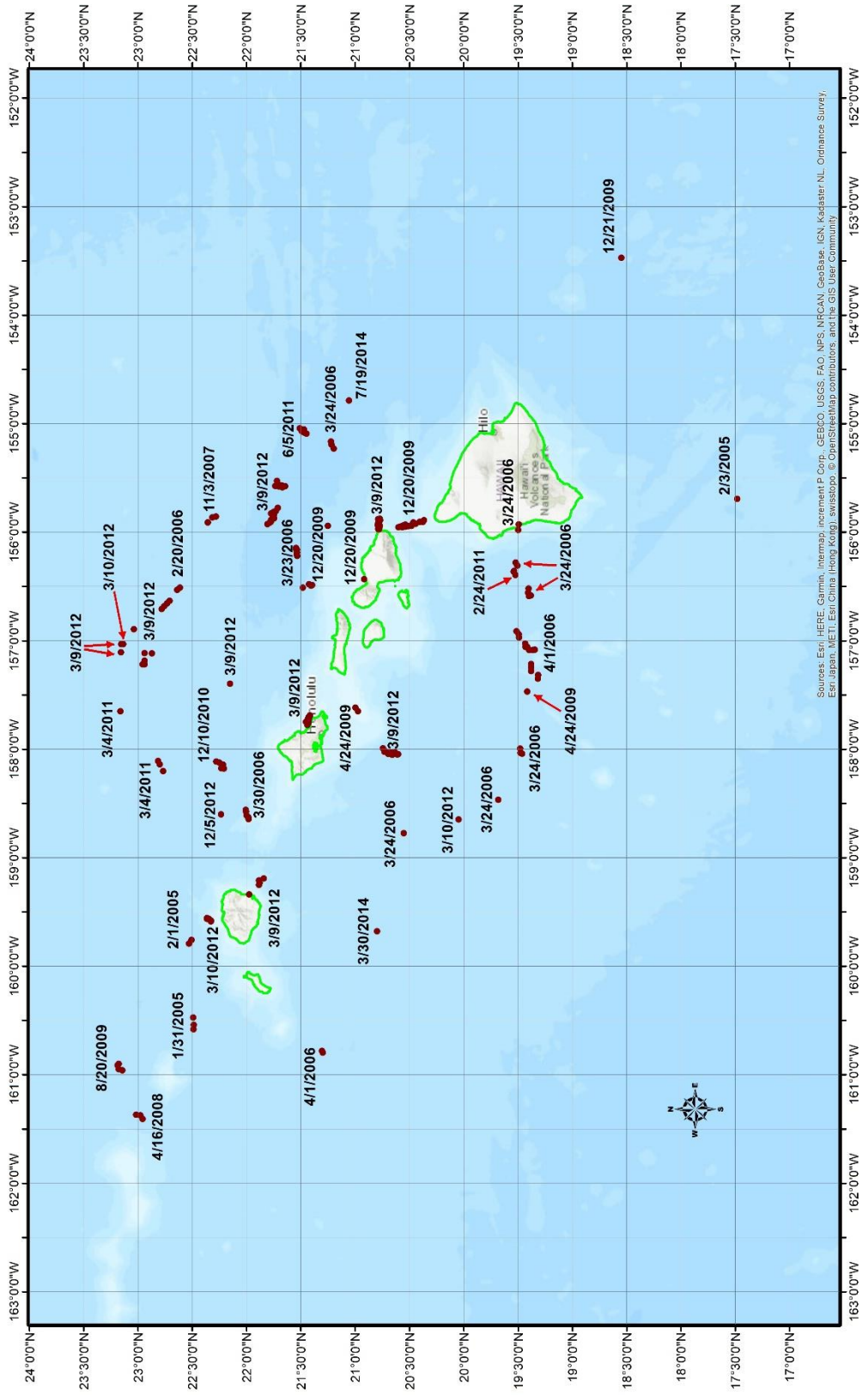

Figure 14. Same as Figure 13, but for MEHS 44 mm. Dates listed (UTC) are the starting date for each occurrence or cluster of occurrences.

3.4 MEHS validation

A simple study was completed to validate MEHS algorithm performance with observed hail reports. The vast majority of the reports were from Local Storm Reports issued by the NWS in Honolulu, while a small number came from NWS shift logs, NCEI Storm Data, and social media. These reports were compared to MEHS algorithm output using a validation time window similar to that used by Witt et al. (1998). The maximum MEHS from 15 minutes prior to the report to 5 minutes after the report from the closest cell within 30 km was compared to the reported hail size. Based on the study by Witt et al., this is to account for several factors, including report error time and location, as well as the time it would be expected to take a hailstone to fall out of the cloud after developing.

A scatterplot of the observed hail size versus the hail algorithm output from all four radars is shown in Figure 15. This includes 44 reports of observed hail, with a total of 81 algorithm detections. MEHS events from areas with significant beam blockage were not included. Although the sample size is limited, there appears to be good correlation between the observed hail sizes and the radar estimates. A linear-fit estimate of observed severe hail in Hawai‘i would correspond to a MEHS of 32 mm. For MEHS cell scans of > 25 mm, as expected, most of the observed reports are smaller than the radar estimates. For cell scans of ≤ 25 mm, there appears to be less of a bias, with a considerable number of observed reports that were larger than the radar estimate. This may be because the hail algorithm was optimized for larger (severe) hail sizes. There are 17 cases where the hail algorithm did not return a MEHS size, yet hail was reported. There are a number of reasons why this might occur, including the distance from radar to storm resulting in incomplete beam volume filling, the lowest elevation angles

intersecting the storm above the freezing level, attenuation due to intervening precipitation, or partial beam blockage.

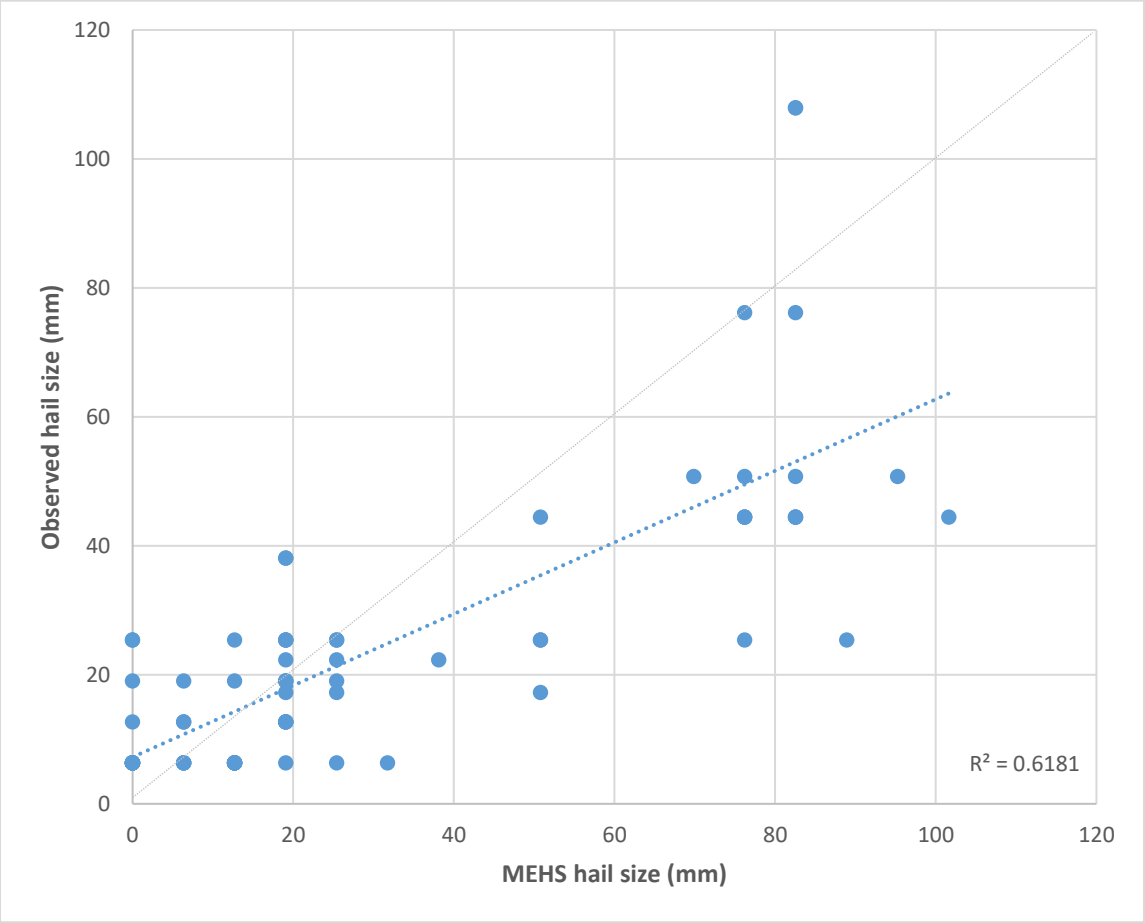

Figure 15. Scatterplot of 44 observed hail reports versus corresponding MEHS detections.

3.5 MEHS sizes versus soundings

From a forecaster perspective, it is helpful to know what parameters are useful for predicting situations likely to lead to large MEHS detections. Here we will examine the same sounding parameters discussed previously, but in terms of MEHS size. Figure 16 shows plots of the 10th, 25th, 50th, 75th, and 90th percentile values for each of the parameters in the antecedent

PHLI sounding for MEHS sizes of 13 mm or less, and for 32 mm and larger. The sounding sample size for the smaller MEHS dataset is 145, and 32 for the larger events. Thus, the results should be interpreted with caution.

The stability parameters of MLCAPE, SBCAPE, MUCAPE, and lifted index do not appear to be useful discriminators. A number of studies (e.g., McCaul and Weisman 1996, Montiverdi and Quadros 1994, Sherburn and Parker 2014) have shown that buoyancy is a relatively minor contributor to observed storm organization, with supercells possible even at relatively low CAPE values. The 500 hPa and 700 hPa geopotential height and temperature fields show weak trends toward lower values with larger MEHS cases. The 500-700 hPa lapse rate, precipitable water, and storm relative helicity values showed little ability to discriminate among sizes. It is somewhat surprising to see that SRH was a poor discriminator, but this seems to show that SRH may be more useful for assessing the potential for low level rotation, rather than deep mesocyclones more likely to produce large hail and other severe weather.

It should not be surprising that of all the parameters given, 0-6 km shear appears to have the clearest signal, with higher values for larger MEHS. As several prior studies have shown (e.g. Weisman and Klemp 1984, McCaul and Weisman 2001), the non-hydrostatic pressure perturbations induced by interactions between the updraft and the environmental winds can result in significant contributions to vertical acceleration, more than to be expected from buoyancy alone. The data here suggests that in some cases, Hawai‘i may experience environments similar to those described in Sherburn and Parker (2014), which are commonly found during severe weather events in the southeast CONUS during the cool season. While the events with the larger MEHS sizes appear to be nearly always associated with 0-6 km shear in excess of 16 m s^{-1}, one can see that large 0-6 km shear alone does not necessarily result in large MEHS. Again, this is

consistent with Rasmussen and Blanchard (1998), who note that for even relatively strong discriminators of ordinary, supercell, and tornadic storms, there is a rather high false alarm rate. They attribute several reasons as to the possibility for why this occurs. To summarize these reasons, convective mode is not only dependent on environmental conditions given by soundings. For example, strong synoptic forcing within an environment favorable for supercells might instead favor storms with squall line/QLCS characteristics rather than supercells. They also note that while the environmental conditions might generally favor supercells, that perhaps there are other mesoscale factors, such as enhancement of helicity along a boundary or baroclinic and/or moisture gradients, are needed to sustain supercell structures. They also note that inadequate reporting might result in an underrepresentation of more intense cases. This should have a relatively minor effect on this climatology since we are using radar rather than public reports.

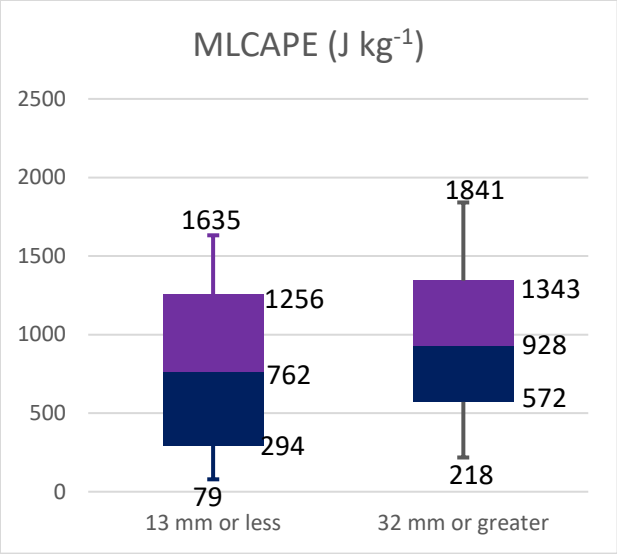
MLCAPE (J kg-1)
2500
2000
1500
1000
500
0
1635
1256
762
294
79
1841
1343
928
572
218
13 mm or less
32 mm or greater

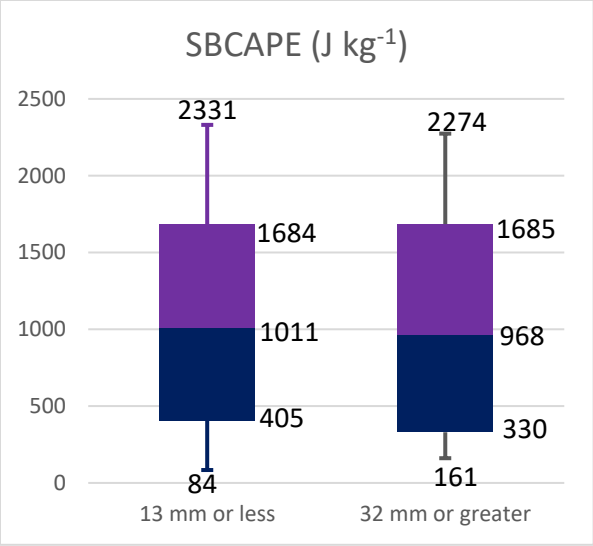
SBCAPE (J kg-1)
2500
2000
1500
1000
500
0
2331
1684
1011
405
84
2274
1685
968
330
161
13 mm or less
32 mm or greater

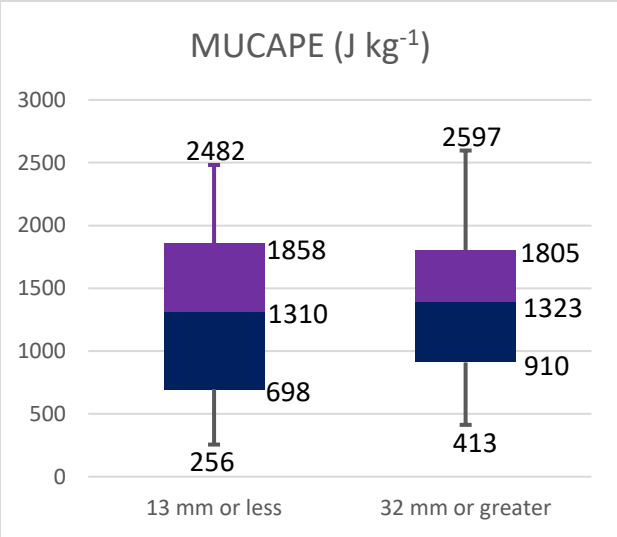
MUCAPE (J kg-1)
3000
2500
2000
1500
1000
500
0
2482
1858
1310
698
256
2597
1805
1323
910
413
13 mm or less
32 mm or greater

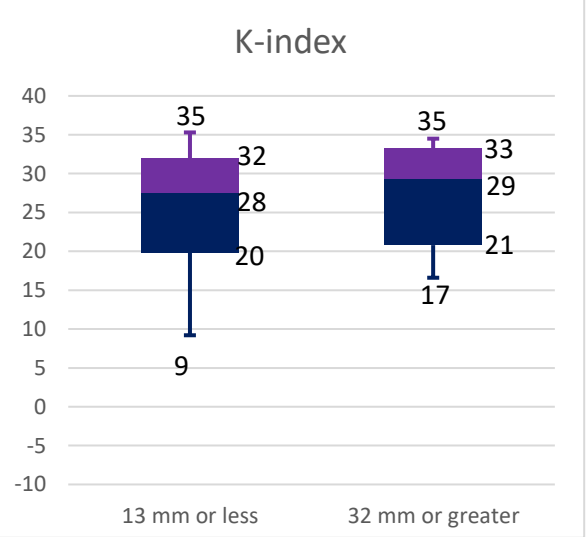
K-index
40
35
30
25
20
15
10
5
0
-5
-10
35
32
28
20
9
35
33
29
21
17
13 mm or less
32 mm or greater

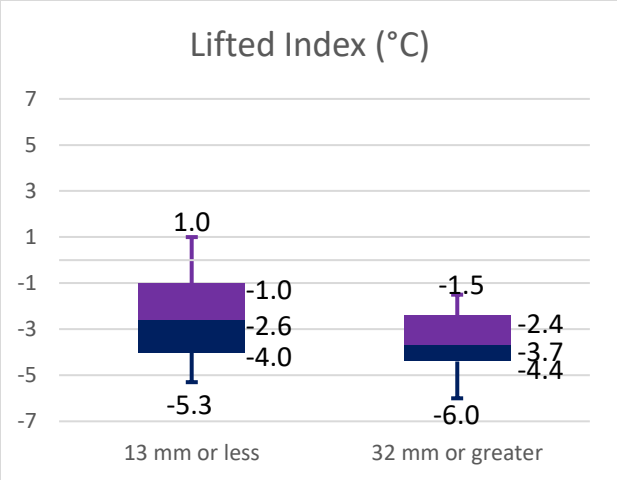
Lifted Index (°C)
7
5
3
1
-1
-3
-5
-7
1.0
-1.0
-2.6
-4.0
-5.3
-1.5
-2.4
-3.7
-4.4
-6.0
13 mm or less
32 mm or greater

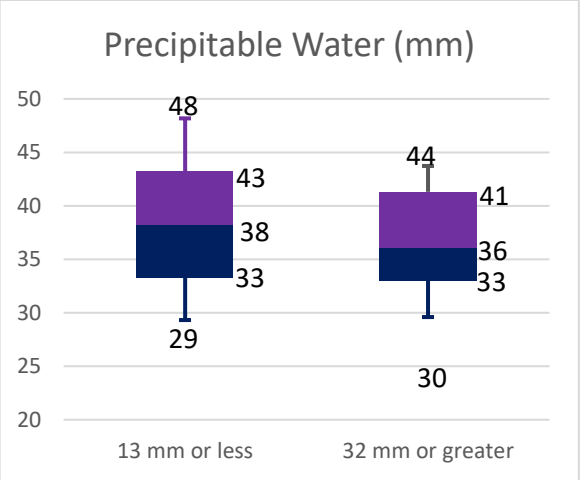
Precipitable Water (mm)
50
45
40
35
30
25
20
48
43
38
33
29
44
41
36
33
30
13 mm or less
32 mm or greater

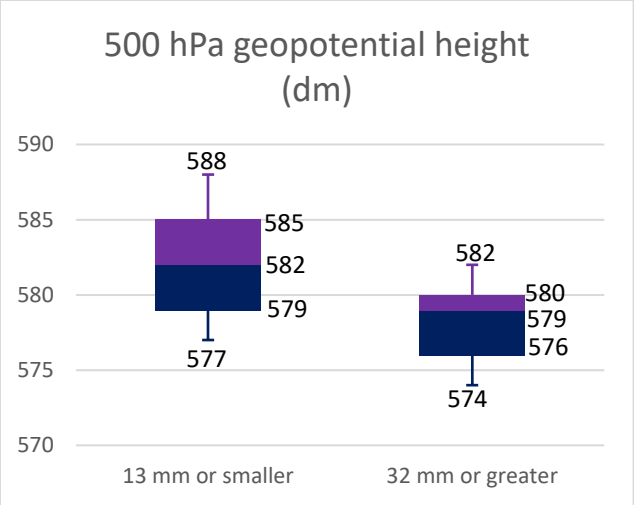
500 hPa geopotential height (dm)
590
585
580
575
570
588
585
582
579
577
582
580
579
576
574
13 mm or smaller
32 mm or greater

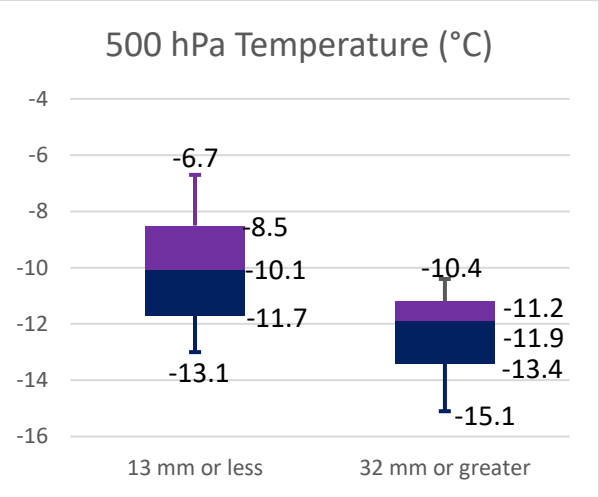
500 hPa Temperature (°C)
-4
-6
-8
-10
-12
-14
-16
-6.7
-8.5
-10.1
-11.7
-13.1
-10.4
-11.2
-11.9
-13.4
-15.1
13 mm or less
32 mm or greater

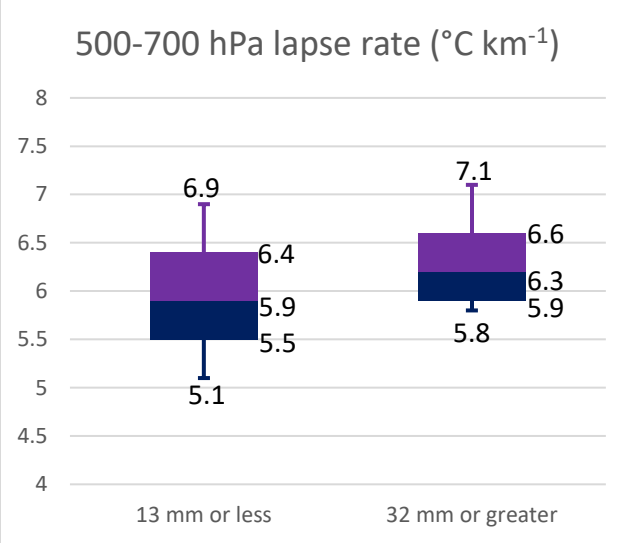
500-700 hPa lapse rate (°C km-1)
8
7.5
7
6.5
6
5.5
5
4.5
4
6.9
6.4
5.9
5.5
5.1
7.1
6.6
6.3
5.9
5.8
13 mm or less
32 mm or greater

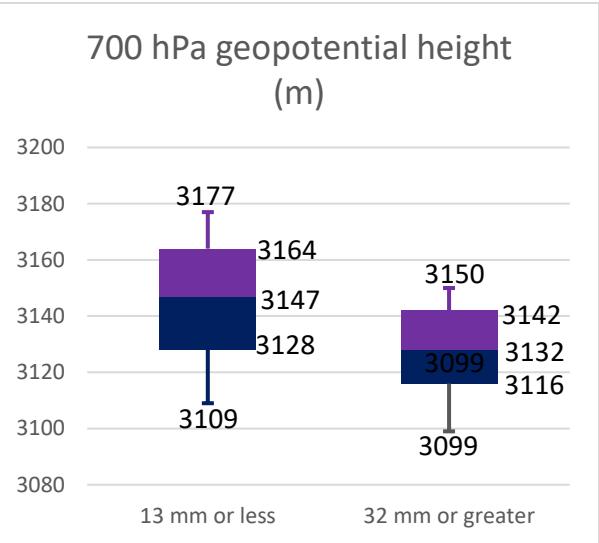
700 hPa geopotential height (m)
3200
3180
3160
3140
3120
3100
3080
3177
3164
3147
3128
3109
3150
3142
3132
3116
3099
13 mm or less
32 mm or greater

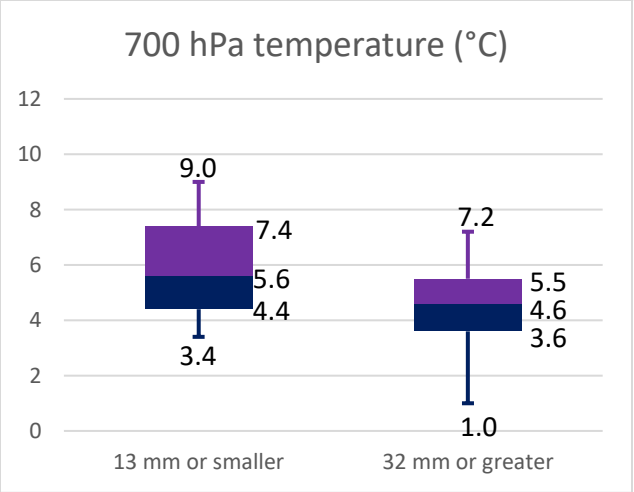
700 hPa temperature (°C)
12
10
8
6
4
2
0
9.0
7.4
5.6
4.4
3.4
7.2
5.5
4.6
3.6
1.0
13 mm or smaller
32 mm or greater

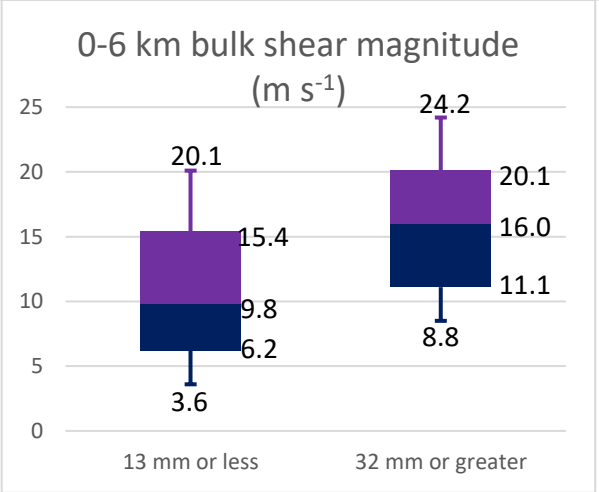
0-6 km bulk shear magnitude (m s-1)
25
20
15
10
5
0
20.1
15.4
9.8
6.2
3.6
24.2
20.1
16.0
11.1
8.8
13 mm or less
32 mm or greater

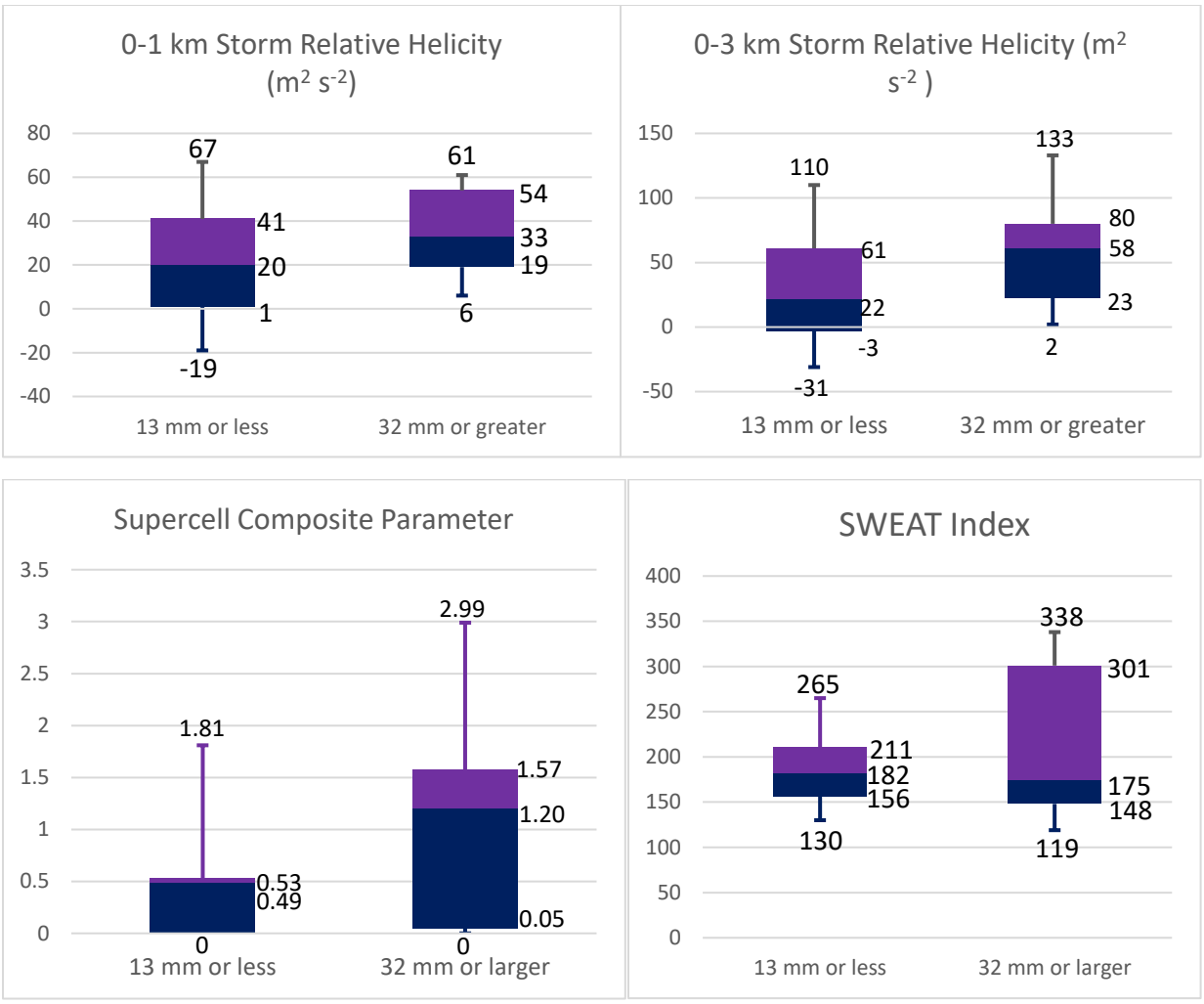

Figure 16. As in Figure 5, but for MEHS sizes of 13 mm or less (left side of each diagram), and 32 mm and larger (right side of each diagram) within PHKI radar range. The boxes indicate the extent of the 75th, mean, and 25th percentiles. Whiskers indicate the extent of the 90th and 10th percentiles.

3.6 Cell-based MEHS results

An individual thunderstorm cell detected by radar is likely to be scanned a number of times during its lifetime. Depending on the how persistent the cell is, where it is located, and to a lesser extent on the scan strategy in use at the time, there may be a large number of MEHS detections for any individual thunderstorm. In many cases, there can also be MEHS detections from multiple radars for an individual cell. Up to now, I have developed results based on *any* indication or exceedance, since a forecaster may very well need to take action with even a single occurrence. However, there may also be a desire to understand the radar-based climatology of thunderstorm *cells* that meet or exceed these thresholds at any time during their radar-detectable life. In order to obtain this cell-based information, further examination had to be done and additional factors had to be considered. For this portion of the study, all radar scans with MEHS values of 19 mm or larger were visually examined to make a subjective determination of continuity over time as a cell.

The WSR-88D cell tracking algorithm, which assigns an alphanumeric ID to each cell, was helpful in this regard, but it is not foolproof. Cells with MEHS greater than 19 mm detected by multiple radars (not necessarily simultaneously) were bundled together considered as a single storm case. In some cases, one cell would weaken as another cell develops nearby. In this case, the radar algorithm might incorrectly identify the "new" cell with the previous nearby cell ID (making the cell appear to "jump" slightly in position). When this appeared to occur, I counted this as a new storm (assuming this new storm also had a MEHS greater than 19 mm at some point in its life cycle). Although relatively unusual, similar situations also occur with merging and splitting cells. After cell-mergers and cell-splits, a determination was made to attempt to determine which storm was dominant. If a determination could be made, I would continue to

maintain its original cell ID, and end or begin the non-dominant storm, respectively. Otherwise, I utilized the new IDs afterward.

For the 6521 indications of MEHS over 19 mm from the four radars, 1333 cells were identified. A breakdown of the maximum MEHS size by storm is given in Table 7. This is also broken down as a probability distribution function in Figure 17. No attempt was made to establish a cell count for MEHS less than 19.1, as the sheer number and disorganization of thousands of weaker cells makes categorization impractical.

Table 7. The number of cells with a given maximum MEHS during their radar-detectable lifetime.

Maximum MEHS (mm)	Number of cells (2005-2015)
19.1	940
25.4	222
31.8	89
38.1	34
44.5	17
50.8	9
57.2	5
63.5	4
69.9	2
76.2	2
82.6	1
88.9	1
95.3	1
101.6	4

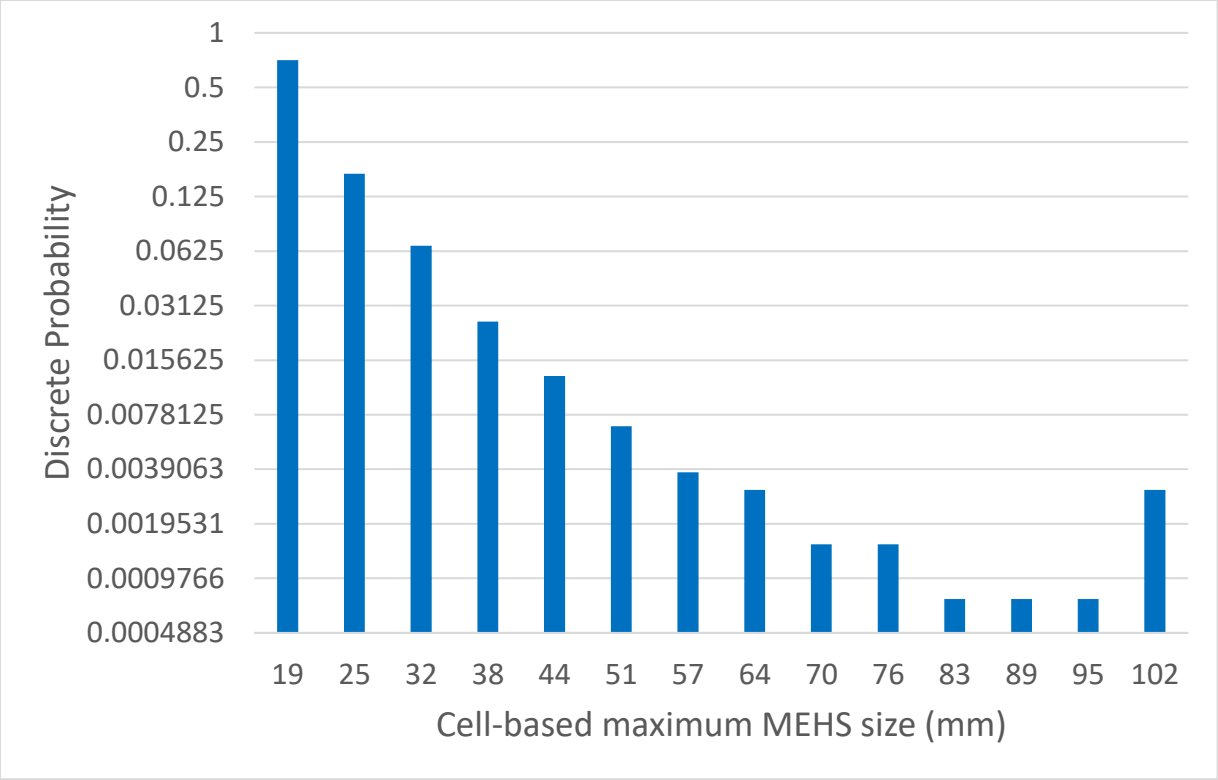

Figure 17. Discrete probability of storm cells ranked by maximum MEHS size (mm)(2005-2015) during their radar-detectable lifetime.

The number of storms (for MEHS equal to or greater than 19.1 mm), utilizing cell initiation time) by month is given in Figure 18. The relative breakdown here is nearly identical to the results of Figure 7, with the breakdown reflecting an overall maximum during the wet season months, and peaks in November, December, and March.

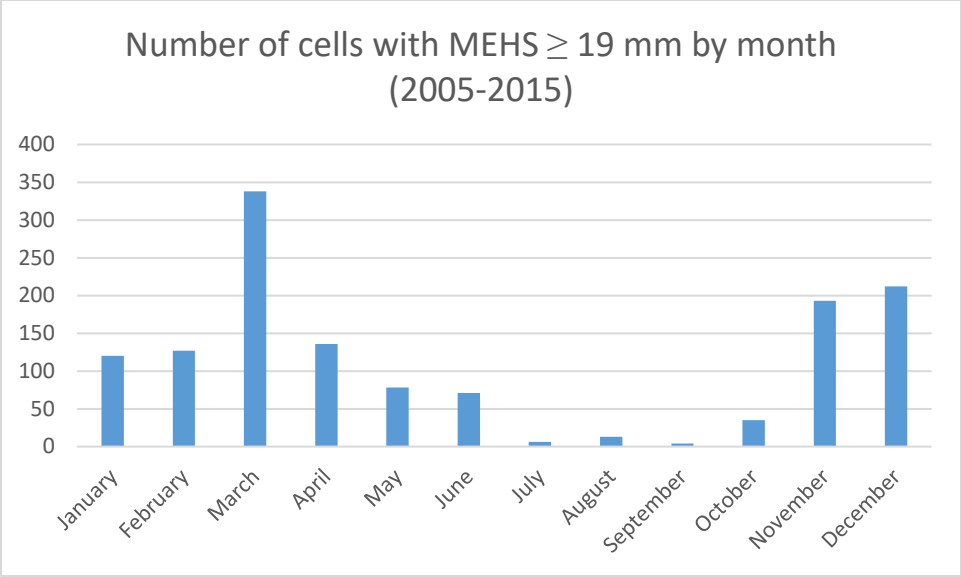

Figure 18. Number of storms (using cell-based considerations) by month (2005-2015).

3.7 TVS Climatology

For the final part of the study, I used radar-indicated TVSs to investigate the stronger rotational signatures more likely to lead to tornadoes or larger waterspouts. However, as previously noted, the sample size is quite limited. During the period from August 2004 to December 2016, the SWDI database contained 637 TVSs from the four radars. However, an examination of all TVS-detected cells revealed 552 of these (87%) were determined to be from poor data, typically from corrupted velocity data in and near terrain features. Of the original 637 TVSs, 85 (13%) appeared to be legitimate features associated with convection and not corrupted by terrain. These occurred on 26 calendar days. The locations and dates of these are shown on the map in Figure 19. Only three confirmed TVSs (3.6%) occurred over land: one over O‘ahu, one over Maui, and one over the Big Island. None of these were associated with any reported damage (Storm Data 2011, Storm Data 2015). The TVSs over O‘ahu and Maui were transient

and associated with a weak squall line moving across the islands. The TVS over the Big Island appeared to be associated with enhanced afternoon convection that developed over the slopes of Mauna Loa.

As mentioned earlier, not all tornadoes are simultaneously accompanied by a TVS. In addition to the Kapolei tornadoes in 2009, there are a few other noteworthy examples: Although a damaging tornado was associated with a persistent TVS just southwest of Lānaʻi in March of 2006, the TVS dissipated before the tornado reached the shoreline. Another tornado, which made landfall on southern Kauaʻi in 2008, did not trigger the TVS algorithm. There was strong rotation, but due to its proximity to the radar, the circulation did not have the gate-to-gate velocity difference that is required for the TVS algorithm (Mitchell et al. 1998).

On March 9, 2012, a supercell thunderstorm with a tornado occurred in Kailua, on Oʻahu. Although the radar algorithm returned a TVS with this cell for 7 volume scans, a careful examination of the velocity data revealed that the algorithm appeared to be triggered by spurious velocity features over the southern portion of the Koʻolau range, rather than rotation associated with the attendant supercell. However, it seems likely that poor velocity data from terrain may have masked a true rotational feature within this storm.

Figure 19 includes a number of areas where a single cell exhibited a TVS rotation for multiple (not necessarily consecutive) volume scans. This implies more persistent rotation and is more likely to be from a supercell thunderstorm, rather than a brief spin up. Out of the 85 TVSs in the database, 50 of them (59%) were associated with the same cell on multiple volume scans. The most persistent TVS occurred southeast of Kauaʻi, from the PHKI radar, on February 21, 2006. The TVS occurred intermittently from 12:09 pm local time, to 2:45 pm local time over a

path approximately 40 km long, and originated from a thunderstorm with supercell characteristics in the base radar data.

The monthly distribution of TVSs from the Hawai‘i radars (2005-2016) is shown in Figure 20. Just as with MEHS events, there is a strong tendency for TVSs to favor cool season months, with relative maxima in December and March. For the 12-year period, there was only one legitimate TVS during the months of April through October. This agrees well with previous authors who found that funnel clouds, waterspouts, and tornadoes were observed most often during the cool season, during breaks in the normal trade wind pattern around Hawai‘i.

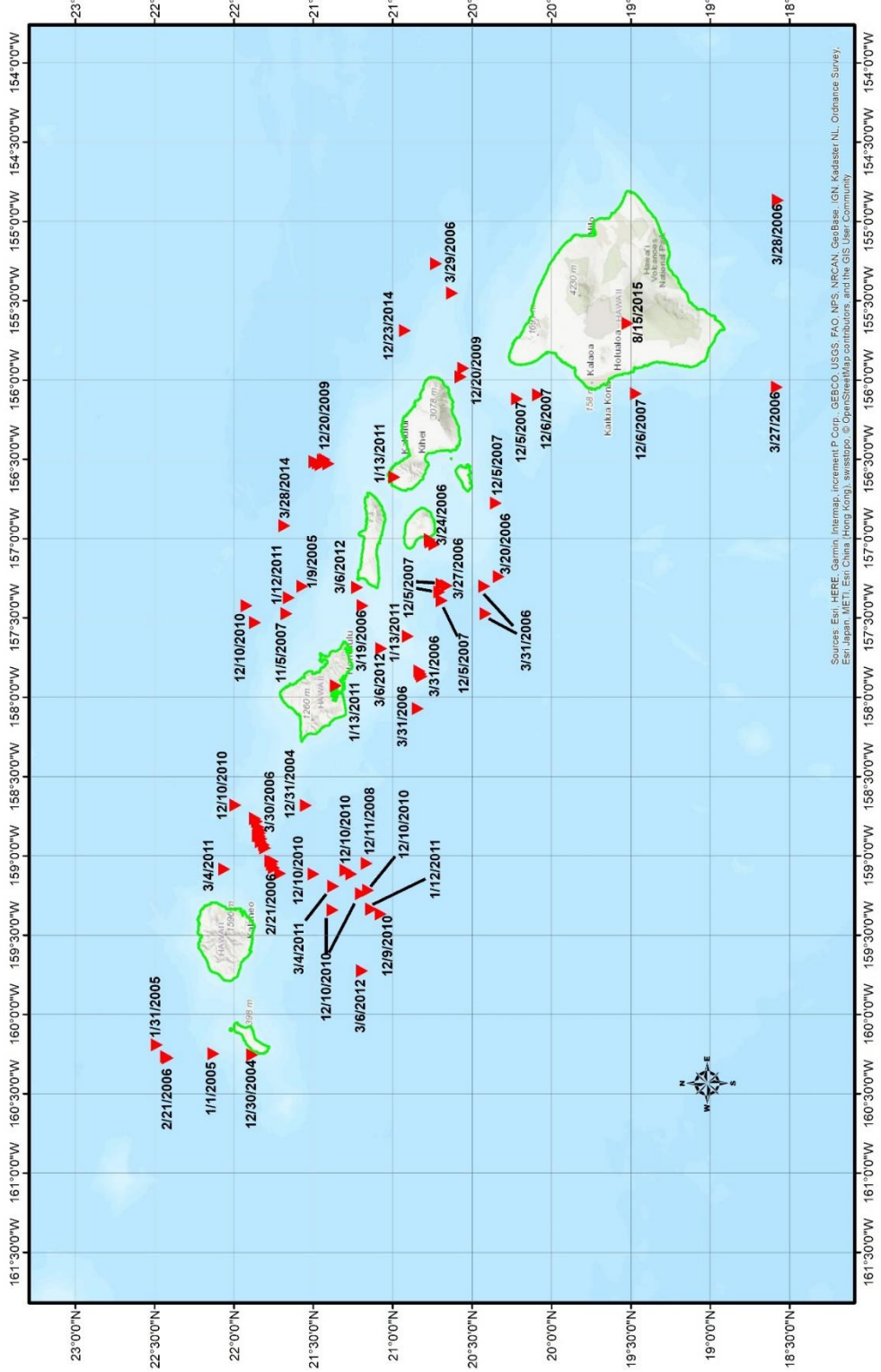

Figure 19. Plot of all TVS (Aug. 2004 – Dec. 2015), red triangles. Date (UTC) is given associated with TVS events or cluster of TVSs.

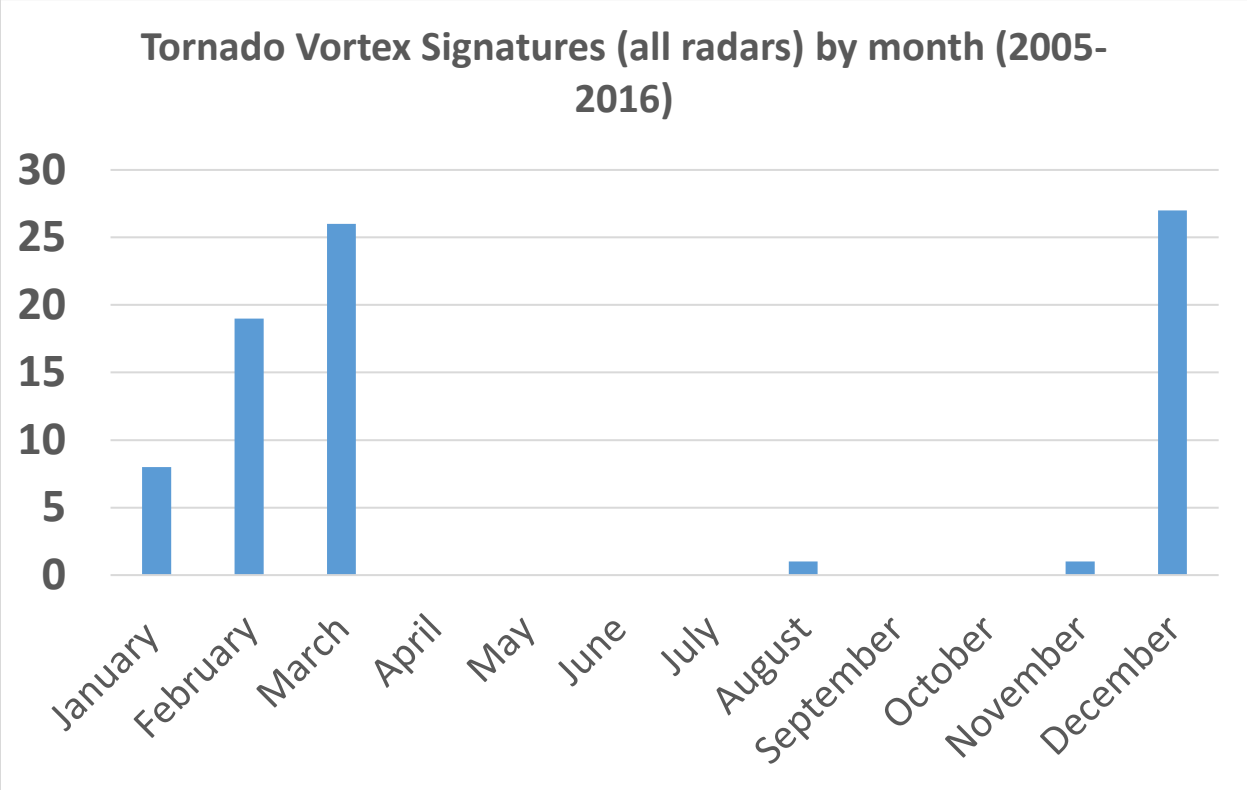

Figure 20. Monthly distribution of TVSs (2005-2016).

Figure 21 shows the hourly distribution of TVSs from all four radars for the period August 2004-December 2016. While previous studies showed a distinct decrease in the number of observed funnel events at night, the hourly frequency of TVSs from radar does not appear to show any strong trends. This is also in stark contrast to the nighttime preference of MEHS events. Three-fourths of the total number of TVSs from 2-3 pm local time is from the aforementioned persistent TVS on February 21, 2006, and just under half the total number of TVSs from 11 am until 2 pm is accounted for by February 21, 2006.

The WSR-88D TVS detection algorithm calculates parameters to rank TVS strength. Two of these are the low-level delta-V and the maximum delta-V (hereafter, LLDV and MXDV,

respectively). The LLDV is the maximum radial velocity difference at the same range gate on adjacent radials at the lowest angle of the TVS detection (typically 0.5°)(Kingfield and LaDue 2015), sometimes referred to as "gate-to-gate" rotation. The MXDV is the maximum radial velocity difference at any angle within the 3-dimensional TVS detection. Although not calculated by the TVS algorithm, another commonly used rotational metric for tornadic storms is low-level radar-derived rotational velocity (V_{rot}). This is defined as half of the absolute value of the maximum inbound and outbound velocities within a mesocyclone. The maxima do not necessarily need to be gate-to-gate. However when they are, the LLDV value is simply $V_{rot} \times 2$.

A number of authors (e.g., Smith et al. 2012, Kingfield and Ladue 2015, Gibbs 2016) have been able to establish relationships between these measures of rotation based on WSR-88D velocity fields, and the intensity of surveyed tornado damage. The results were stratified by range, in order to mitigate the effects of larger sampling volumes masking more extreme velocity values. They also considered storm characteristics and organization (e.g., supercell vs. QLCS). They discovered that when the lowest level V_{rot} exceeded about 20 m s^{-1}, the chance of strong tornadoes (EF2 or greater intensity) began to increase.

Use of the WSR-88D algorithms, however, is not ideal for determining tornado threat. Although it would be preferable to utilize a manual determination of V_{rot} to make a strict comparison to some of the findings in these studies, the Level 3 velocity data available for this study does not always include the absolute maximum and minimum velocities. Prior to 2010, the velocity data was binned into relatively large ranges that make it impossible to obtain a reliable V_{rot} value. However, the LLDV and MXDV values utilize the original radar data before data recombination. (Note that V_{rot} will always be $\geq$ LLDV/2). A count of LLDV and MXDV values for all four radars is given in Figure 22. Not surprisingly, when compared to the potential tornado

intensity of previous studies, most of the detected TVSs are weak. However, a significant number (about 12%) of the TVSs would fall into the zone with some potential for EF2 or higher damage, based on the NWS Warning Decision Training Branch guidance shown in Gibbs (2016).

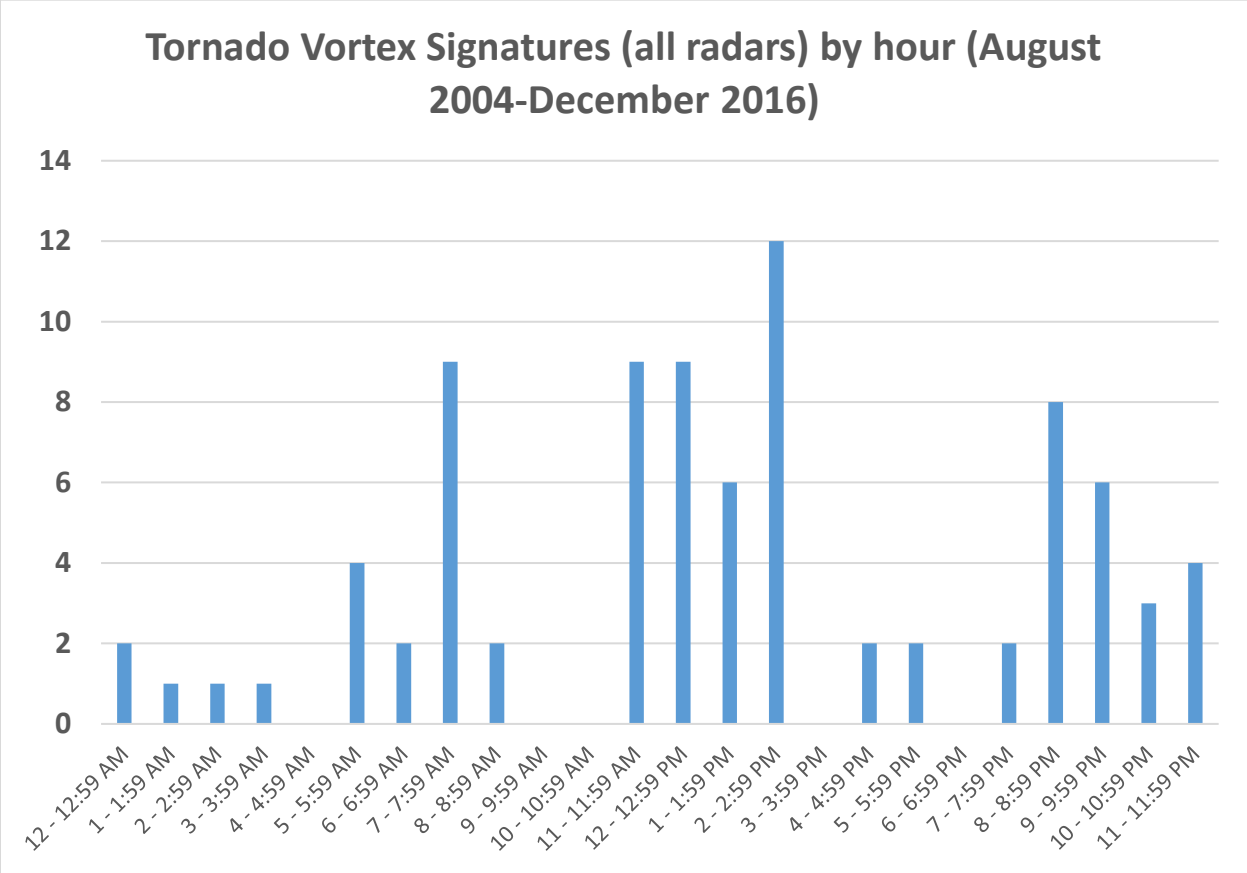

Figure 21. Hourly distribution of TVSs (August 2004-December 2016).

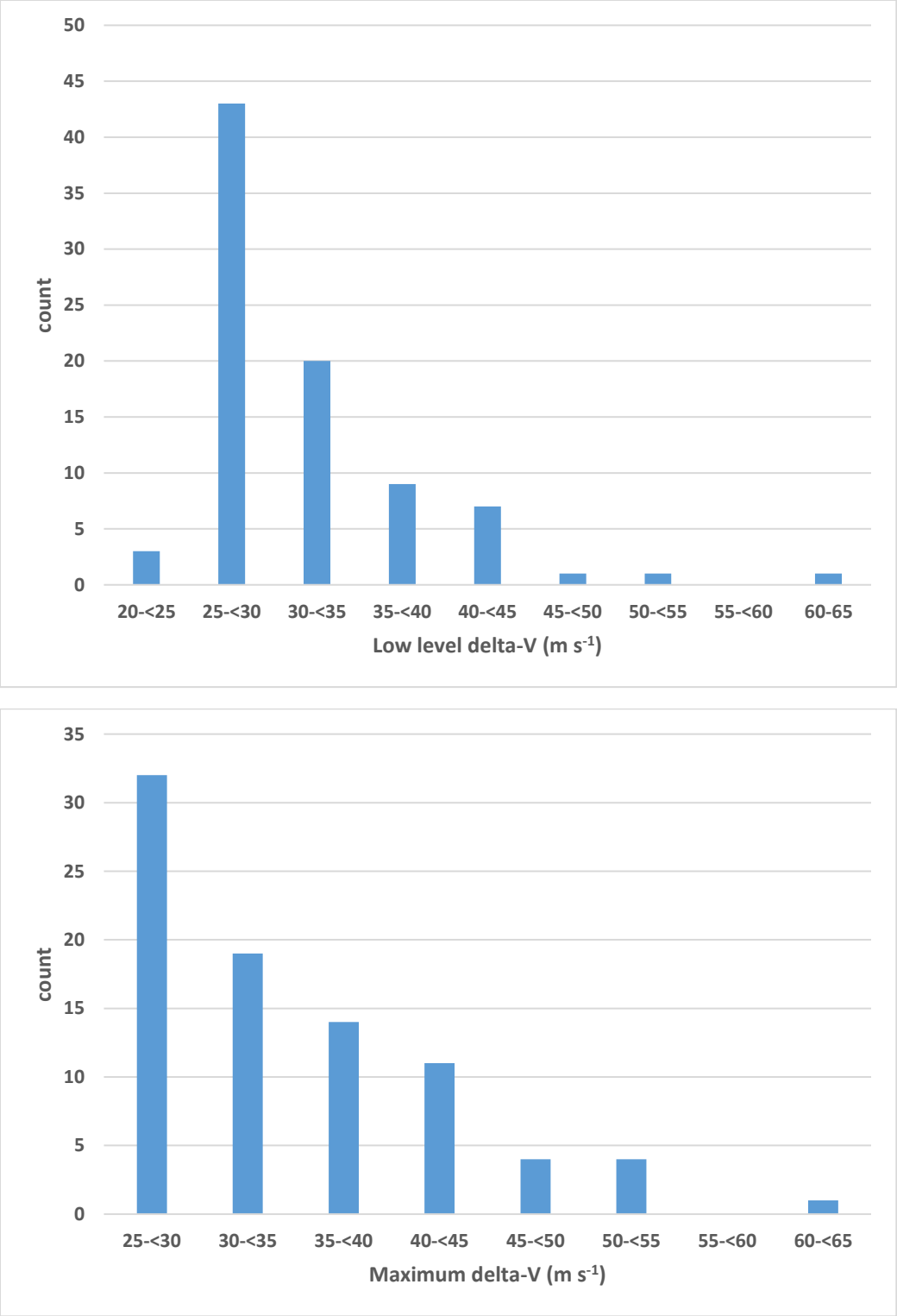

Figure 22. Count of low level delta V (top) and maximum delta V (bottom) for all TVSs (Dec. 2004- Dec. 2015).

3.8 Sounding parameters associated with TVSs on the Kauaʻi radar.

Similar to the sounding comparisons for observed thunderstorms at Līhuʻe, MEHS events, and MEHS sizes, I examined sounding parameters associated with TVSs detected by radar. There are again some significant considerations that must be made in regard to the sampled environment. The conditions favorable for TVS development are almost certainly even more sensitive to the ambient conditions than thunderstorms or MEHS events, with even fewer samples to utilize. Boundary passages and existing convection affecting the sounding can result in drastic differences in wind fields, causing a poor evaluation of the parameters considered to be important for tornado genesis (e.g., storm relative helicity). For this portion of the study, rather than always using the antecedent sounding as in prior comparisons, I used WSR-88D velocity imagery, VAD wind profiles, surface observations, and temporally adjacent soundings to establish whether or not to use the temporally closest sounding, or the antecedent sounding, for the most representative data. This led to the adjustment of sounding choices associated with two TVS events, 0619-0649 UTC 10 December 2010, and 0748-0758 UTC 4 March 2011, to utilize the antecedent soundings instead of the sounding closest to the time of the TVSs.

When looking at only TVSs detected by the PHKI radar (for their proximity to the Līhuʻe sounding site), there are 12 soundings which correspond to 40 individual TVSs. Each TVS is assigned a sounding in order to give more weight to situations where there are more TVSs (i.e., the TVSs are more numerous among cells, or more persistent with a single cell). Some consideration and preliminary work was given to similar cases from the PHMO radar when compared to the PHLI sounding, but the distance from many of the TVS to the sounding site, and particular synoptic and mesoscale situation for any given setup makes it difficult to obtain what appear to be useful data.

The average and median values of the parameters from the 40 TVSs are depicted in Table 8. When comparing the median values in Table 3 to the median values in Table 8, it is apparent that parameters related to instability (CAPE, K-Index, Lifted Index) and moisture (Precipitable Water) appear to be similar to, or in some cases, even less stringent than those for observed thunder and MEHS events. The median MLCAPE value is lower than that found by Rasmussen and Blanchard (1998) for significant tornadoes (i.e., tornadoes rated F-2 or greater). However, the 500 hPa and 700 hPa median geopotential height values are somewhat lower for TVS events than for thunder and MEHS events. The temperatures at these levels are similar to those for TVS, thunder, and MEHS events.

The largest differences among the parameters between thunder, MEHS events, and TVS cases are in the severe weather indices, storm relative helicity, and 0-6 km shear. The mean sounding parameters for these are higher for TVS events than for observed thunder cases. The median SWEAT index of around 200 for observed thunder compares to around 300 for Hawai‘i TVSs, which is lower than Miller’s (1972) low-end threshold value of 400 for tornado cases (Miller defined a tornado case as 5 or more tornadoes within the same general area). The 0-1 km storm relative helicity for Hawai‘i TVS events is roughly double that for observed thunder and MEHS cases. The 0-3 km SRH is over 5 times larger for Hawai‘i TVS cases than for observed thunder, but nearly identical to the median value obtained by Rasmussen and Blanchard (1998) for significant tornadoes over the CONUS. The median 0-6 km shear is about 4 to 5 m s^{-1} higher in TVS cases.

These findings seem consistent with Schroeder (1977) who suggested there may occasionally be value in utilizing tornado forecast parameters to assess tornado threat in Hawai‘i, when they are driven by synoptic scale forcing. Tanabe (2000) showed little skill in using classic

forecast parameters to forecast weaker (i.e., non-mesocyclonic) tornadoes and waterspouts in Hawai‘i. Additional work needs to be done to examine the synoptic situations commonly associated with these TVS (as well as the larger MEHS cases), in order to put these parameters into a proper forecast context.

Table 8. PHLI sounding parameters associated with 40 TVS detections from PHKI. All sounding parameters reflect closest temporal sounding parameters except for 10 December 2010 (00z used instead of 12z) and 4 March 2011 (00z used instead of 12z).

Parameter	minimum	median	average	maximum
MLCAPE (J kg^{-1})	1	597	760	2312
SBCAPE (J kg^{-1})	3	826	991	2882
MUCAPE (J kg^{-1})	20	826	1090	2882
K-Index	26.3	30.1	31.3	37.8
Lifted Index (°C)	-6.6	-2.3	-2.8	2.9
Precipitable Water (mm)	33.1	42.7	41.7	52.4
500 hPa geopotential height (m)	5730	5780	5771	5800
500 hPa temperature (°C)	-13.3	-10.1	-10.6	-7.5
500-700 hPa lapse rate (°C km^{-1})	4.8	5.9	5.9	6.5
700 hPa geopotential height (m)	3054	3110	3104	3127
700 hPa temperature (°C)	3.4	5.5	5.0	7.2
SWEAT index	194.6	300.7	307.8	461.7
0-6 km bulk shear magnitude (m s^{-1})	10.8	15.2	15.1	37.6
0-1 km storm relative helicity (m^2 s^{-2})	10	57	62	135
0-3 km storm relative helicity (m^2 s^{-2})	67	183	161	264
Supercell composite parameter	0.1	1.6	2.5	8.1

Chapter 4. Summary, Conclusions, and Future Work

This work presents new information on thunderstorms and severe weather in Hawai‘i, using sounding based parameters and radar-based proxies to improve the climatology. Radar data overcomes some of the challenges of previous studies, including population and diurnal visibility biases, and extends the range of reportable area well beyond the land. However, other challenges and assumptions must be considered when evaluating the results. Although the radar algorithm was designed to correlate to storm intensity, confidence is rather low in precisely how severe weather will manifest itself at the surface based on a given signature, due to rather small sample sizes in Hawai‘i. There are also areas where the radar is inadequately sampling due to beam blockage. Despite these limitations, these findings should help to give forecasters a better idea of not only how often more intense events occur, but also where and when they tend to occur. I also paired these events with sounding data, so forecasters will become more comfortable with recognizing climatologically unusual or dangerous values, and how some parameters compare with typical mainland values during severe weather events.

The sounding data associated with thunderstorm cases indicated that, generally more instability is optimal for thunderstorms in Hawai‘i than on the mainland. The median MLCAPE value for observed thunderstorms at Līhu‘e is nearly double that found by Rasmussen and Blanchard for mainland cases of “ordinary thunderstorms,” with a value of nearly 1200 J kg^{-1}. This is probably due to the typically weak synoptic forcing environments in Hawai‘i. In addition, relatively weak mid-level (500-700 hPa) lapse rates (median 6.1°C km^{-1}) are typical for thunderstorm situations at Līhu‘e, with lapse rates >6.8°C km^{-1} quite rare. Typical thunderstorm cases also feature an abundance of moisture, with K-indices in the upper 20s to mid 30s, and

total precipitable water values approaching or exceeding 40 mm. The sounding parameter values associated with MEHS cases of 6 mm or greater within 30 km to Līhuʻe were generally very close to those found from observed thunder cases at Līhuʻe.

MEHS events from 2005-2015 strongly favored the months of November through May, which encompasses most of the typical wet season in Hawaiʻi. Activity on the Kauaʻi and Molokaʻi radars increases earlier in the wet season, but peaks in March. On the Big Island radars, the MEHS events start later, but peak in December. Very few MEHS events have occurred during the months of July, August, and September.

The Kauaʻi and Molokaʻi radars show a distinct diurnal trend with a relative minimum in MEHS event activity during the midday hours, and a peak near local midnight. A minor peak also occurs during the mid-afternoon, which is likely due to afternoon convective patterns over the islands themselves. The Big Island radars experience less of a diurnal change overall, with only minor overnight and afternoon peaks witnessed from the North Kohala radar.

A gridded plan view mosaic of average annual MEHS events indicates convective maxima located downwind from each island, in the area that often experiences low-level convergence in easterly or southeasterly flow. There are also weak maxima in activity over the interior of the islands, possibly due to afternoon convection in light wind patterns.

MEHS values of >13 mm comprise less than 5% of the total number of events during the study period, and values >32 mm are slightly less than 1%, observed on 5.5 days per year on average. The data show an average of 1.5 days per year with MEHS values of ≥ 51 mm, which past studies have shown to be typically associated with supercells. Larger MEHS events also strongly favor wet season months, with a peak in November and December, and another in

March and April. They show less of a dependence on the overnight hours, with little diurnal signal seen in the hourly totals. On land, the event density appears to slightly favor the eastern portions of Kauaʻi, Oʻahu, and Maui, though some cases do occur over interior and leeward sections. Although the sample size is small, the MEHS algorithm tends to overestimate the hail sizes of larger events, which may be due in part to the bias built into the design of the algorithm.

For stronger events, typical stability parameters such as those related to CAPE and lifted index do not appear to show significant increases over weaker events. Many of the other parameters exhibited little difference across the size spectrum. Larger MEHS events were often associated with colder temperatures and lower geopotential heights at 700 and 500 hPa. The 0-6 km shear was almost always in excess of 16 m s^{-1} for stronger events, but it should be noted that this is only an indication of potential, since the environmental conditions assumed by soundings are not the only factors necessary for thunderstorm organization.

The sample size for TVS cases is small (a total of 85). Only 3 TVS cases occurred over land, although one persistent TVS occurred just before a tornado hit the island of Lānaʻi. Fifty-nine percent of the TVSs occurred with the same cell on multiple scans. One persistent cell exhibited a TVS intermittently for well over two hours over a 35 km long path. TVS signatures, like MEHS events, favor the wet season, with a peak in December, a relative minimum in January, and an increase in February leading to another peak in March. Only 1 TVS occurred between the months of April and October. Much like with the stronger MEHS events, there appears to be little diurnal preference in the hourly TVS totals. Most TVSs are associated with delta-V values of <30 m s^{-1}, but values ≥ 45 m s^{-1} do occur on occasion. Well-known severe weather parameters in the continental United States, such as the SWEAT index, the Supercell

Composite Parameter, 0-6 km shear, and low level storm relative helicity values sometimes approach those known to be associated with stronger tornadoes during TVS events in Hawai‘i.

The dataset seems ripe for further study. For example, further examination is needed to determine possible reasons for the locations, timing, and intensity of MEHS and TVS events. A study of synoptic patterns associated with those cases would almost certainly be useful in this attempt. It would also be useful to determine if there are favorable low-level flow directions or speeds which are commonly associated with locations stronger events, particularly in determining areas of orographic lift or favored zones of low-level convergence downwind from the islands. A closer examination of the preferred motions for MEHS events and TVS cases, particularly stronger ones, may also yield useful results.

One important subset of storms which is largely excluded by this research are events where the predominant hazard is damaging winds (i.e., QLCS). Certainly, damaging winds can occur in the absence of high reflectivity aloft and intense rotation. The limitations of Level III radar data in identifying damaging winds have already been discussed, but it may still be possible to use this dataset to identify a suitable proxy for damaging winds, such as cell motions. More study is needed to verify if this is a viable solution. An ever-growing Level II (native resolution) archive should also offer promising data.

The results in this dataset largely do not consider the differences in background conditions favoring land based events, versus water. It seems likely that there may be some differences in the conditions optimal for thunderstorms over land versus over the water. Possible differences in timing (both diurnal and seasonal) for land versus oceanic events need to be explored, particularly with respect to synoptic regime.

Finally, it seems logical to explore interannual variability within the dataset to look for possible applications for seasonal forecasting. For example, well known longer-term climatological signals (such as the ENSO phase or Madden Julian Oscillation) may show correlations with the total number and overall timing, locations, or intensity of MEHS and TVS events during a given season. Such correlations could help us to anticipate potential hazards in the longer range.

Appendix A: WSR 88-D TVS adaptable parameters

The following is a list of the WSR-88D Tornado Vortex Signature adaptation parameters in use at NWS Honolulu. Values in bold are adaptable at the radar control console, but generally are not changed without prior approval.

10 dBz: Min reflectivity

11 m s^{-1}: Vector velocity difference

100 km: Max pattern vector range

10.0 km: Max pattern vector height

2500: Max number of pattern vectors

11 m s^{-1}: Diff. velocity threshold 1

15 m s^{-1}: Diff. velocity threshold 2

20 m s^{-1}: Diff. velocity threshold 3

25 m s^{-1}: Diff. velocity threshold 4

30 m s^{-1}: Diff. velocity threshold 5

35 m s^{-1}: Diff. velocity threshold 6

3: Min # of vectors per 2D feature

0.5 km: 2D vector radial distance

1.5°: 2D vector azimuthal distance

4.0 km/km: 2D feature aspect ratio

2.5 km: Circulation radius #1

4.0 km: Circulation radius #2

80 km: Circulation radius range

600: Max number of 2D features

3: Min number of 2D feature/3D feature

1.5 km: Min 3D feature depth

25 m s^{-1}: Min 3D feature low level delta V

36 m s^{-1}: Min TVS delta velocity

35: Max number of 3D features

15: Max # of TVSs

0: Max # of elevated TVSs

0.6 km: Min TVS base height

1.0°: Min TVS elevation

3.0 km: Min Avg delta velocity height

20.0 km: Max storm association distribution

Appendix B: Indices and parameters obtained from the soundings.

Precipitable Water.

The primary parameter chosen to evaluate moisture available was precipitable water. It is defined as the total mass of water vapor in a column of unit cross sectional area:

$$PW = \int_{SFC}^{TROP} q\rho \; dz$$

where q is specific humidity and ρ is the air density. The units are typically kilograms per square meter, but the values are often expressed in millimeters of equivalent water depth. There are significant regional variations to what constitutes a "significant" PW in a forecasting sense, generally being compared to a climatological mean value for a particular area.

Convective Available Potential Energy

The amount of energy available for a lifted parcel from the level of free convection to its equilibrium level can be estimated by the Convective Available Potential Energy, or CAPE (Moncrieff and Miller 1976). It is defined as

$$CAPE = g \int_{LFC}^{EL} (\frac{T_{v_p} - T_{v_e}}{T_{v_e}}) \; dz$$

where LFC is the level of free convection, EL the equilibrium level of the parcel, T_{v_p} is the virtual temperature of the parcel, and T_{v_e} is the environmental virtual temperature (Doswell and Rasmussen 1994).

There are several different ways to define the parcel used to compute CAPE, depending on the particular situation of interest. If one assumes the parcel is to be lifted from the surface, this is termed "surface-based CAPE" (SBCAPE). If the most unstable parcel in the lowest 300 hPa is lifted, then the parameter is said to be "most-unstable CAPE" (MUCAPE) (Evans and Doswell 2001). More typically, however, CAPE is often computed to be from the lifting of a layer of given depth (typically 100 or 50 hPa). Craven et al. (2002) demonstrated that the lifting of a mixed layer of air, rather than a two-dimensional parcel at some level, yields more accurate results on average when compared to observed cloud bases at the lifting condensation level. Barnes (1995) demonstrated that although initial updrafts may take advantage of undilute near-surface air, subcloud mixing and convective processes may quickly result in mixed-layer parcels being ingested into the updraft with time. In the interests of completeness, and with an understanding that it is important to know what value is most representative for a given situation, all three forms of CAPE have been included.

Thunderstorm indices: Lifted index and K-index

The Lifted Index (LI) was developed by Galway (1956) and is defined simply as the temperature difference a lifted parcel would have from the environment when raised dry adiabatically to the LCL, then moist adiabatically to the 500 hPa level. The original index included an adjustment to account for daytime heating in morning soundings. In this study, no adjustment was made to correct for diurnal changes, and the lifted layer was computed to be from the lowest 50 hPa of the sounding (similar to Tanabe [2000]), but also includes the virtual temperature correction.

The K-Index (KI), developed by George (1960) and is defined as:

$$KI = (T_{850} - T_{500)} + Td_{850} - (T_{700} - Td_{700})$$

where T indicates temperature, Td indicates dewpoint, and the subscripts indicate the pressure level, in hPa, for each.

Both the Lifted Index and K-Index are often reasonable discriminators of thunderstorm versus non-thunderstorm environments. There are regional variations as to what constitutes significant values of each. However, generally negative values of LI, or values of KI greater than about 30, are considered to be favorable for thunderstorm development.

Storm-Relative Helicity

Davies-Jones et al. (1990) defined a parameter commonly used to analyze the potential for storm rotation, termed storm relative helicity (SRH). It is defined as:

$$SRH = -\int_0^h \boldsymbol{k} \cdot (\boldsymbol{V} - \boldsymbol{c}) \times \frac{\partial \boldsymbol{V}}{\partial z} dz$$

for an inflow layer of depth h (usually taken to be a shallow layer of 1 to 3 km in depth). **V** is the horizontal wind velocity and **c** is the storm motion vector. For this study, the storm motion vector is approximated using the Bunkers (2000) internal dynamics method. Both the 0-1 km SRH and the 0-3 km SRH were obtained, because of their utility in tornado forecasting. Rasmussen and Blanchard (1998) found that tornadic thunderstorms became more likely when 0-3 km SRH approached or exceeded 200 $m^2 s^{-2}$. A study by Thompson et al. (2007) showed that tornadoes became increasingly likely with thunderstorms when the 0-1 km SRH values exceed 100 $m^2 s^{-2}$.

While it is generally now accepted that using an effective layer of storm relative inflow as described by Thompson et al. (2007) yields a superior result, the fixed layers are sufficient to develop an initial climatological baseline.

Bulk wind difference from 0-6 km

Strong vertical shear of the horizontal wind is a known contributor to supercell development. In a strongly sheared environment, tilting of the updraft within the thunderstorm protects it from precipitation-driven downdrafts and evaporative cooling through entrainment of mid-level dry air commonly found in supercell environments. Rasmussen and Blanchard (1998) established from observations that thunderstorms were more likely to become supercellular when the boundary layer to 6 km wind difference reached or exceeded 15-20 m s^{-1}, with non-supercell thunderstorms more likely with values below 15 m s^{-1}. Supercell thunderstorms are strongly associated with severe weather. However, unlike storm-relative helicity, the Rasmussen and Blanchard study found that there was not a significant difference in the values associated with tornadic thunderstorms compared to supercells, so this parameter does not appear to be a good discriminator for tornadic versus non-tornadic potential.

Supercell Composite Parameter

This parameter, designed to highlight ideal conditions for storm development and rotation of discrete cells, was introduced by Thompson et al. (2002), and later modified (2004). The 2004 version of the parameter is defined as:

$$SCP = \left(\frac{\boldsymbol{MUCAPE}}{1000\ J\ kg^{-1}}\right) * \left(\frac{effective\ BWD}{20\ m\ s^{-1}}\right) * \left(\frac{effective\ SRH}{50\ m^2\ s^{-2}}\right)$$

where MUCAPE is as previously described, and effective bulk wind difference (BWD) and effective SRH are as described in Thompson (2007). Each term is normalized to a value considered optimal for supercell development based on past studies. The second term is set to zero when effective BWD is less than 10 m s^{-1} and set to 1 when effective BWD is greater than 20 m s^{-1}. Values of 0.5 to 3.4 or greater (median 1.7) were shown to be associated with cells that achieved marginal supercell characteristics, with surface based supercells commonly associated with SCP values of 2.2 or greater (median 5.7). For ease of calculations, the effective shear and SRH terms were approximated in this study to be the 0-6 km bulk wind difference and the 0-3 km SRH (as given in Thompson [2002]), respectively.

Severe Weather Threat (SWEAT) Index

This empirically-derived index was developed by Miller (1972) and is defined as

$$SWEAT = 12(Td_{850}) + 20(TT - 49) + 2(wind_{850}) + wind_{500} + 125(\sin(dir_{500-850}) + 0.2)$$

where Td_{850} is the dewpoint at 850 hPa, TT is the total totals index (defined as the sum of the 850 hPa temperature and dewpoint in °C minus twice the 500 hPa temperature), $wind_{850}$ and $wind_{500}$ are the wind speed at 850 hPa and 500 hPa, respectively, and $dir_{500\text{-}850}$ is the angle between the 500 hPa and 850 hPa. Miller found that with high values of SWEAT and sufficient triggering mechanism, values above about 300 were more likely to yield severe thunderstorms, with values over 400 favorable for tornadoes. This index is included here as a comparison with findings from Schroeder (1977) and Tanabe (2000).

Temperatures and geopotential heights at 500 hPa and 700 hPa

Bunkers et al. (2010) noted that even with more advanced diagnostic measures of evaluating the possibility for convection (e.g., considering CAPE and convective inhibition or CIN), there may be occasions when it is useful to utilize more simple indicators as well, particularly when modeled representations of integrated parameters may suffer due to difficulties in resolving relatively subtle features that may affect CAPE and CIN, particularly in the boundary layer. They caution, though, that much like other convective indices, these rules-of-thumb must be used carefully, in combination with climatology, and with an understanding of the meteorological processes at work. Since 500 hPa and 700 hPa heights and temperatures are frequently examined during the forecast process in Hawai‘i, it seems logical to include these in a climatology of deep convection in Hawai‘i.

Appendix C. Selected climatological sounding parameters from Līhu‘e RAOB (1973-2017).

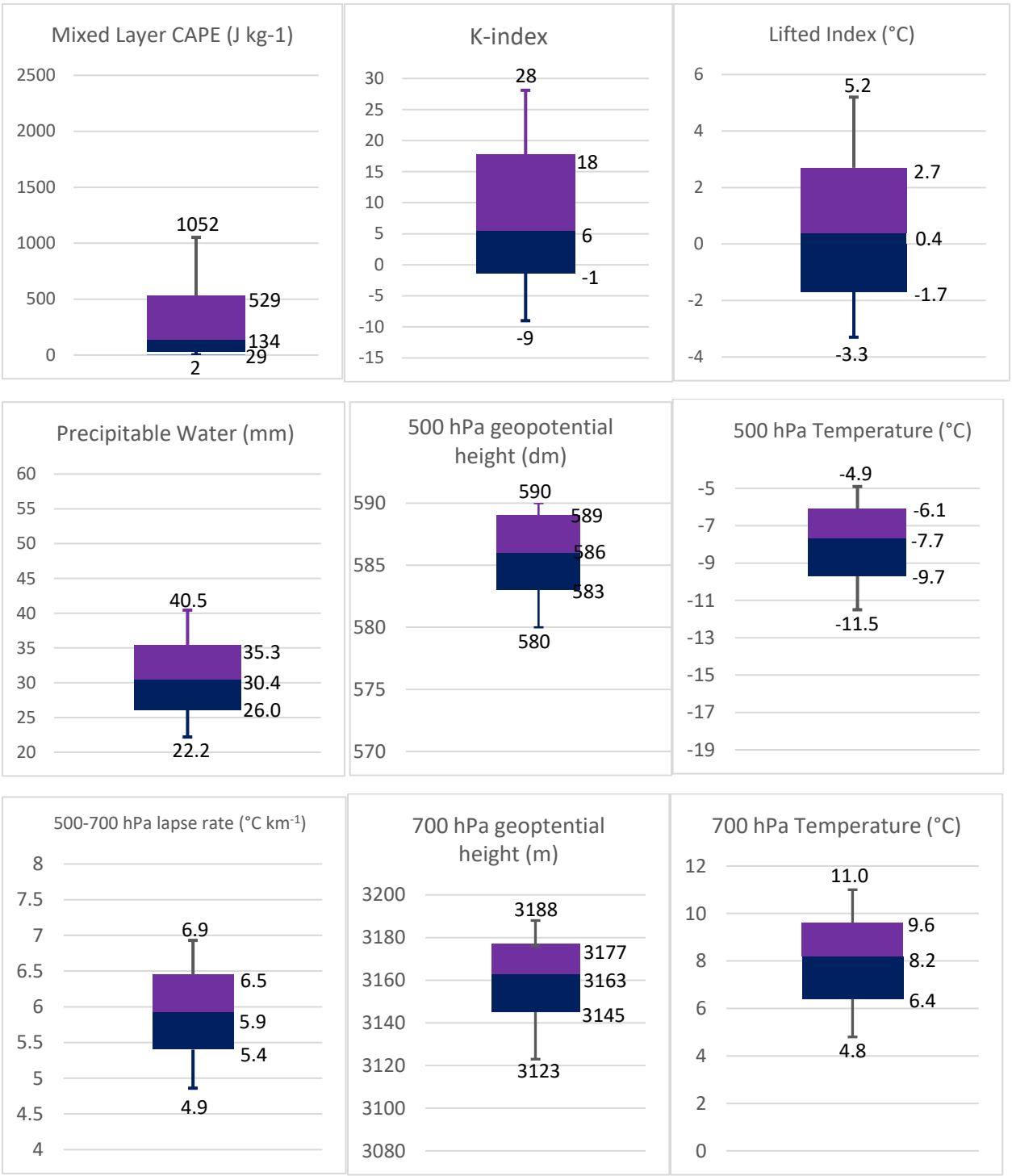

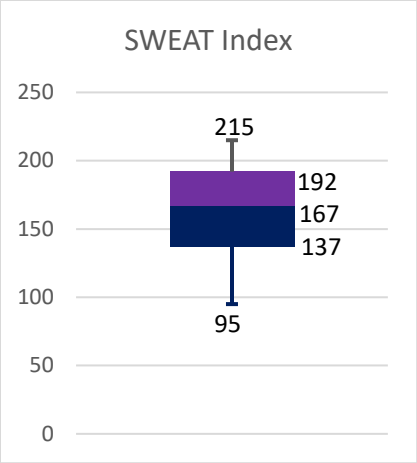
SWEAT Index
250
200
150
100
50
0
215
192
167
137
95

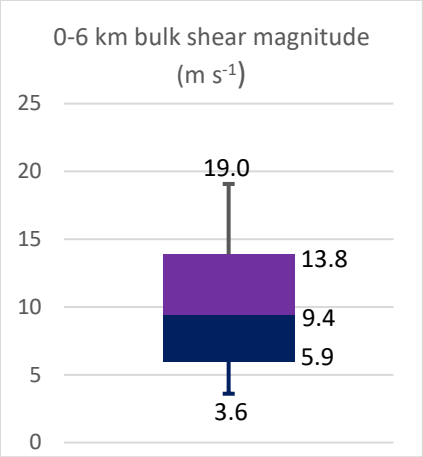
0-6 km bulk shear magnitude
(m s-1)
25
20
15
10
5
0
19.0
13.8
9.4
5.9
3.6

References

Barnes, G. M., 1995: Updraft evolution: A perspective from cloud base. *Mon. Wea. Rev.*, **123,** 2693-2715.

Barnes, G. M., 2001: Severe local storms in the tropics, *Severe Convective Storms*, *Meteor. Monogr.*, No. 50, Amer. Meteor. Soc., 359-432.

Blanchard, D. O., 1998: Assessing the vertical distribution of convective available potential energy. *Wea. Forecasting*, **13**, 870-877.

Blumenstock, D. L., and S. Price, 1967: Climates of the United States-Hawaii, Climatography of the United States No. 60-51, U.S. Dept. of Commerce, ESSA, 27 pp.

Businger, S., T. Birchard, K. Kodama, P. A. Jendrowski, and J. J. Wang, 1998: A bow echo and severe weather associated with a kona low in Hawaii. *Wea. Forecasting*, **13,** 306-321.

Bunkers, M. J., J. R. Wetenkamp Jr., J. J. Schild, and A. Fischer, 2010: Observations of the relationship between 700-mb temperatures and severe weather reports across the contiguous United States. *Wea. Forecasting,* **25,** 799-814.

Bunkers, M. J., B. A. Klimowski, J. W. Zeitler, R. L. Thompson, and M. L. Weisman, 2000: Predicting supercell motion using a new hodograph technique. *Wea. Forecasting,* **15,** 61-79.

Chen, Y.-L., and A. J. Nash, 1994: Diurnal variation of surface airflow and rainfall frequencies on the island of Hawaii. *Mon. Wea. Rev.*, **122,** 34-56.

Chen, Y.-L., and J. Feng, 1995: The influences of inversion height on precipitation and airflow over the island of Hawaii. *Mon. Wea. Rev.*, **123,** 1660-1676.

Craven, J. P., Jewell, R. E., and H. E. Brooks, 2002: Comparison between observed convective cloud-base heights and lifting condensation level for two different lifted parcels. *Wea. Forecasting*, **17,** 885-890.

Crum, T., and R. Alberty, 1993: The WSR-88D and the WSR-88D Operational Support Facility. *Bull. Amer. Meteor. Soc.* **74,** 1669-1687.

Davies-Jones, R. P., D. Burgess, and M. Foster, 1990: Test of helicity as a tornado forecast parameter. Preprints, *16th Conf on Severe Local Storms*. Kananaskis Park, AB, Canada, Amer. Meteor. Soc., 588-592.

Dostalek, J. F., and Schmit, T. J., 2001: Total precipitable water measurements from GOES sounder derived product imagery. *Wea. Forecasting,* **16,** 573-587.

Doswell, C. A. III, 1987: The distinction between large-scale and mesoscale contribution to severe convection: A case study example. *Wea. Forecasting*, **2,** 3-16.

Doswell, C. A. III, and E. N. Rasmussen, 1994: The effect of neglecting the virtual temperature correction on CAPE calculations. *Wea. Forecasting,* **9,** 625–629.

Doswell, C. A. III, and D. M. Shultz, 2006: On the use of indices and parameters in forecasting severe storms, *Electronic J. Severe Storms Meteor.,* **1**(3), 1-22.

Evans, J. S., and C. A. Doswell III, 2001: Examination of derecho environments using proximity soundings. *Wea. Forecasting,* **16,** 239-342.

Dye, J. E., W. P. Winn, J. J. Jones, and D. W. Breed, 1989: The electrification of New Mexico thunderstorms. Part I: The relationship between precipitation development and the onset of electrification. *J. Geophys. Res.*, **94,** 8643-8656.

Frisby, E. M. and H. W. Sansom, 1967: Hail incidence in the tropics. *J. Appl. Meteor*., **6,** 339-354.

Galway, J. G., 1956: The lifted index as a predictor of latent instability. *Bull. Amer. Meteor. Soc.*, **37,** 528-529.

Garrett, A. J., 1980: Orographic cloud over the eastern slopes of Mauna Loa volcano, Hawaii, related to insolation and wind. *Mon. Wea. Rev.,* **108,** 931-941.

Gibbs, J. G., 2016: A skill assessment of techniques for real-time diagnosis and short-term prediction of tornado intensity using the WSR-88D. *J. Operational Meteor.,* **4**(13), 170-181.

Johns, R. H., and Doswell, C. A., III, 1992: Severe local storms forecasting. *Wea. Forecasting,* **7,** 588-612.

Kodama, K., and G. M. Barnes, 1997: Heavy rain events over the south-facing slopes of Hawaii: Attendant conditions. *Wea. Forecasting,* **12,** 347-367.

Kodama, K. R., and Businger, S., 1998: Weather and forecasting challenges in the Pacific Region of the National Weather Service. *Wea. Forecasting,* **13,** 523-546.

Kingfield, D. M., and J. G. LaDue, 2015: The relationship between automated low-level velocity calculations from the WSR-88D and maximum tornado intensity determined from damage surveys. *Wea. Forecasting,* **30,** 1125-1139.

Lavoie, R. L., 1967: Air motions over the windward coast of the Island of Hawaii. *Tellus,* **19,** 354-358.

Leopold, L. B., 1949: The interaction of trade wind and sea breeze, Hawaii. *J. Meteor.,* **6,** 312-320.

Lucas, C., E. J. Zipser, and M. A. LeMone, 1994a: Vertical velocity in oceanic convection off tropical Australia. *J. Atmos. Sci.,* **51,** 3182-3193.

Lucas, C., E. J. Zipser, and M. A. LeMone, 1994b: Convective available potential energy in the environment of oceanic and continental clouds: Corrections and comments. *J. Atmos. Sci.,* **51,** 3829-3830.

Lyman, R. E., Schroeder, T. A., and G. M. Barnes, 2005: The heavy rain event of 29 October 2000 in Hana, Maui. *Wea. Forecasting,* **20,** 397-414.

McCaul, E. W., and M. L. Weisman, 1996: Simulations of shallow supercell storms in landfalling hurricane environments. *Mon. Wea. Rev.,* **124,** 408-429.

McCaul, E. W., and M. L. Weisman, 2001: The sensitivity of simulated supercell structure and intensity to variations in the shapes of environmental and shear profiles. *Mon. Wea. Rev.*, **129,** 664-687.

Miller, R. C. 1972: Notes on analysis and severe storm forecasting procedures of the Air Force Global Weather Central. AWS Tech. Rep. 200 (revised), 190 pp.

Mitchell, E. D., S. V. Vasiloff, G. J. Stumpf, A. Witt, M. D. Eilts, J. T. Johnson, and K. W. Thomas, 1998: The National Severe Storms Laboratory tornado detection algorithm. *Wea. Forecasting*, **13,** 352-366.

Moncrieff, M. W., and M. J. Miller, 1976: The dynamics and simulation of tropical cumulonimbus and squall lines. *Quart. J. Roy. Meteor. Soc.,* **102,** 373-394.

Monteverdi, J. M., and J. Quadros, 1994: Convective and rotational parameters associated with three tornado episodes in northern and central California. *Wea. Forecasting*, **9,** 285-300.

NCEI, 2005: *Storm Data*, Vol. 47, No. 1, 226 pp.

NCEI, 2009a: *Storm Data*, Vol. 51, No. 2, 276 pp.

NCEI, 2009b: *Storm Data*, Vol. 51, No. 12, 278 pp.

NCEI, 2010: *Storm Data*, Vol 52, No. 12, 242 pp.

NCEI, 2011: *Storm Data.* Vol. 53, No. 3, 386 pp.

NOAA, 2005: Jan 8-9, 2005 Severe storms on Kauai and Oahu [Available online at http:// http://www.prh.noaa.gov/hnl/pages/events/jan9storms/]

OFCM, 2005: Present weather. Surface weather observations and reports, Federal Meteorological Handbook 1, Doc. FCM-H1-2005, 8-7. [Available online at http://www.ofcm.gov/publications/fmh/FMH1/FMH1.pdf]

Pessi, A., S. Businger, K.L. Cumins, N. W. S. Demetriades, M. Murphy, and B. Pifer, 2009: Development of a long range lightning detection network for the Pacific: Construction, calibration, and performance. *J. Atmos. Oceanic Technol.,* **26,** 145-166.

Price, S., and R. I. Sasaki, 1963: Some tornadoes, waterspouts, and other funnel clouds of Hawaii. *Mon. Wea. Rev.,* **91,** 175-190.

Rasmussen, E. N., and D. O. Blanchard, 1998: A baseline climatology of sounding-derived supercell and tornado forecast parameters. *Wea. Forecasting,* **13,** 1148–1164.

Rasmussen, R. M., and A. J. Heymsfield, 1987: Melting and shedding of graupel and hail. Part II: Sensitivity study. *J. Atmos. Sci.,* **44,** 2764-2782.

Schroeder, T. A., 1977: Hawaiian Waterspouts and tornadoes. *Mon Wea. Rev.,* **105,** 1163-1170.

Schroeder, T. A., 1993: Climate Controls. *Prevailing Trade Winds,* M. Sanderson, Ed., University of Hawaii Press, 13-36.

Schroeder, T. A., B. J. Kilonsky, and B. N. Meisner, 1977: Diurnal variation in rainfall and cloudiness. UH-MET 77-03, Dept. of Meteorology, University of Hawaii, 67 pp.

Sherburn, K. D., and M. D. Parker, 2014: Climatology and ingredients of significant severe convection in high shear, low CAPE environments. *Wea. Forecasting,* **29,** 854-877.

Smith, B. T., R. L. Thompson, H. E. Brooks, A. R. Dean, and K. L. Elmore, 2012: Diagnosis of Conditional Maximum Tornado Damage Probabilities. *Proc. 26th Conf. on Severe Local Storms*, Nashville, TN, Amer. Meteor. Soc., P2.20.

Takahashi, T., 1987: Hawaiian hailstones—30 January 1985. *Bull. Amer. Meteor. Soc.,* **68,** 1530-1534.

Tanabe, R., 2000: Waterspouts, funnels, and tornadoes in the vicinity of the Hawaiian Islands. M.S. thesis, Dept. of Meteorology, University of Hawaii, 76 pp.

Thompson, R. L., C. M. Mead, and R. Edwards, 2007: Effective storm-relative helicity and bulk shear in supercell thunderstorm environments. *Wea. Forecasting,* **22,** 102-115.

Thompson, R. L., R. Edwards, and J. A. Hart, 2002: Evaluation and interpretation of the supercell composite and significant tornado parameters at the Storm Prediction Center. Preprints, *21st Conf. on Severe Local Storms,* San Antonio, TX, Amer. Meteor. Soc., J11-J14.

Thompson, R. L., R. Edwards, and C. M. Mead, 2004: An update to the supercell composite and significant tornado parameters. Preprints, *22nd Conf on Severe Local Storms,* Hyannis, MA, Amer. Meteor. Soc., P8.1.

Thompson, K. B., M. G. Bateman, and L. D. Carey, 2014: A comparison of two ground-based lightning detection networks against the satellite-based Lightning Imaging Sensor (LIS). *J. Atmos. Oceanic Technol.,* **31,** 2191-2205.

Toracinta, E. R., K. I. Mohr, E. J. Zipser, and R. E. Orville, 1996: A comparison of WSR-88D reflectivities, SSM/I brightness temperatures, and lightning for mesoscale convective systems in Texas. Part I: Radar reflectivity and lightining. *J. Appl. Meteor.*, **35,** 902-918.

Wakimoto, R. M., and J. W. Wilson, 1989: Non-supercell tornadoes. *Mon. Wea. Rev.,* **117,** 1113-1140.

Weisman, M. L., and J. B. Klemp, 1984: The structure and classification of numerically simulated convective storms in directionally varying wind shears. *Mon. Wea. Rev.,* **112,** 2479-2498.

Witt, A., M. D. Eilts, G. J. Stumpf, J. T. Johnson, E. D. Mitchell, and K. W. Thomas, 1998: An enhanced hail detection algorithm for the WSR-88D. *Wea. Forecasting,* **13,** 268-303.

Wood, V. T., and R. A. Brown, 1997: Effects of radar sampling on single-Doppler velocity signatures of mesocyclones and tornadoes. *Wea. Forecasting,* **12,** 928-938.

Yang, Y. H., and P. King, 2010: Investigating the potential of using radar echo reflectivity to nowcast cloud-to ground lightning initiation over southern Ontario. *Wea. Forecasting,* **25,** 1235-1248.

Zipser, E. J., 1994: Deep cumulonimbus cloud systems in the tropics with and without lightning. *Mon Wea Rev,* **122,** 1837-1851.

Zipser, E. J., and K. Lutz, 1994: The vertical profile and radar reflectivity of convective cells: A strong indicator of storm intensity and lightning probability? *Mon. Wea. Rev.,* **122,** 1751-1759.

Zrnic, D. S., and A. Ryzhkov, 1999: Polarimetry for weather surveillance radars. *Bull. Amer. Meteor. Soc.,* **80,** 389-406.

Zrnic, D. S., and A. Ryzhkov, 2004: Polarimetric properties of chaff. *J. Atmos. Oceanic Technol.,* **21,** 1017-1024.